The Measurement of Atmospheric Species with Absorptions Close to the Actinic Flux Cut-off by Active & MAX-DOAS: Chlorine Monoxide (ClO) & Sulphur Dioxide (SO_2)

Csilla Csukat

A thesis submitted to the Faculty of Graduate Studies in partial fulfillment of the requirements for the degree of

Master of Science

Graduate Program in Chemistry

York University

Toronto, Ontario

March 2019

ABSTRACT

The gas-phase chlorine monoxide (ClO) radical has been studied extensively for its role in catalytic stratospheric ozone depletion following the discovery of the Antarctic ozone hole in 1985. Reactive chlorine chemistry is known to occur in the troposphere as well, originating primarily from sea salt aerosols in the marine boundary layer, but direct spectroscopic observations have been limited. In this research, we endeavour to identify and quantify ClO in a mid-latitude urban atmosphere removed from a large source of salt water, using techniques of differential optical absorption spectroscopy (DOAS). In particular, we seek to determine whether this trace gas is present in any appreciable amount in ambient air during the wintertime owing to the widespread application of road salt. The study was performed at The Centre for Atmospheric Chemistry at York University in Toronto, Ontario, Canada (43.77° N, 79.50° W) using Active long-path DOAS and MAX-DOAS. We further take interest in SO_2; a secondary absorbing species in the wavelength range bordering the cut-off of solar actinic flux. In a complementary study at the Welland Canal in Ontario, we demonstrate that it may be possible to measure trace amounts of SO_2 in ship plumes using a stationary MAX-DOAS instrument.

Feasibility modeling was first performed using a pair of analogous zero-dimensional models; AcuChem and AtChem Online, running a subset of the Master Chemical Mechanism (MCM) with the addition of key tropospheric chlorine-containing species and reactions. Both models predicted a maximum ClO mixing ratio on the order of a few ppt, within a few hours after sunrise. Under conditions of low NO_2 and given a 3 ppb input of nitryl chloride ($ClNO_2$), our model predicts a maximum 7 ppt of ClO. These modeling results are unique to our study and may serve to guide future experimental studies. Experimental identification and quantification of the ClO radical was not concrete within our dataset, comprised of intermittent diurnal mixing ratio profiles on dates with and without snowfall over the course of a year. Although research of this kind is not widely available for comparative value, results were unexpectedly high in all seasons, reaching a maximum of over 150 ppt in opposition to much lower levels of ClO found in previous instances in the literature and as dictated by results of the aforementioned preliminary modeling. We explore the possibility that these measurements comprise a combination of both tropospheric and stratospheric ClO but conclude that a stratospheric origin is unlikely. This leads us to believe there may have existed complications in data acquisition or analysis, giving rise to an apparent experimental artifact in our results. It is also very likely that with our current instrumentation, detection limits are too high for measuring ClO at expected levels. Further improvements and testing is required to confirm our results, and a series of recommendations for the current active-DOAS system to achieve better detection limits is included.

TABLE OF CONTENTS

LIST OF TABLES

Chapter 1: Introduction

Chapter 2: Methods

Chapter 3: Results & Discussion

LIST OF FIGURES

Chapter 1: Introduction

Chapter 2: Methods

Chapter 3: Results & Discussion

CHAPTER 1: INTRODUCTION

1.1: Composition & Structure of the Atmosphere

Earth's atmosphere has evolved over billions of years, shaped by natural processes and in recent times, by human activity. **Table 1.1** displays the present-day chemical composition of air, with nitrogen (78%) and oxygen (21%) being the most abundant constituents, while the remainder are trace gases. A trace gas is one that makes up less than 1% of the Earth's atmosphere, yet can play a significant role in air pollution, climate change and the critical environmental issues we face. These gases are often in the form of stable molecules or radical species, rendering them highly reactive with short lifetimes, and they can be challenging to measure experimentally. However, these free radicals are the driving force behind much of the chemistry occurring in the atmosphere, affecting both the quality of the air that surrounds us locally on a daily basis and the long-term sustainability of the planet on a global scale.

Table 1.1: The major and trace gaseous constituents of the atmosphere. Adapted from "Atmospheric Chemistry," by A.M. Holloway and R.P. Wayne, 2010, RSC Publishing, Cambridge.

Atmospheric constituent	*Source*	*Mixing ratio (ppm)*	*Percentage*
Nitrogen N_2	Prebiological Microbiological	780 840	78.08
Oxygen O_2	Photosynthesis	209 460	20.95
Argon Ar	Mainly radiogenic	9340	0.93
Carbon dioxide CO_2	Prebiological	350	0.035
Water H_2O	Prebiological	0–40 000[a]	
Neon Ne	Prebiological	18	
Helium He	Mainly radiogenic	5.2	
Methane CH_4	Microbiological	1.7	
Hydrogen H_2	Some volcanic (birth)	0.53	
Nitrous oxide N_2O	Microbiological	0.3	
Carbon monoxide CO	Microbiological Oxidation product	0.04–0.2	
Ammonia NH_3	Microbiological	<0.01	
Hydrogen sulfide H_2S	Microbiological	10^{-4}	
Sulfur dioxide SO_2	Volcanic	10^{-4}	
Ozone O_3	Photochemical production from O_2	0–10[b]	

[a]The amount of water varies considerably according to climatic conditions.
[b]The value for ozone varies principally with altitude

The structure of the atmosphere is divided into four key regions; the troposphere, stratosphere, mesosphere and thermosphere, as shown in **Figure 1.1** (Finlayson-Pitts and Pitts, 2000). These divisions are based on temperature variation as a function of altitude, with a shift to the opposite temperature profile at the tropopause, stratopause and mesopause transition zones, such that temperature is decreasing with altitude in the troposphere, and increasing with altitude in the stratosphere. In studying diurnal dynamics, we consider layers within the troposphere, as can be seen in **Figure 1.2.** These regularly occurring stratifications are a meteorological phenomenon brought on by temperature inversions, characterized by a disruption in the atmospheric lapse rate. Reversal to a negative lapse rate is caused by rapid cooling of the Earth's surface and the adjacent layer of air following sunset, often

becoming cooler than the layers above, particularly on calm nights. The inversion which forms creates what we define to be a nocturnal boundary layer (NBL), typically extending up to 100 m and trapping emitted pollutants near the surface. A residual layer (RL) forms above, containing species that were present in a daytime boundary layer, ranging anywhere from around 100 - 3000 m (Finlayson-Pitts and Pitts, 2000). The inversion breaks up following sunrise, when re-heating of surface air restores the balance in which in less dense air rises and atmospheric mixing occurs (Finlayson-Pitts and Pitts, 2000). We therefore note that a study in atmospheric chemistry is often a study involving one or more trace gases, in a given region(s) of the atmosphere, at a given time(s) of day.

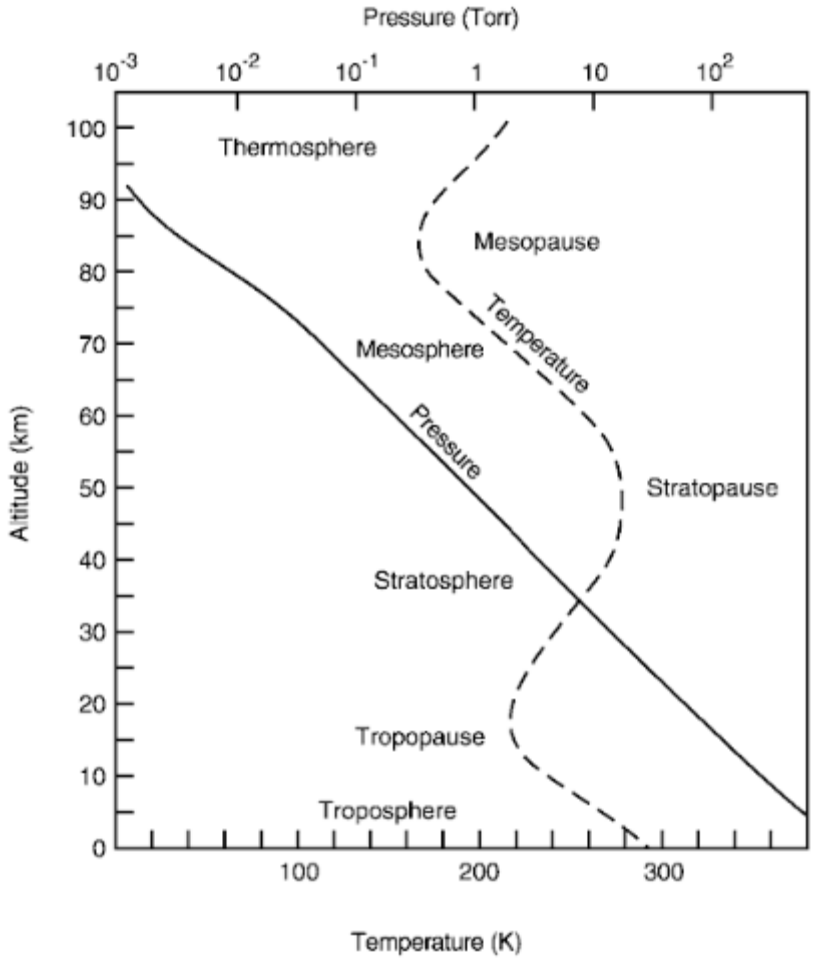

Figure 1.1: Typical variation of temperature and pressure with altitude at mid-latitudes. Adapted from "Chemistry of the Upper and Lower Atmosphere: Theory, Experiments, and Applications," by B.J. Finlayson-Pitts and J.N. Pitts Jr., 2000, Academic Press, San Diego, CA.

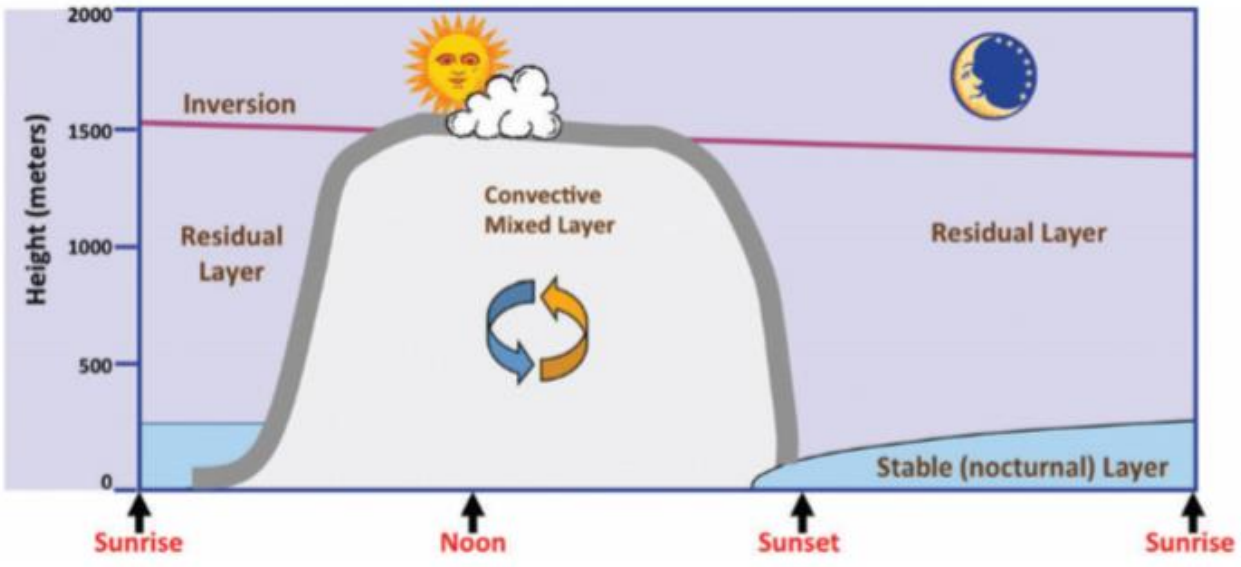

Figure 1.2: Typical variation of the planetary boundary layer (PBL) structure with time of day. Adapted from "Nighttime radical observations and chemistry," by S.S. Brown and J. Stutz, 2012, Chem. Soc. Rev., 41, p. 6405–6447.

1.2: Chlorine Chemistry in the Stratosphere & Troposphere

Stratosphere

Since the discovery of the Antarctic ozone hole in the mid-1980s, chlorine chemistry has been at the forefront of atmospheric research, historically regarded as primarily a stratospheric phenomenon (Farman et al., 1985). Loss of ozone was first linked to increasing concentrations of chlorofluorocarbons (CFCs) about a decade prior, in the mid-1970s (Molina and Rowland, 1974). It was revealed that inert manmade CFCs, the most common of which were refrigerants, were transported up into the stratosphere, where they then underwent photolysis to release chlorine atom radicals (Jacob, 1999). These radicals form chlorine monoxide (ClO); a trace atmospheric gas most commonly associated with the depletion of ozone in the stratosphere, and the primary focus of our study. The chemistry of the chlorine-catalyzed ozone destruction cycle involving the ClO radical is as follows (Jacob, 1999):

Cycle 1:

$$Cl\cdot + O_3 \longrightarrow ClO\cdot + O_2$$

$$ClO\cdot + O \longrightarrow Cl\cdot + O_2$$

Net: $O_3 + O\cdot \longrightarrow 2O_2$

This catalytic cycle is eventually terminated through conversion into HCl and $ClNO_3$., the stable terminal reservoirs of atmospheric chlorine (Jacob, 1999). Under the exceptionally cold temperatures of the Antarctic, ClO will self associate to form a dimer and this enhances ozone destruction through the

following series of reactions involving Cl, ClO and other chlorine oxide species, ClO_x (Holloway and Wayne, 2010):

Cycle 2:

$$ClO\cdot + ClO\cdot + M \rightarrow (ClO)_2 + M$$

$$(ClO)_2 + hv \rightarrow Cl\cdot + ClOO\cdot$$

$$ClOO\cdot + M \rightarrow Cl\cdot + O_2 + M$$

$$2(Cl\cdot + O_3 \rightarrow ClO\cdot + O_2)$$

Net: $2O_3 \rightarrow 3O_2$

Cycle 3:

$$ClO\cdot + BrO\cdot \rightarrow Cl\cdot + Br\cdot + O_2$$

or $ClO\cdot + BrO\cdot \rightarrow BrCl + O_2$ & $BrCl + hv \rightarrow Cl\cdot + Br\cdot$

$$Cl\cdot + O_3 \rightarrow ClO\cdot + O_2$$

$$Br\cdot + O_3 \rightarrow BrO\cdot + O_2$$

Net: $2O_3 \rightarrow 3O_2$

As this ClO_x-catalyzed ozone loss was becoming a clear threat to the integrity of the ozone layer, implementation of internationally-followed agreements, including the well-known Montreal Protocol in 1987, led to a complete ban on CFCs (Jacob, 1999). Evidence of the healing of the ozone hole in the upper stratosphere has recently been published (Solomon at al., 2016; Strahan and Douglass, 2018).

Troposphere

Over the past decade or so, the role of chlorine in tropospheric chemistry has become increasingly evident. Here, the primary driver of this chemistry, the chlorine atom radical, may derive from the photolysis of chlorocarbons, the oxidation of HCl, or most commonly, from the heterogeneous and multiphase formation reactions of photolabile chlorinated compounds such as nitryl chloride, $ClNO_2$, among others (Faxon and Allen, 2013). The significance of $ClNO_2$ was first discovered when NaCl aerosols were irradiated in the presence of NO_x, generating a large flux of chlorine radicals that could not be accounted for by homogeneous gas-phase reactions alone (Finlayson-Pitts et al., 1989; Behnke and Zetzsch, 1990). It is now known that $ClNO_2$ accumulates overnight, produced by the heterogeneous uptake of dinitrogen pentoxide, N_2O_5, on chloride-containing aerosol particles (Bertram and Thornton, 2009). $ClNO_2$, along with Cl_2, undergo photolysis the next morning to release these highly reactive chlorine radicals (Osthoff et al., 2008):

$$N_2O_5 + Cl^-_{aerosols} \rightarrow ClNO_2 + NO_3\cdot$$

$$ClNO_2 + hv\ (\lambda < 839\ nm) \rightarrow Cl\cdot + NO_2$$

$$Cl_2 + hv\ (\lambda < 493\ nm) \rightarrow Cl\cdot + Cl\cdot$$

The chlorine atom will oxidize VOC's, through hydrogen abstraction, in turn leading to enhanced surface ozone production (Finlayson-Pitts and Pitts, 2000). The rates of these reactions are often orders of magnitude faster than the corresponding O_3 and OH reactions for several of the most abundant VOC's, including methane, isoprene and some monoterpenes (Faxon and Allen, 2013). Alternatively, as in the stratosphere, Cl may destroy O_3, forming the chlorine monoxide radical, ClO, our species of interest

(Jacob, 1999). Therefore, the amount of ClO produced and the extent of ozone production or destruction will depend on the VOC to O_3 ratios:

$$Cl\cdot + RH \longrightarrow HCl + R\cdot$$

$$Cl\cdot + O_3 \longrightarrow ClO\cdot + O_2$$

The ClO radical may be short lived as it undergoes subsequent reaction and is lost through a number of channels. This is largely attributable to its own photolysis or to its three-body reaction with NO_2, thought to be its primary loss process (Jacob, 1999). Therefore, although NO_x is required for the formation of the $ClNO_2$ precursor at night, it may hinder accommodation of ClO the next morning. As mentioned, the highly reactive chlorine free radical may bypass ClO formation altogether, instead forming HCl in a competing reaction with methane or other non-methane hydrocarbons (Finlayson-Pitts and Pitts, 2000). For these reasons, it is predicted that the terminal reservoirs of the atmospheric chlorine are more likely to be the stable non-radical species HCl and $ClONO_2$.

$$ClO\cdot + h\nu\ (\lambda < 445\ nm) \longrightarrow Cl\cdot + O\cdot$$

$$ClO\cdot + NO_2 + M \longrightarrow ClONO_2 + M$$

It has previously been shown that in contrast to N_2O_5, $ClNO_2$ does not exhibit a strong vertical gradient through the lower troposphere; however, O_3 can be higher in the residual layer (Young et al., 2012). As such, we may expect more ClO in this layer, which is frequently ~100+ m above ground (Brown et al., 2007). However, detection of ClO closer to the surface is possible, with the merging of the residual and nocturnal boundary layer into a single well-mixed boundary layer sometime after sunrise (Finlayson-Pitts and Pitts, 2000). Since N_2O_5 is formed strictly at night from the reaction of NO_2 and NO_3, and $ClNO_2$ accumulates and begins to photolyze after sunrise, measurements of ClO are to be taken in the early morning hours, for optimum likelihood of detection. In this study, we wish to qualitatively locate, as well as quantify the ClO radical, employing the techniques of active long-path differential optical spectroscopy (DOAS) and MAX-DOAS (Hönninger et al., 2004); to be discussed in detail in subsequent sections.

1.3: ClO in the Literature & Study Motivation

To date, a limited number of research studies have been published that report direct measurements of tropospheric ClO. Those available were conducted in arctic regions (Tuckermann et al., 1997; Pöhler et al., 2010), where the role of ClO in the stratosphere is well documented, or in coastal regions by the ocean or a large salt-water lake (Lee et al., 2008; Stutz et al., 2002), where we find pronounced chlorine in the atmosphere. This is because the largest source of inorganic chloride, required to form $ClNO_2$, derives from sea spray (Osthoff et al., 2008). As such, studies have been confined to marine regions in reach of NOx pollutant plumes, with few inland investigations conducted (Thornton et al., 2010; Mielke et al., 2011), where the source of chlorine may be from long range transport of the sea salt aerosol, or from salt beds or various direct chlorine emissions (Faxon and Allen, 2013). Furthermore, only one successful attempt at measuring ClO using MAX-DOAS has been made

(Lee et al., 2008). Therefore, the significance of the project lies in that this will be the first attempt of its kind in measuring tropospheric ClO in a non-coastal urban area like Toronto and only the second yet which attempts to use MAX-DOAS. In our study, we intend to explore wintertime road salt as a possible source of chloride in an area not in close proximity to an ocean or salt lake, salt flat, or other large natural chlorine reservoir.

In essence, the detection of ClO can function as a proxy for the presence of chlorine radical chemistry in an urban environment, in the residual layer prospectively, but perhaps in the nocturnal boundary layer as well. Chlorine radicals will impact the oxidizing power of the troposphere, particularly at a time when other primary oxidants, i.e. OH and O_3 are scarce (Osthoff et al., 2008). In Great Lake, Utah, 15 pptv of ClO was observed, corresponding to a Cl radical concentration of 10^5 molecules cm^{-3} (Stutz et al., 2002), approaching levels within an order of magnitude of the average daytime OH concentration (Finlayson-Pitts and Pitts, 2000). The general consensus we derive from the literature is that ClO is likely to be on the order of a few ppt; a review of select $ClNO_2$ precursor studies in North America is provided in **Table 1.2** and any available ClO measurements made to date has been compiled in **Table 1.3**.

Table 1.2: A selection of major studies reporting direct measurements of $ClNO_2$ mixing ratios. Adapted in part from "Chlorine chemistry in urban atmospheres: a review," by C.B. Faxon and D.T. Allen, 2013, Environ. Chem., 10, p. 221–233.

Author, Year	Location	Maximum [$ClNO_2$] (ppt)
Osthoff et al., 2008	Texas Gulf Coast	1200
Thornton et al., 2010	Boulder, Colorado	450
Mielke et al., 2011	Calgary, Alberta	250
Riedel et al., 2012	Los Angeles, California	2100
Young et al., 2012	Los Angeles, California	3000 (1200 avg)
Edwards et al., 2013	Utah (remote, inland)	2000

Table 1.3: Summary of major studies reporting direct measurements of ClO mixing ratios. The following studies provide indirect calculated or otherwise estimated concentrations: Platt et al., 1995: typical global background [ClO] est. = 10^6–10^8 molec cm^{-3}; Chang et al., 2003: calculated avg. daytime [ClO] in coastal marine boundary layer = 10^7 molec cm^{-3}; Pöhler et al., 2010: est. upper limit of daytime ClO = 7.6 pmol/mol.

Author, Year	Location	Method	[ClO] (ppt)	Fitting Range (nm)	Detection Limit (ppt)
Tuckermann et al., 1997	Ny-Alesund, Spitsbergen, Norway	Active LP-DOAS	3.3 ; 21 (averages)	275–305	8.5 to 19
Stutz et al., 2002	Great Salt Lake, Utah	Active LP-DOAS	5 to 15 ± 2 (range)	285–300	3 to 4
Lee et al., 2008	Anmyeen Island (off the west coast of Korea)	MAX-DOAS	8.4 ± 4.3 (average)	302.5–316	

The motivation behind the project is tied not only to the matter that tropospheric ClO is a relatively unexplored topic, but to the importance of airborne chlorine, including ClO and related species, in the atmosphere. The role of chlorine in the initiation of oxidative cycles and its contribution to enhanced ozone production is of great interest, particularly in urban areas where surface ozone is a monitored air pollutant with potential health hazards to the public. The detection of ClO may serve as a first step in determining whether chlorine chemistry is to be incorporated into regional air quality models. Our approach consists of theoretical feasibility modeling followed by direct experimental measurements using the DOAS technique, ideal for highly reactive trace gases and radical species such as ClO. We also utilize DOAS to measure SO_2, as ClO and SO_2 each have absorption features in the low wavelength region of actinic flux at surface level.

1.4: Theory: Differential Optical Absorption Spectroscopy (DOAS)

DOAS, the abbreviation of Differential Optical Absorption Spectroscopy, is a well-established and non-invasive analytical spectroscopic measurement technique based on the absorption of light by atmospheric gases in the UV and visible range of the electromagnetic spectrum. DOAS allows for both identification and quantification of a target trace gas and the various types of DOAS are categorized according to light source and optical configuration. The underlying foundation of the DOAS technique involves the separation of interfering broad (background) and other narrow (fingerprint) absorption features to isolate the spectrum of the target molecule (Platt and Stutz, 2008).

Mathematically, as an absorption-based spectroscopic technique, the underlying quantitative principles of DOAS are founded upon the Beer-Lambert Law (Platt and Stutz, 2008):

$$I(\lambda) = I_0(\lambda) \cdot e^{-\sigma(\lambda) \cdot L \cdot c}$$

In this equation, $I_0(\lambda)$ is the initial light intensity and $I(\lambda)$ is the intensity of the transmitted light, at a given wavelength λ, after passing through a path length L (cm) containing an analyte of concentration c (molecules cm^{-3}) with a wavelength-dependant absorption cross-section $\sigma(\lambda)$.

The optical density, D, of a layer of a particular atmospheric absorber is defined as:

$$D = \ln\left(\frac{I_o(\lambda)}{I(\lambda)}\right) = \sigma(\lambda) \cdot L \cdot c$$

The average concentration of the absorber in the air sample can be determined by rearranging the above equation to solve for variable c:

$$c = \frac{\ln\left(\frac{I_0(\lambda)}{I(\lambda)}\right)}{\sigma(\lambda) \cdot L} = \frac{D}{\sigma(\lambda) \cdot L}$$

In the real atmosphere, we must account for light loss due to Rayleigh and Mie scattering, as photons interact with air molecules and atmospheric aerosol particles, respectively. In the expanded equation, $\varepsilon_R(\lambda)$ is the Rayleigh extinction coefficient ($\varepsilon_R(\lambda) \approx \sigma_{R0} \cdot \lambda^{-4} \cdot c_{air}$) and $\varepsilon_M(\lambda)$ is the Mie extinction

coefficient ($\varepsilon_M(\lambda) = \sigma_{M0} \cdot \lambda^{-n} \cdot N_A$). A is an attenuation factor stemming from the broadband wavelength-dependant effects of instrumental transmissivity (mirrors and retroreflector) and turbulence:

$$I(\lambda) = I_0(\lambda) \cdot e^{L\left(-\sigma(\lambda) \cdot c + \varepsilon_R(\lambda) + \varepsilon_M(\lambda)\right)} \cdot A(\lambda)$$

In most instances, there is a reduction in light intensity due to more than one absorber, and so we expand the equation to account for all possible absorbing trace gases in the parcel of air:

$$I(\lambda) = I_0(\lambda) \cdot e^{-L\left(\sum \sigma_i(\lambda) \cdot c_i + \varepsilon_R(\lambda) + \varepsilon_M(\lambda)\right)} \cdot A(\lambda)$$

To simplify the task of determining variable c, DOAS measures a differential absorption, defined as the component of the total absorption which varies rapidly as a function of wavelength. While the extinction processes described above exhibit broad and smooth spectral characteristics, certain trace gases also reveal unique narrow absorption structures (< 10 nm) once isolated from the broad components that mask these features, as exemplified in **Figure 1.3**.

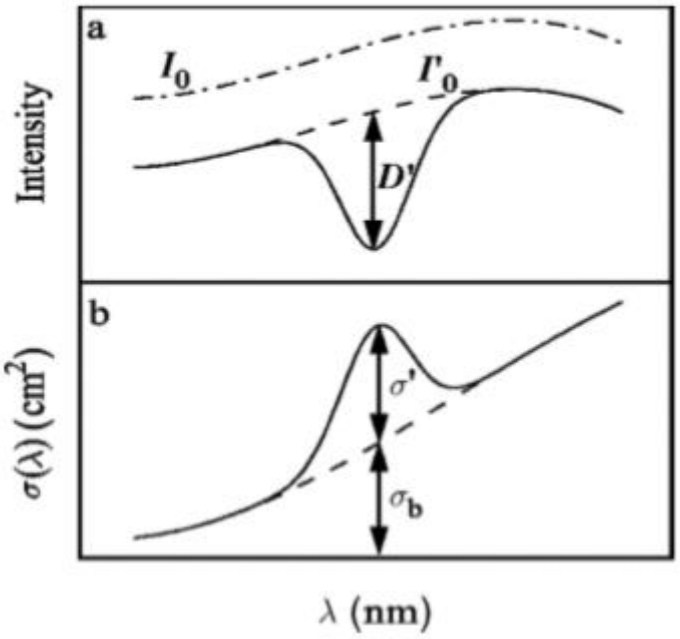

Figure 1.3: Illustrating the separation of I_0 and σ, through a filtering procedure, into narrow (D' and σ') and broadband (I'_0 and σ_b) components. Adapted from "Differential Optical Absorption Spectroscopy: Principles and Applications," by U. Platt and J. Stutz, 2008, Springer-Verlag Berlin Heidelberg.

The absorption cross sections of all species are then separated into a broadband component that varies slowly with wavelength and a narrowband component that varies rapidly with wavelength, as follows:

$$\sigma_i(\lambda) = \sigma_{i,0}(\lambda) + \sigma'_i(\lambda)$$

Incorporating the two separate components, we arrive at the final expression for transmitted light intensity:

$$I(\lambda) = I_0(\lambda) \cdot e^{-L(\sum \sigma_i'(\lambda) \cdot c_i)} \cdot e^{-L\left(\sum \sigma_{i,0}(\lambda) \cdot c_i + \varepsilon_R(\lambda) + \varepsilon_M(\lambda)\right)} \cdot A(\lambda)$$

A differential optical density, D', is then defined as:

$$D' = \ln\left(\frac{I_0'(\lambda)}{I(\lambda)}\right) = L \cdot \sum \sigma_i'(\lambda) \cdot c_i$$

Likewise, the concentration of absorber i, c_i, is solved for using the following equation and is calculated by performing a least squares fit of the structured differential absorption to an absorption cross section in the literature, a procedure described in-depth in the Experimental section:

$$c_i = \frac{D'}{\sigma_i'(\lambda) \cdot L}$$

CHAPTER 2: METHODS

2.1: Modeling: Modeling Chlorine Chemistry

2.1.1: AcuChem

Prior to beginning experimental work, feasibility modeling was performed to estimate the viability of ClO detection based on predicted approximate concentrations of its precursors and related kinetic information using a pair of simple zero-dimensional box models. This modeling was first accomplished using the chemical kinetics simulator AcuChem, ideal for large and complex sets of mechanisms (Braun et al., 1988). An input was assembled, encompassing a list of the major gas-phase bimolecular and termolecular chemical reactions and photodissociations in which ClO is formed or destroyed (Sander et al., 2006). To simplify the model, we honed in on only the following key chlorine-containing species: $ClNO_2$, Cl_2, Cl, HCl, $ClONO_2$, HOCl, and ClO. Also included were other high background level non-chlorinated species featured as reactants or products, as well as any additional reactions required to accurately model the chemistry of the troposphere (Finlayson-Pitts and Pitts, 2000). The complete model input in plain text format has been made available in **Appendix A1**. The temperature and pressure dependent rate constants of the reactions were calculated using laboratory and theoretical values and equations from the NASA Panel for Data Evaluation - Evaluation No. 15, JPL Publication 06-2 (Sander et al., 2006), at a fixed [M], where [M] is any atmospheric constituent at STP (273 K / 0 °C / 32 °F, 1 atm). Molecular photolysis frequencies were retrieved using the NCAR Tropospheric Ultraviolet and Visible (TUV) Radiation Model on a select date, March 21 2016, assuming an overhead ozone column of 300 du, a surface albedo of 0.1, and using a known elevation of 209 m above sea level near York University (43.77 °N, 79.50 °W). Several other assumptions were necessary; we assumed the initial concentrations of $ClNO_2$, Cl_2 and NO_2 to be fixed (1 ppb, 300 ppt, and 1 ppb respectively), we set the relative humidity (RH) at 50%, and we assumed that the rate of chlorine loss to a surrogate hydrocarbon mix is equal to the rate of the reaction of Cl with ethane, with a total ethane concentration of 10 ppb in the model, excluding methane at 2 ppm. This totalled value for larger non-methane hydrocarbons (NMHC) is only an estimate and will vary with pollution levels, which in turn will affect our resultant ClO (Jacob, 1999; Baker et al., 2010). The AcuChem program generated a number density (molec cm^{-3}) vs. time (s) output for all species over a period of 6 hours in the morning, our preliminary peak observation window.

2.1.2: AtChem Online + Master Chemical Mechanism (MCM)

Next, a somewhat more complex and comprehensive modeling software, AtChem on-line v1.5, running the Master Chemical Mechanism (MCM) v.3.3.1 was used. Developed at the University of Leeds, the MCM comprises a large collection of tropospheric gas-phase reactions involved in the degradation of primary VOCs (Jenkin et al., 1997; Saunders et al., 2003). However, it considers the chlorine radical initiated transformations of alkanes only and most crucially, the inorganic species and reactions we require are excluded. Therefore, a select set of thermal chlorine-based reactions and their associated temperature-dependant rate constant equations, adapted from a MCM modeling study of $ClNO_2$ by Riedel et al. in 2014, were incorporated into the model alongside a core subset of the existing MCM.

These reactions and rates are listed in **Table 2.1** and the complete model input in FACSIMILE format has been made available in **Appendix A2**. This input was contained in a mechanism file and a file of initial concentrations in which we set $ClNO_2$, Cl_2 and NO_2 values identical to the prior model. This round of modeling was performed with several advantages over what was done previously. In contrast to the AcuChem model which was compiled from the ground up, the MCM equipped us with a framework of reactions to build upon. Of particular importance, we were able to specify a start date/time (and location) within the settings and photolysis rates were not defined with respect to a single time of day, allowing us to run the model continuously. The AtChem web tool also provided the option of specifying additional environmental variables and model constraints. For consistency and simplicity, the [M], temperature and relative humidity remained constant, but these parameters were easily varied if desired and the opportunity to take into account factors such as boundary layer height among others was available. A start time (21 600 s / 6:00 AM), number of steps (360) and step size (60 s) were entered, effectively running the model from 6:00 AM to noon, on March 21 2016 at York University (43.77 °N, 79.50 °W). The results of the simulations were contained in concentration output files. The effects of varying model runs with both the AcuChem and AtChem + MCM models will be presented in Chapter 3.

Table 2.1: The modified portion of the AtChem + MCM model, composed of key inorganic chlorine reactions and associated rates. Photolysis J values are defined based on those already in the MCM. The complete input in FACSIMILE format is available in Appendix A2. Adapted from "An MCM modeling study of nitryl chloride ($ClNO_2$) impacts on oxidation, ozone production and nitrogen oxide partitioning in polluted continental outflow," by T.P. Riedel et al., 2014, ACP, 14, p. 3789–3800.

Reaction	**Rate k**
$ClNO_2 + hv \longrightarrow Cl + NO_2$	$J_{NO2 + hv \rightarrow NO + O}$ / 30
$HCl + OH \rightarrow Cl + H_2O$	2.6e-12*exp(-350/T)
$Cl + O_3 \longrightarrow ClO + O_2$	2.8e-11*exp(-250/T)
$ClO + NO \longrightarrow Cl + NO_2$	6.2e-12*exp(295/T)
$ClO + HO_2 \longrightarrow HOCl + O_2$	2.2e-12*exp(340/T)
$ClO + NO_2 \longrightarrow ClONO_2$	2.3399e-12 (298 K)
$ClONO_2 + hv \longrightarrow Cl + NO_3$	$J_{H2O2 + hv \rightarrow 2\ OH}$ * 5.4
$ClONO_2 + hv \longrightarrow ClO + NO_2$	$J_{H2O2 + hv \rightarrow 2\ OH}$ * 1.1
$HOCl + hv \longrightarrow Cl + OH$	$J_{H2O2 + hv \rightarrow 2\ OH}$ * 37
$Cl_2 + hv \longrightarrow 2\ Cl$	$J_{HCHO + hv \rightarrow CO + 2\ HO2}$ * 75

2.2: Experimental: Differential Optical Absorption Spectroscopy (DOAS)

2.2.1: Rationale

In this study, DOAS is the primary spectroscopic technique used to qualify and quantify our species of interest. DOAS is regularly employed to measure a variety of trace gases having unique absorption features less than ~10 nm in width in the UV-Vis, as presented in **Figure 2.1**, with ClO and SO_2 among these molecules (Platt and Stutz, 2008). The detailed characteristic UV absorption cross-sections of ClO and SO_2 are provided in **Figure 2.2** and **Figure 2.3** respectively (Finlayson-Pitts and Pitts, 2000).

The DOAS technique is generally suitable for the measurement of free radicals with high (ppt) sensitivity (Platt and Stutz, 2008). Under this assumption, we approached the task of detecting ClO optimistically, with the belief that it is potentially measurable, in principle, using a UV-Vis spectrometer having a sufficiently low spectral range and one or more types of DOAS instruments.

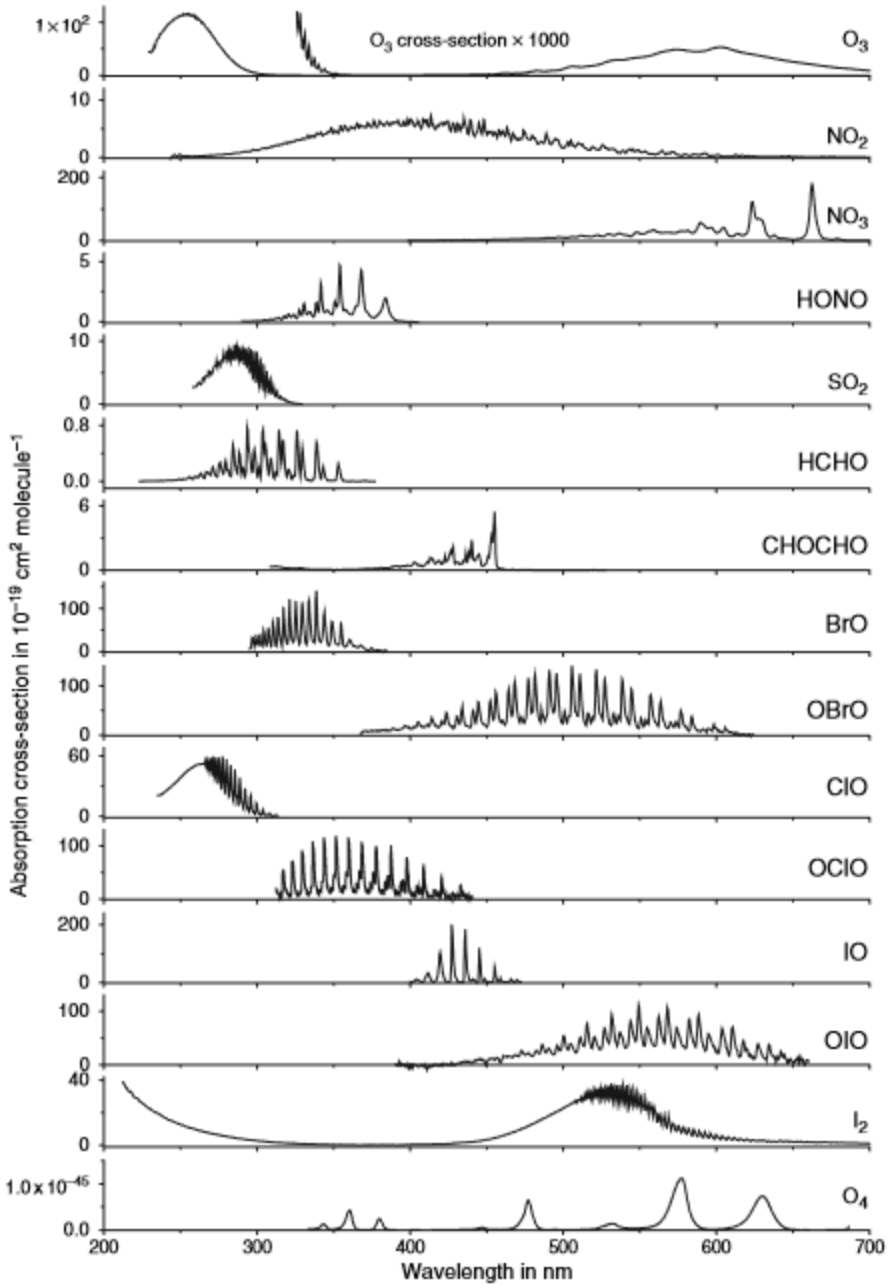

Figure 2.1: The UV-Vis absorption spectra of atmospheric species measured by DOAS. Adapted from "Differential Optical Absorption Spectroscopy: Principles and Applications," by U. Platt and J. Stutz, 2008, Springer-Verlag Berlin Heidelberg.

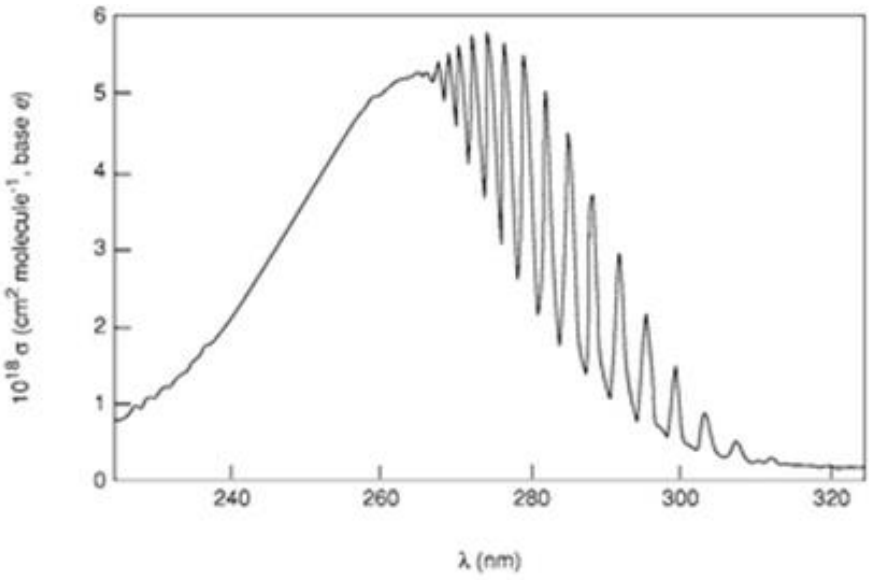

Figure 2.2: The UV absorption spectrum of ClO. Adapted from "Chemistry of the Upper and Lower Atmosphere: Theory, Experiments, and Applications," by B.J. Finlayson-Pitts and J.N. Pitts Jr., 2000, Academic Press, San Diego, CA.

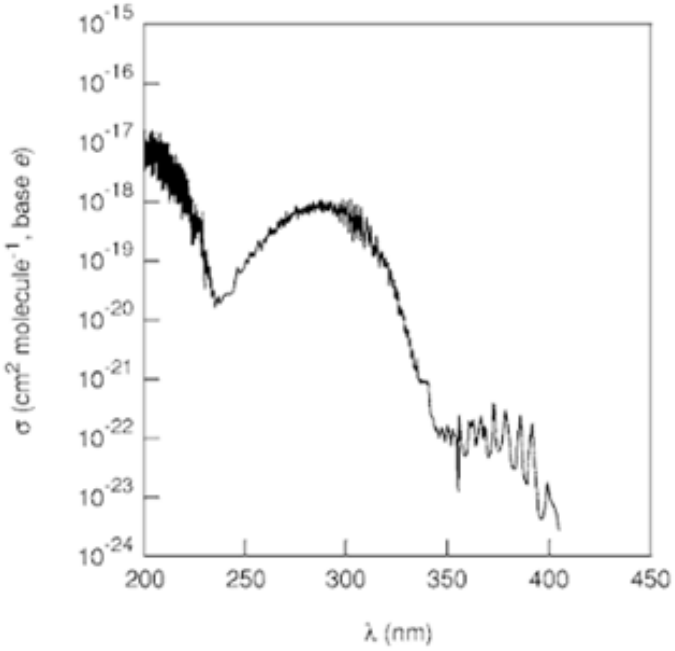

Figure 2.3: The UV absorption spectrum of SO_2. Adapted from "Chemistry of the Upper and Lower Atmosphere: Theory, Experiments, and Applications," by B.J. Finlayson-Pitts and J.N. Pitts Jr., 2000, Academic Press, San Diego, CA.

There are multiple configurations of DOAS systems that transmit and/or receive light through the atmosphere, each one advantageous for various purposes. They are largely categorized into two

modes based on light source; active and passive. Active forms of DOAS use a continuous artificial light source while passive techniques rely on natural light such as sunlight or moonlight. We utilize two types of DOAS to our advantage; active long-path DOAS with a lamp and a passive Multi-Axis (MAX-DOAS) instrument, with sky-scattered sunlight as its light source. The preference for MAX-DOAS is that it records spectral data at multiple elevation angles in order to determine the vertical distribution of the target species (Platt and Stutz, 2008). These two setups were chosen because they would allow us the freedom to measure ClO at surface-level and at higher altitudes, at different times of day, and under different sky conditions. Both active and MAX-DOAS systems are described in detail in the following sections.

2.2.2: Instrumental Setup of Active & MAX-DOAS

Active DOAS

The design of the active DOAS instrument used in this work is illustrated in the diagram in **Figure 2.4**. This particular instrument consists of a double coaxial Cassegrain telescope with joint transmitting and receiving optics within its interior. Light is emitted from a Xenon (Xe)-Arc lamp in the focal plane of a primary mirror in the telescope, with the primary and secondary mirrors collimating the outgoing beam. Alternatively, a Deuterium (D)-Arc lamp, broadband laser or light emitting diode (LED) may be used as the light source in other systems (Platt and Stutz, 2008). It is aligned to a retroreflector placed at a distance from the active DOAS instrument, with a typical light path ranging from hundreds of meters to several kilometers. The retroreflector directs the light beam back into the telescope where it is focused onto an optical fibre, detected by a spectrometer and stored on a computer for later analysis. With active DOAS, we obtain the average concentration of an absorber along an open but well-defined path in the atmosphere.

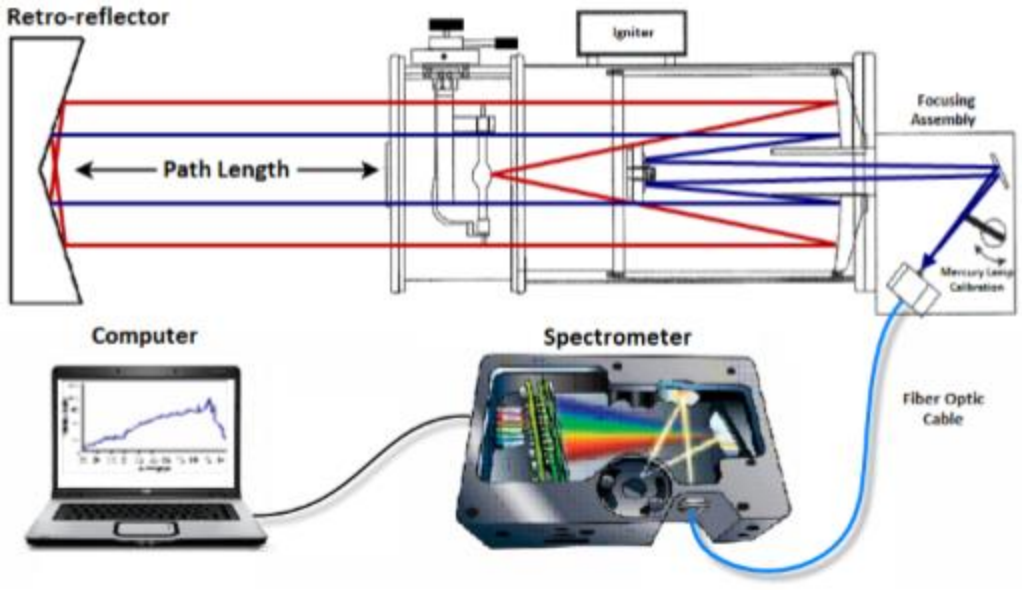

Figure 2.4: Schematic diagram of an active DOAS system. The outgoing and incoming light beams are traced in red and blue, respectively.

MAX-DOAS

The schematic of a Mini MAX-DOAS instrument is illustrated in **Figure 2.5**. Relatively compact in size, the receiving optics, fibre coupled spectrometer, temperature controls, and all electronics are contained within a sealed metal box. An exterior stepper motor rotates the instrument to a selected viewing angle and incident light enters past a black tubular shield that restricts the field of view to 0.6°, through a lens in the telescope to reach the fibre. In contrast to active DOAS, the path is less defined and analysis yields the slant column density (SCD) of an absorber, with radiative transfer calculations needed for conversion into a tropospheric or total vertical column density (VCD) (Bobrowski and Filsinger, 2005).

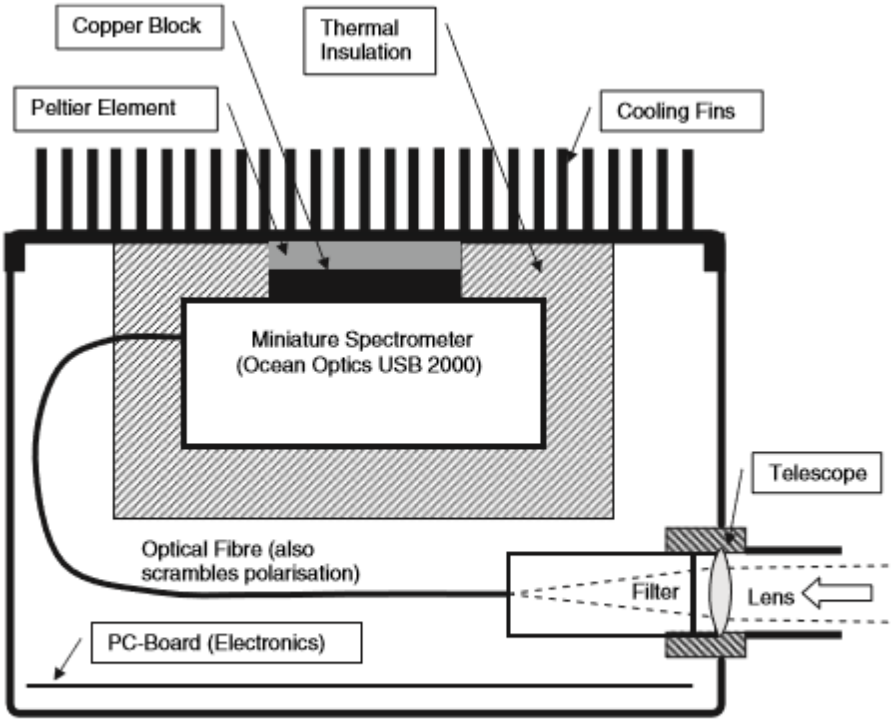

Fig. 7.53. Schematic cross-section through a miniature MAX-DOAS system (Bobrowski, 2005). The entire instrument, including the telescope, can be pointed to any elevation between horizon and zenith

Figure 2.5: Schematic diagram of a Mini MAX-DOAS instrument. Adapted from "Differential Optical Absorption Spectroscopy: Principles and Applications," by U. Platt and J. Stutz, 2008, Springer-Verlag Berlin Heidelberg.

2.2.3: DOASIS Fitting Procedure

Ambient atmospheric spectra were collected with the active and MAX-DOAS instruments and analyzed using the DOASIS software package developed by the Institute of Environmental Physics at the University of Heidelberg. The measured spectra were fit against those of the target species and any other trace gases that absorb in the same wavelength region. The DOASIS spectral analysis software utilizes a combination of a standard linear least squares fit to retrieve trace gas absorptions and a non-

linear Levenberg-Marquardt algorithm to account for spectral shifts between a measured spectrum and a reference, in an effort to minimize the residual of the fit (Platt and Stutz, 2008). The high resolution absorption cross sections used as reference spectra in fitting, those for ClO, SO_2, and O_3, were retrieved from the MPI-Mainz UV-Vis Spectral Atlas of Gaseous Molecules of Atmospheric Interest (Keller-Rudek et al., 2013) and are summarized in **Table 2.2**. These reference spectra were incorporated within a fit scenario alongside a spectrum of the light source in the case of active DOAS. For MAX-DOAS, we require additional components due to the presence of Fraunhofer lines in the solar spectrum caused by gases absorbing in the Sun's photosphere. A Fraunhofer reference spectrum (FRS) is necessary; one collected at a small solar zenith angle and high elevation angle to have minimum absorbers, typically a 90° zenith spectrum at noon. We require a ring spectrum as well, generated in DOASIS, which accounts for the filling in of the Fraunhofer lines at larger solar azimuth angles due to inelastic rotational Raman scattering, the effects of which can be an order of magnitude larger than the weaker absorptions of trace gases, a phenomenon known as the Ring Effect (Bobrowski and Filsinger, 2005). Fitting also requires the collection and processing of electronic offset, dark current and calibration spectra, the details of which are provided in the following section. For ease of use, JScript files were compiled to automate the fitting of large sets of data. Adjustments to the standard fitting procedure were required and will be discussed in depth in Chapter 4. The DOASIS software computes the column density in units of molecules cm^{-2}, along with an associated fit error for each species. For MAX-DOAS, this is a slant column density (SCD) that is differential with respect to the FRS. For active DOAS, the value may be converted into a concentration number density through dividing by the path length and subsequently to a mixing ratio by further dividing by the number density of air at a given temperature and pressure.

Table 2.2: The key absorption cross sections used in this study. In all instances, the spectral resolution is greater than the resolution of our DOAS instrument. DOASIS conversion from vacuum to air conditions was required for the SO_2 and O_3 cross sections.

Species	Author & Year	Temperature	Wavelength Range & Resolution
ClO	SanderFriedl, 1989	298 K	244 - 317 nm, 0.07 nm
SO_2	Bogumil, 2003	293 K	239 – 395 nm, 0.21 – 0.22 nm
O_3	Bogumil, 2003	293 K	230 – 1070 nm, 0.24 nm in the ClO fit range (channel dependant)

2.2.4: Correction, Calibration & Lamp Spectra

Electronic Offset & Dark Current Noise

An electronic offset and dark current (DC) signal may be present in an optical detector when no radiation is admitted into the device. A baseline offset is added to the signal to avoid negative values in the analog to digital (A/D) converter. The offset signal of the OceanOptics USB2000 spectrometer is temperature dependant, decreasing with increasing temperature. To obtain reliable statistical mean offset spectra, we record a large number of averages and use a small integration time to minimize

effects of dark current (Bobrowski and Filsinger, 2005). The dark current (DC) is caused by thermally excited electrons in the CCD detector and is variable from pixel to pixel. DC is temperature dependant as well, increasing exponentially with increasing temperature. We collect DC spectra using a large integration time, as the signal is proportional to the exposure time (Platt and Stutz, 2008). In practice, we must record offset and DC spectra with no light entering the spectrometer and with appropriate acquisition parameters for each. The fibre optic cable was removed from the active DOAS instrument and capped, and the MAX-DOAS instrument was immersed in darkness. Offset spectra were generally taken with a 3 ms integration time and 10,000 averages, while for DC spectra, we used a 30,000 ms integration time and 1 average, for both active DOAS and MAX-DOAS. Sample offset and DC spectra for active DOAS measurements are provided in **Figure 2.6** and **Figure 2.7**, respectively, and are similar to those for MAX-DOAS. We subtract these two spectra from every other spectrum taken with our spectrometer prior to fitting.

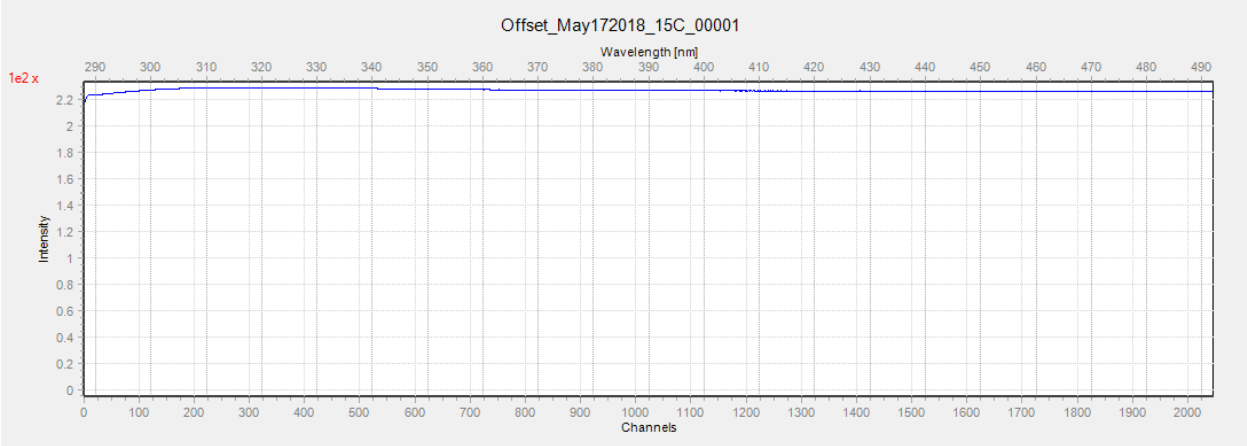

Figure 2.6: Sample offset spectrum collected on May 17 2018 with a 3 ms integration time and 10,000 averages, using the active DOAS USB2000 spectrometer, temperature stabilized to 288 K / 15 °C / 59 °F.

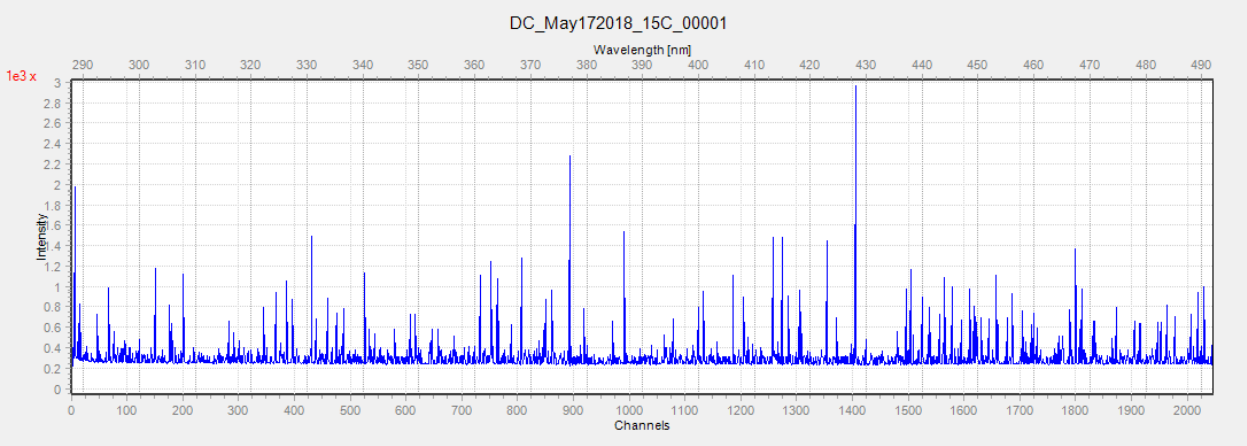

Figure 2.7: Sample dark current (DC) spectrum collected on May 17 2018 with a 30,000 ms integration time and 1 average using the USB2000 spectrometer temperature stabilized to 288 K / 15 °C / 59 °F.

Initial subtraction of the offset signal and normalization of integration time with respect to each minuend spectra is required.

Mercury (Hg) Lamp: Spectral Calibration & Convolution

The spectrum of a mercury (Hg) lamp was collected for two purposes; wavelength calibration and convolution of reference spectra. Consisting of several discrete emission lines at well-known wavelengths, those appearing at 302.50 nm, 313.17 nm and 334.15 nm were used, as they fall into and around the ClO and SO_2 fit ranges. In similar applications, other metal and noble gas lasers are often employed, neon or cadmium being the most common (Platt and Stutz, 2008). Each of the peaks was fit to a Gaussian, the center of which was used for calibration. The calibration function was determined using a 3rd order polynomial and applied to all spectra to correct any wavelength misalignment. Furthermore, because the absorption cross sections sourced are of higher resolution, we must replicate the resolution of our spectrometer in order to create suitable reference spectra for fitting, a practice known as convolution. Once again, the instrument function of the spectrometer at a given temperature may be approximated by the full width half maximum (FWHM) of an atomic emission line in the fit range (Bobrowski and Filsinger, 2005). We thereby use the Hg spectrum to both shift and squeeze spectra in wavelength space (Platt and Stutz, 2008). To obtain the Hg spectrum, we simply expose the active DOAS fibre optic or the entrance optics of the MAX-DOAS to light from a Hg lamp in the absence of all external light. The resultant spectrum, taken with a 250 ms integration time and 2,000 averages for active DOAS, or a 5 ms integration time and 2,000 averages for MAX-DOAS, is shown in **Figure 2.8**.

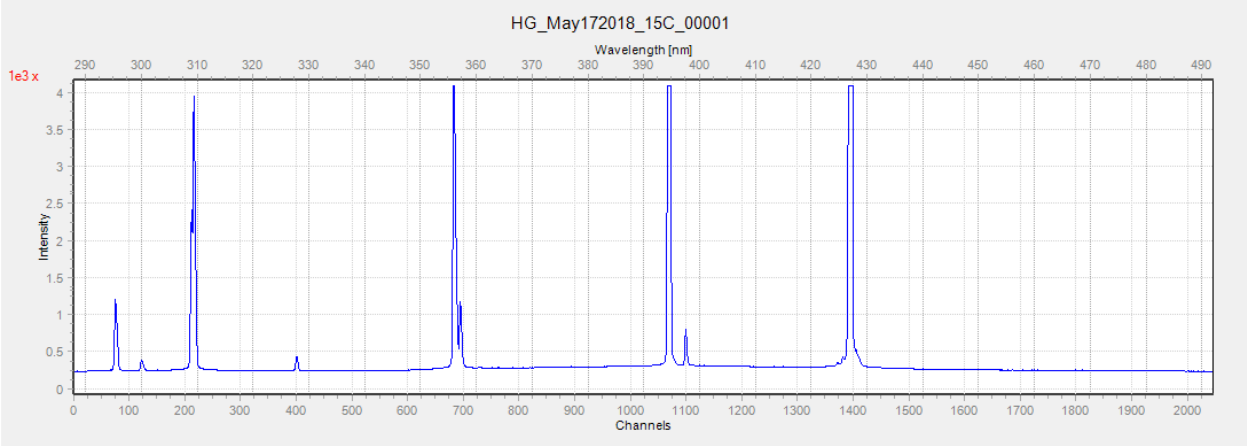

Figure 2.8: Sample mercury (Hg) spectrum collected on May 17 2018 with a 250 ms integration time and 2,000 averages, using the active DOAS USB2000 spectrometer, temperature stabilized to 288 K / 15 °C / 59 °F.

Xenon (Xe) Lamp

In the case of active DOAS, the spectrum of the light source was incorporated into the fit in the form of a lamp reference spectrum. Its collection required the focusing of reflected light originating from the lamp only, without first traversing the atmosphere, onto the fibre optic opening. A standard high pressure Xe-Arc lamp emits a Planck spectrum corresponding to black body radiation at 6000 -

8000K, giving rise to high light intensities and a smooth spectrum in the UV (Platt and Stutz, 2008). The lamp spectrum was recorded using an integration time of 250 ms with 2,000 averages. An example spectrum is shown in **Figure 2.9**.

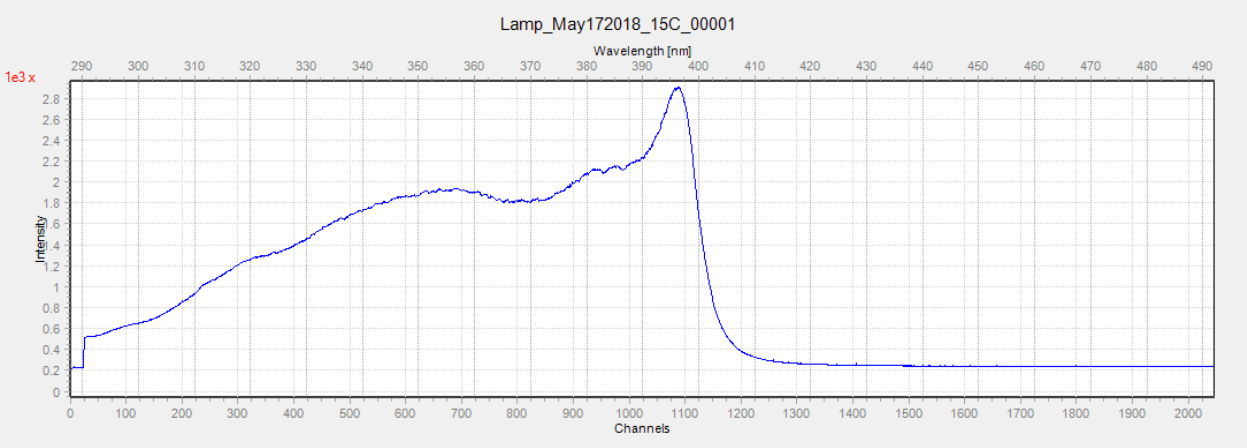

Figure 2.9: Sample lamp spectrum collected on May 17 2018 with a 250 ms integration time and 2,000 averages, using the USB2000 spectrometer temperature stabilized to 288 K / 15 °C / 59 °F.

2.3: York University Measurements

2.3.1: Active DOAS

Overview

The location for the bulk of this study was York University's Keele Campus (43.77 °N, 79.50 °W), an urban center in the large city of Toronto, Ontario, Canada, in close proximity to high-traffic roadways and other sources of air pollution. The active DOAS instrument was positioned in the penthouse lab of the Petrie Science and Engineering Building, at an elevation of approximately 13.4 m above ground-level, pointing out of a north-facing window. A retroreflector was placed under the overpass of nearby Highway 407, about 5 m off ground-level and at a distance of approximately 2 km, or 4 km total return pathlength. A map of the area pinpointing the exact location of the active DOAS instrument and the retroreflector is provided in **Figure 2.10**. This site was selected as it offered us a long path length for increased ClO sensitivity, with the added benefit of neighbouring highway emissions. In addition, the overpass served to shield the mirror from the elements and a concrete wall was thought to help deter sunlight surrounding the retroreflector from entering the telescope. The retroreflector was cleaned as necessary to ensure dust and debris on the glass was not causing light attenuation. A dashboard camera pointing out of an east-facing window in the lab was used to monitor sky conditions 24/7 to record instances of interference by rain, snow, or fog and in later measurements, to ensure skies were clear for the duration of spectra collection. These video clips were archived.

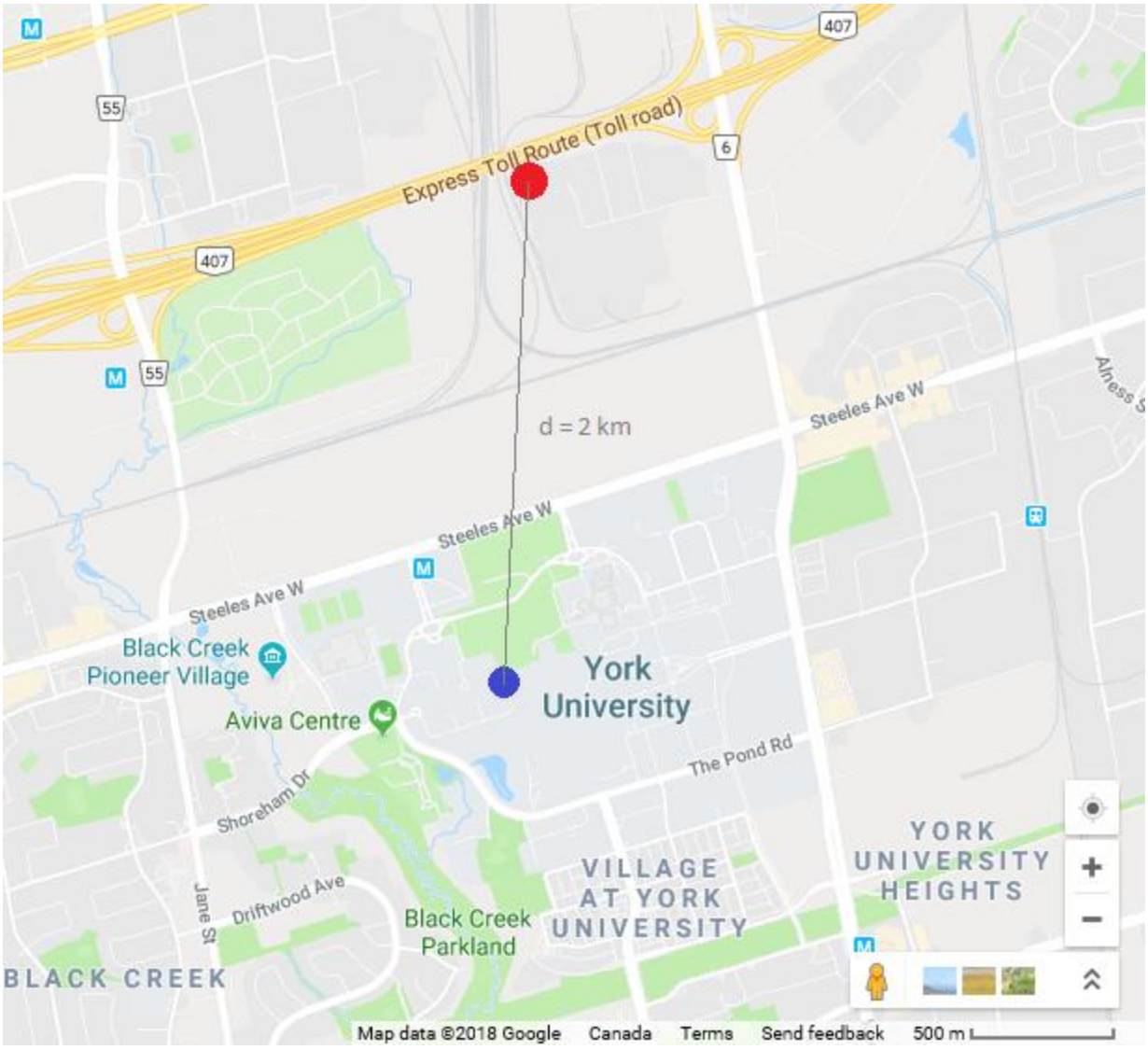

Figure 2.10: Map displaying the location of the active DOAS in the Petrie Science & Engineering Building on the York University campus (blue dot) and the retroreflector located 2 km away, under the overpass of Highway 407 (red dot).

Technical Details

The active DOAS instrument used in this study was a modified Thermo Environmental Instruments Inc. DOAS 2000® equipped with a Hamamatsu Photonics L2274 high pressure 150 Watt Xe-Arc lamp and an 8" primary mirror. The telescope was oriented such that the beam of light traveled a defined path through the lower atmosphere to an aluminum 30 x 2"corner cube retroreflector. Photos of our instrument and retroreflector are provided in **Figure 2.11** and **Figure 2.12**, respectively. The return light was focused onto an Ocean Optics UV-Vis high OH content fibre optic cable with a 600 µm core diameter, operating most efficiently in the 300-1100 nm wavelength range as per manufacturer recommendations. The fibre optic cable was woven through a grating to reduce the effects of

turbulence noise and then connected to an OceanOptics USB2000 spectrometer (Grating #10, 2048 pixels, 25 µm slit, wavelength range: 287.8-492.1 nm) used in conjunction with SpectraSuite operating software. A 25 mm quartz shortpass filter with a 400 nm cut-off wavelength was used in order to reduce stray light in the spectrometer (Platt and Stutz, 2008).

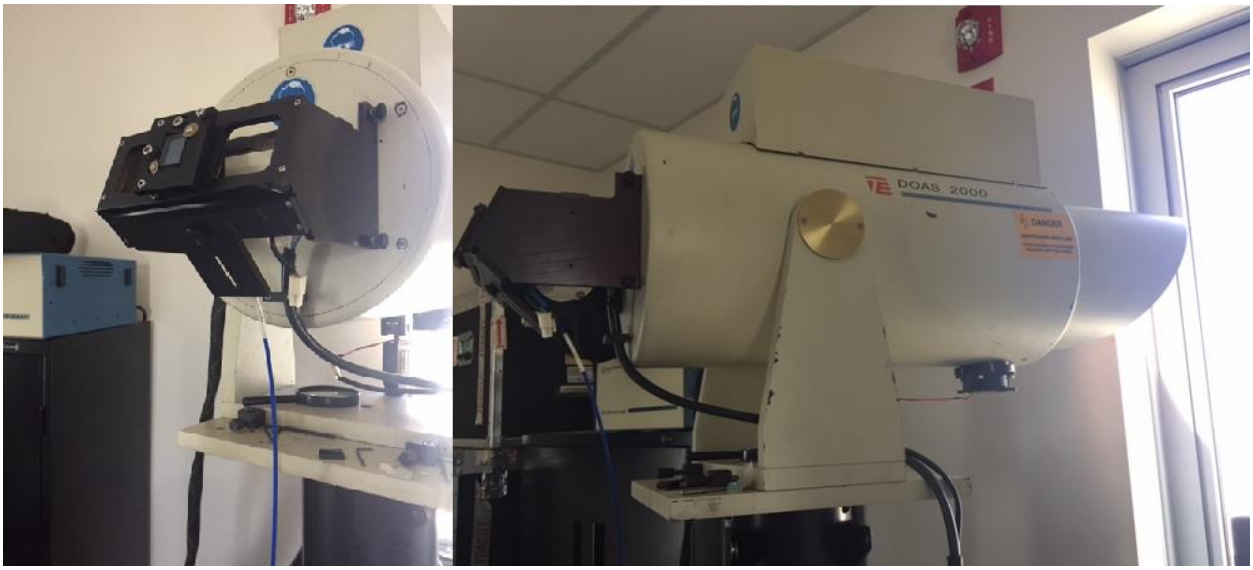

Figure 2.11: Back and side views of the active DOAS instrument (Thermo Environmental Instruments Inc., DOAS 2000®). The telescope connects to a lamp power supply (not pictured).

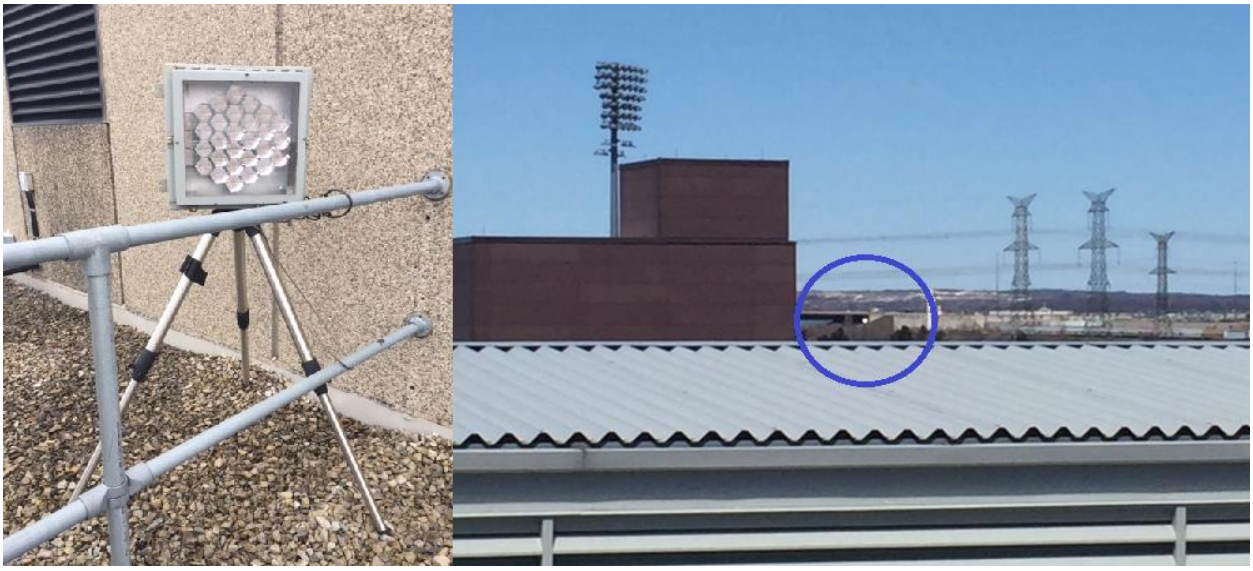

Figure 2.12: (Left) The aluminum 30 x 2”corner cube retroreflector used in our study. (Right) The view of the retroreflector from the active DOAS instrument in the penthouse lab. A bright return light (circled) was visible at all times.

It is important to note that the spectrometer was thermally controlled during its operation. A temperature controlling unit (Resonance Ltd.) housed the spectrometer between a metal plate and an

8” PC case cooling fan, as pictured in **Figure 2.13**. It was used to keep the temperature steady to about ± 0.2 degrees of a fixed temperature of either 283 K (10 °C / 50 °F) or 288 K (15°C / 59 °F) during spectra collection. The set temperature was somewhat arbitrary, selected to be 10 °C - 13 °C below the ambient temperature in the lab. This was to facilitate optimum cooling, owing to the lack of a heating element in addition to the Peltier cooler in the unit. The temperature controller was operated with HyperTerminal software, a terminal emulator with the output window shown in **Figure 2.14**. This temperature regulation was essential in order to minimize spectral shifts that would otherwise degrade the accuracy of the instrument (Platt and Stutz, 2008). Full data showing fair adherence to the set temperature is available, however, there was a slight drift at certain times and the possible repercussions of any temperature variation that may have occurred will be discussed in detail.

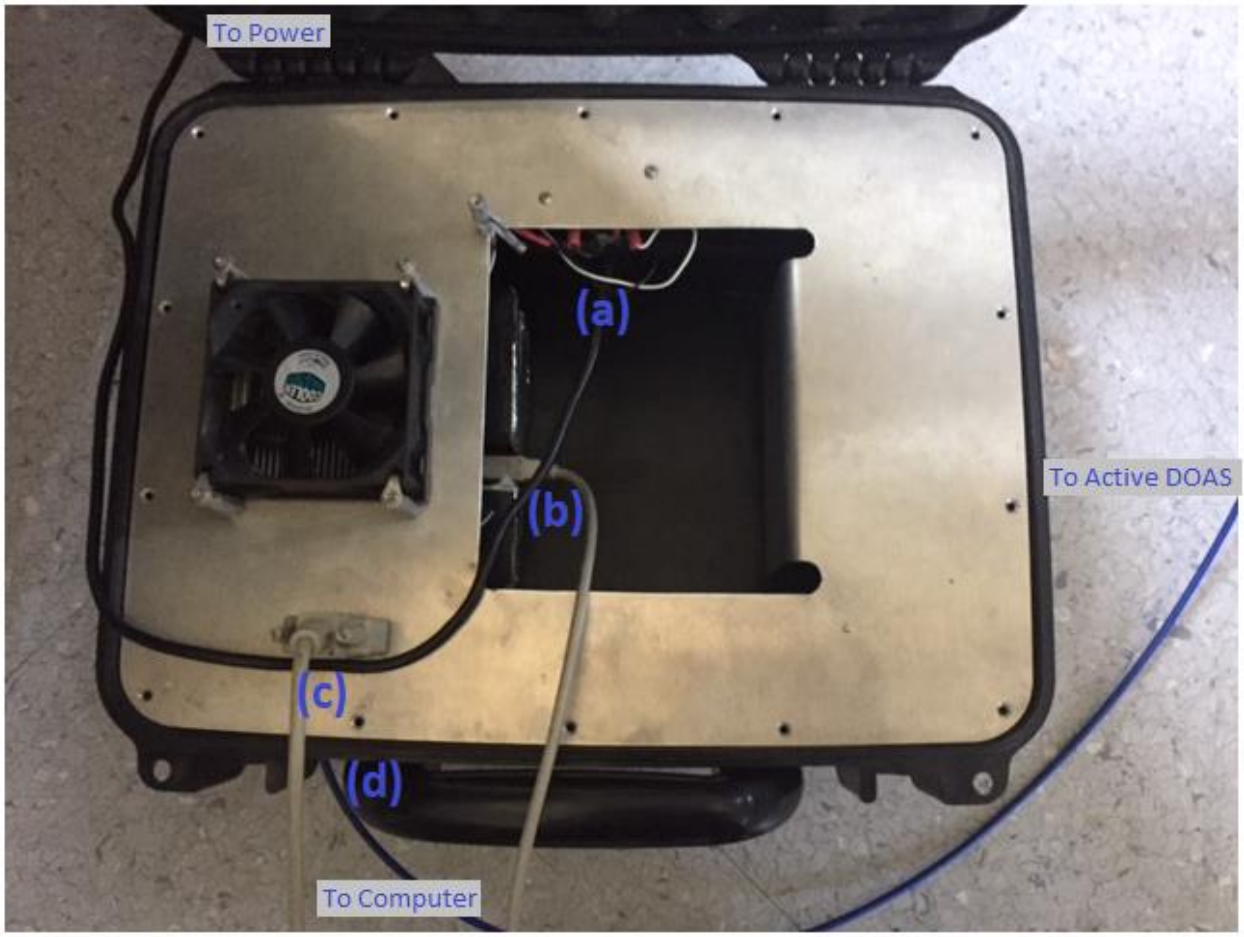

Figure 2.13: The Resonance Ltd. temperature controlling unit with all connections intact. The spectrometer (not visible) is located below the fan. In this diagram, the power cord for the unit is labelled (a), cables (b) and (c) are connected to the spectrometer and to the unit, respectively, and link to a computer through a USB input. The blue fibre optic cable (d) is inserted into the spectrometer and leads to the active DOAS instrument.

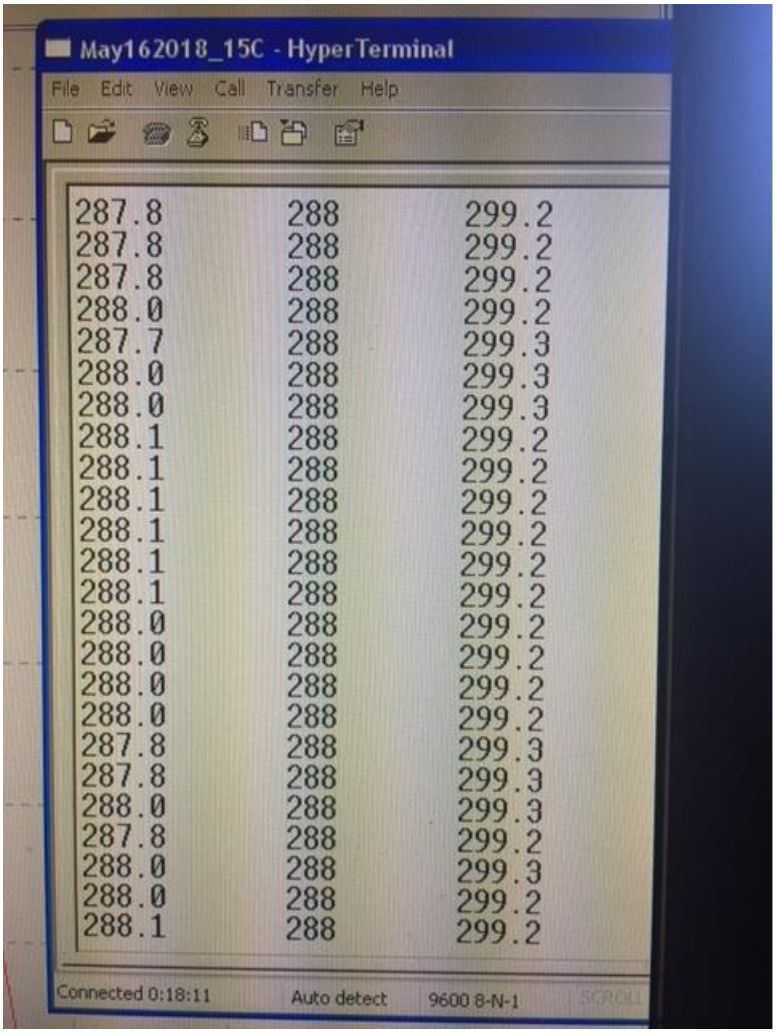

Figure 2.14: The output window of the Resonance Ltd. temperature controlling unit. The first column logs the temperature of the spectrometer, the second column displays the set temperature and the third column represents the ambient temperature in the lab, in units of Kelvin.

A series of raw atmospheric spectra were collected, with a typical example spectrum provided in **Figure 2.15**. One measurement spectrum was recorded every 8.3 minutes using a 250 ms integration time and 2,000 averages. These acquisition parameters were selected to maximize light intensity over a long path length while optimizing the time resolution of the data. Following the collection of measurement spectra, a lamp spectrum, noise correction (offset and dark current) and a calibration (mercury lamp) spectrum were routinely collected at the same temperature, immediately following morning measurement sets or the day after for 24-hour measurement sets. As a final step, initially performed as a precautionary measure, but later discovered to be integral in fitting, background spectra were collected on a select few days in-between the collection of measurement spectra. These background spectra were recorded on clear days with the lamp turned off to account for any residual scattered sunlight entering the telescope (Platt and Stutz, 2008). In appearance, they resembled a weak measured spectrum during the day and a dark current spectrum at night. In calculating the final mixing

ratios, we used the number density of air at a temperature of 0°C (2.69×10^{19} molec cm^{-3}) and a path length of 400,000 cm.

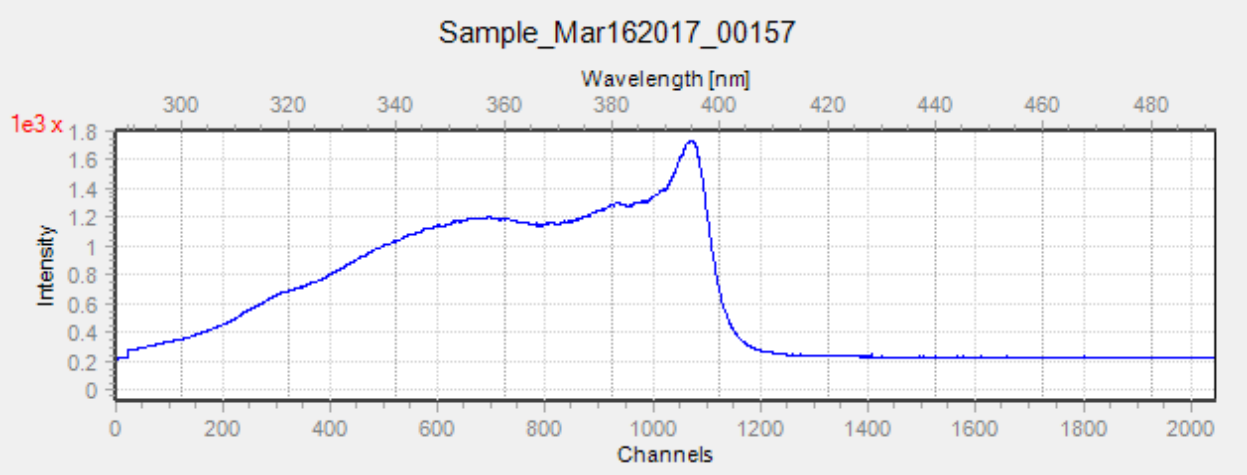

Figure 2.15: Sample active DOAS measurement spectrum collected on March 16 2017 with a 250 ms integration time and 2,000 averages, temperature stabilized to 288 K / 15 °C / 59 °F. All spectra display light intensity (in counts) over the spectrometer's spectral range (287.8-492.1 nm).

2.3.2: MAX-DOAS

Overview

A MAX-DOAS instrument was employed in the same location, functioning under the same guiding principles as the active DOAS. However, this type of DOAS would allow us to make measurements higher up in altitude to test our original hypothesis for the presence of ClO in the residual layer early in the morning. Due to the dependence of this passive technique on sky scattered sunlight, an additional meteorological constraint of cloud free conditions was necessary. As well, our available wavelength range was reduced to a lower limit of 300 nm, limited by the available solar radiation at the Earth's surface, at the latitude of Toronto (Holloway and Wayne, 2010). The MAX-DOAS instrument was located outdoors, on the rooftop of the Petrie Science & Engineering building. It was generally positioned facing east, or from time to time west, depending on direction of cloud cover. In the wintertime, a cover was wrapped around the instrument to keep it operational in below freezing conditions. It was set to run at a temperature 5 °C – 15 °C below the lowest ambient temperature over the measurement session. A pyranometer was placed on top of the MAX-DOAS instrument during this time. It was used in conjunction with a HOBO Micro Station data logger using HOBOware software to quantitatively monitor cloud cover in addition to the visual cues from the webcam videos. It measured solar radiation intensity in units of W/m^2 over 10 second intervals, as exemplified in **Figure 2.16**. In contrast to the active DOAS, we use the DOASIS software package to operate the MAX-DOAS instrument, control the temperature, and to acquire the spectral data in addition to post-processing.

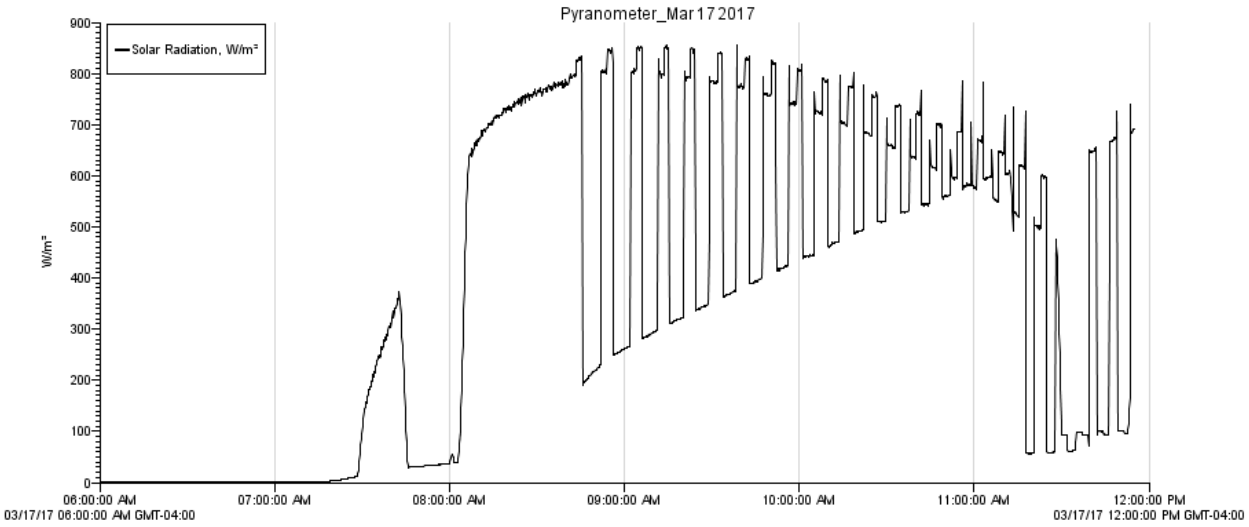

Figure 2.16: Pyranometer readout as solar radiation on the morning of March 17 2017 (Sunrise: 7:26 AM). We observe a pre-dawn value of 0 W/m^2 with high peaks during clear sunny periods and dips during episodes of cloud cover. Time is GMT-04:00 (EDT).

Technical Details

The MAX-DOAS instrument used in this study was a Mini MAX DOAS (University of Heidelberg, Hoffmann Messtechnik GmbH) comprising an internal OceanOptics USB2000 spectrometer (2048 pixels, 50 µm slit, wavelength range: 290-433 nm) controlled by OOIBase32 software. Photos of our Mini MAX-DOAS are provided in **Figure 2.17**. As before, the entrance tube was outfitted with a 25 mm quartz shortpass filter with a 410 nm cut-off wavelength. Measured spectra were collected in a cycle at elevation angles of 2°, 15°, and 90°, with a typical MAX-DOAS spectrum shown in **Figure 2.18**. Correction and calibration spectra were recorded similarly to active DOAS, now with integration times and averages built into scripts executed in DOASIS. Here, the exposure time varied depending on sunlight intensity, recording 1500 or 2000 scans at each angle.

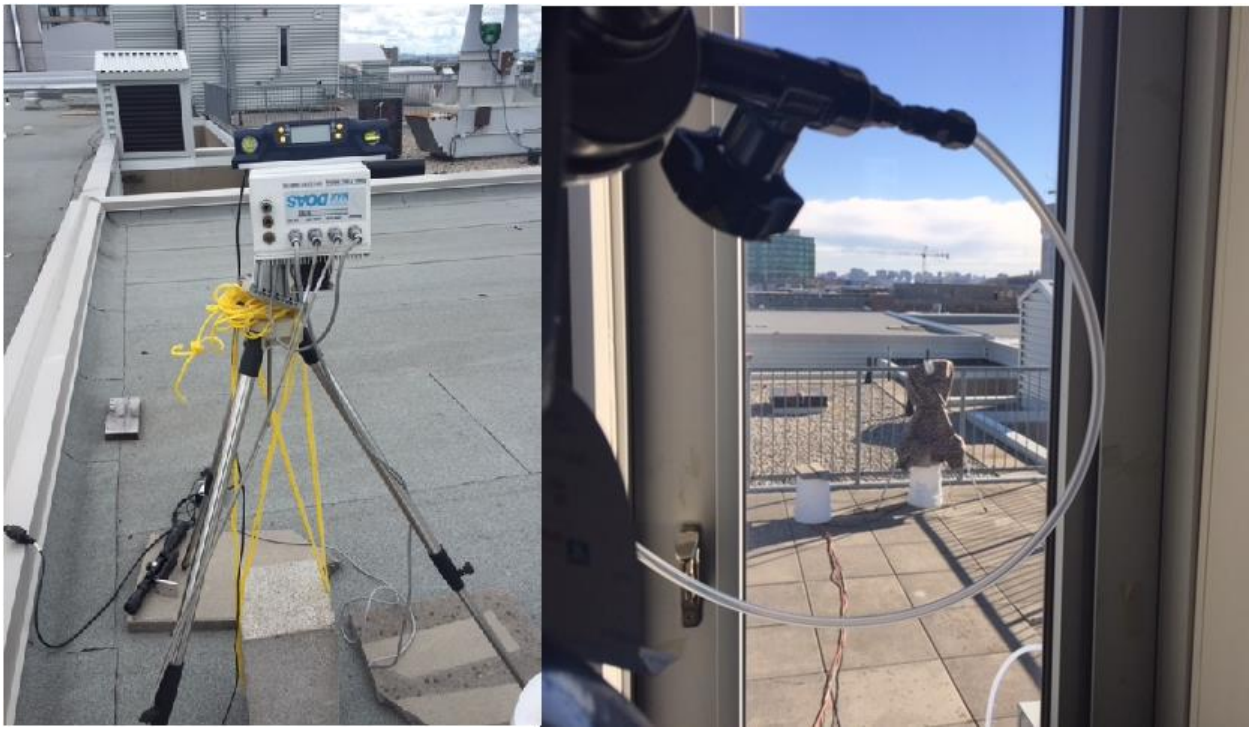

Figure 2.17: (Left) Photo of the Mini MAX-DOAS instrument mounted on a tripod (Right) The MAX-DOAS secured on site, facing eastward and measuring a 90° spectrum.

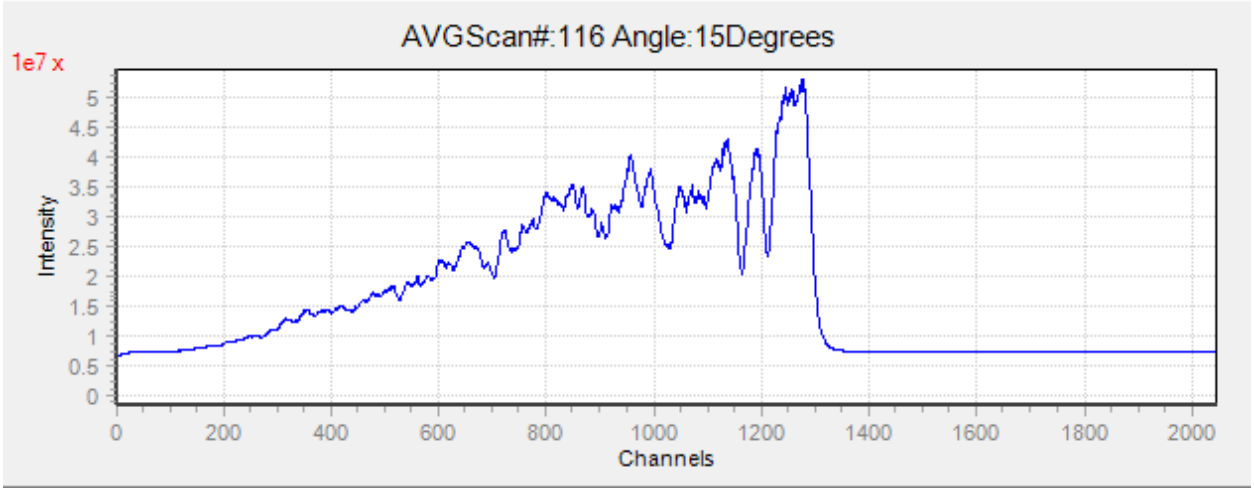

Figure 2.18: Sample MAX-DOAS measurement spectrum collected on March 17 2017 at a 15° elevation angle, temperature stabilized to 264 K / -9.5 °C / 15 °F. All spectra display sunlight intensity (in counts) over the spectrometer's spectral range (290-433 nm). Solar features are clearly visible when compared to the active DOAS spectrum in Figure 2.15.

2.4: Welland Canal Field Study

2.4.1: Overview: Location, Instrumentation & Summary of Marine Vessels

In collaboration with McLaren research group member Aida Khanbabakhani, a field study of the CO_2 and SO_2 content in ship plumes at the Welland Canal in the city of Thorold, Ontario was organized on July 31 and August 1 2017. The active DOAS, Mini MAX-DOAS, and a tunable diode laser (TDL) instrument were transported to the study area. A map of the field site and photo of the experimental set-up is provided in **Figure 2.19** and **Figure 2.20**, respectively. A schedule and description of passing ships on the two measurement days is listed in **Table 2.3**.

2.4.2: MAX-DOAS SO_2 Measurements

The role of the Mini MAX-DOAS in measuring SO_2 will be the sole focus in this report, and much of what has been discussed for measurements made at York University will apply. However, our intention here was to intercept a finite air mass rather than sample ambient air. The MAX-DOAS was oriented in such a way that it would capture a plume from marine vessels sailing up-bound or down-bound the canal, given west winds. Unfortunately, these measurement days saw intermittent cloud cover not ideal for the operation of the MAX-DOAS. Angles of 2°, 15° and 90° were used and the direction of the MAX-DOAS was routinely switched from north-facing to south-facing throughout the day, in an attempt to aim the telescope in the direction of clear patches in the sky. Although large gaps in the data render its interpretation difficult, fitting these MAX-DOAS measurements for SO_2 proved more successful than fitting for ClO at York University and for this reason, we elect to present our field study results in the upcoming sections.

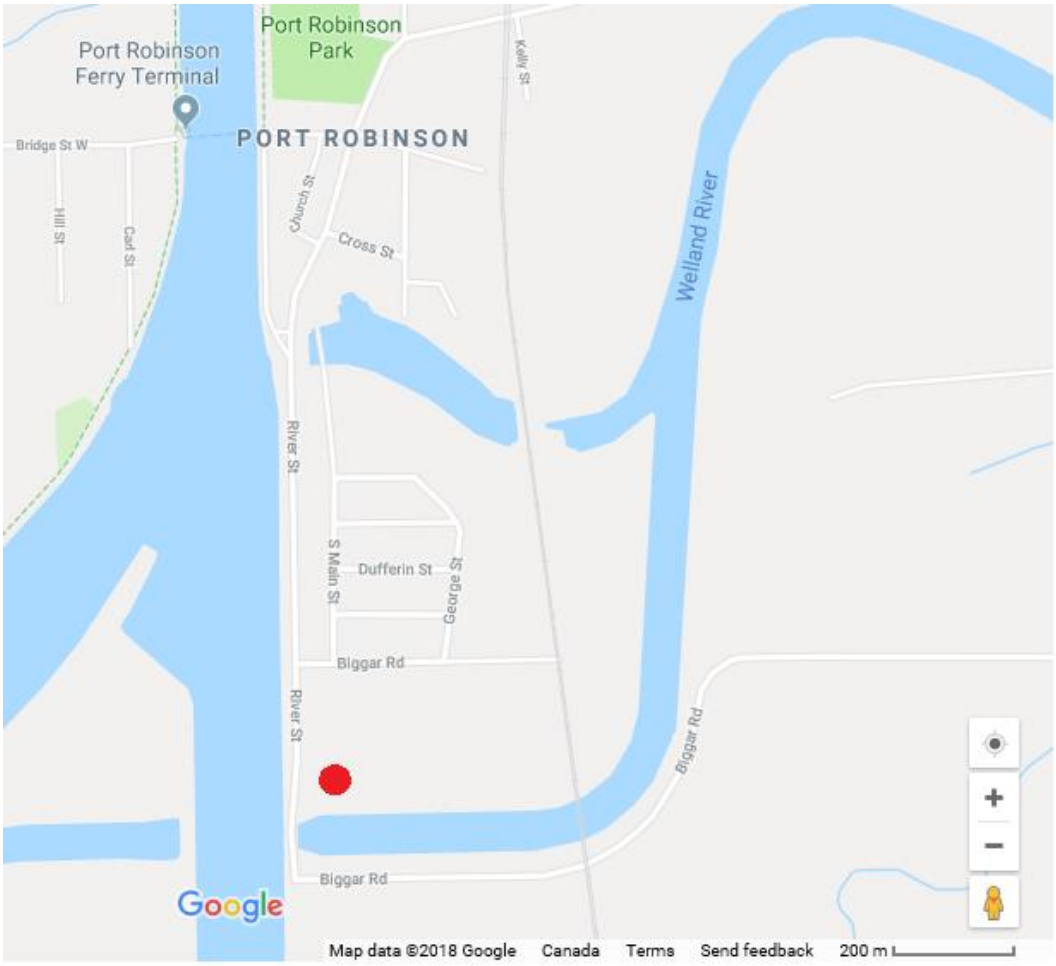

Figure 2.19: Map of the field site pinpointing the location of our instruments (red circle) relative to the passing ships on the Welland Canal to the west.

Figure 2.20: Photos of the MAX-DOAS instrument on site (left) measuring a 15° spectrum with the down-bound passing of the coast guard (right) measuring a 90° spectrum during the up-bound ascent of the largest ship, the CSL Assiniboine.

Table 2.3: A schedule and description of the marine vessels sailing past the field site by the Welland Canal on July 31 and August 1 2017.

Time (EDT)	Vessel	Direction	Dimensions
July 31 2017			
12:25 PM	Federal Kiva	Up-bound	200 m x 23.8 m
1:28 PM	Pearl Mist	Down-bound	99 m x 16.8 m
August 1 2017			
12:37 PM	Coast Guard	Down-bound	~7 m x ~5 m
12:58 PM	CSL Assiniboine	Up-bound	225.5 m x 23.8 m
2:43 PM	CSL Welland	Up-bound	225.5 m x 23.8 m
2:50 PM	Algonova	Down-bound	129.9 m x 19.8 m

CHAPTER 3: RESULTS & DISCUSSION

3.1: Modeling: Modeling Chlorine Chemistry

3.1.1: AcuChem

The AcuChem model was initialized with 1 ppb of $ClNO_2$ (Liao et al., 2014) and 300 ppt Cl_2, along with 1 ppb of NO_2 (Brown et al., 2007) to simulate reasonable starting concentrations. **Figure 3.1** displays the maximum hourly ClO concentration, illustrating the diurnal pattern of ClO over the course of the morning. According to the model, we expect to see a maximum ClO number density of 2.34×10^7 molec cm^{-3}, equal to a mixing ratio of just under 1 ppt occur around 9 AM, at a solar elevation angle of 17°. As the morning progresses, every hour sees higher photolysis rates but less $ClNO_2$ and Cl_2 remains to be photolyzed; the tipping point between the two occurs approximately 2 hours after sunrise, and this gives shape to the diurnal pattern. However, the results must be received with caution, as the model relies on many assumptions, i.e. a constant temperature of 0 °C over 6 hours and constant photolysis rates over the hour. Most importantly, it is not continuous, that is, every hour the model starts anew, with a lower initial [$ClNO_2$] and [Cl_2] from the previous run. If we run the model for the 6 hours under fixed photolysis rates (at a constant time or solar zenith angle), to obtain continuous data, these results are in **Table 3.1**. Under a mid-morning 10 AM set of photolysis rates, we obtain a maximum ClO number density of 6.29×10^7 molec cm^{-3}, equal to a mixing ratio of 2.4 ppt.

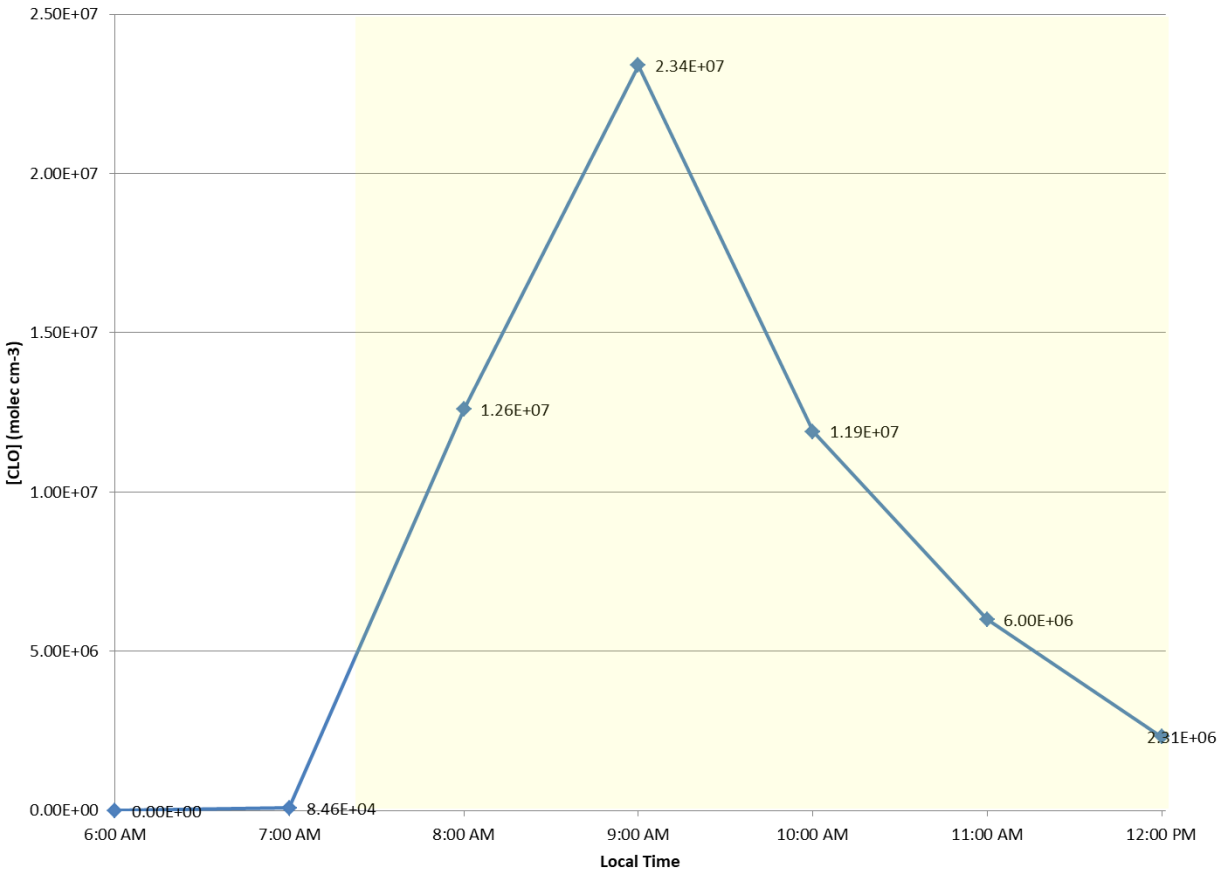

Figure 3.1: The modeled maximum hourly ClO concentration at York University on March 21 2016. Sunrise on this day was at 7:18 AM.

Table 3.1: The modeled maximum ClO concentration at York University on March 21, 2016 under the photolysis conditions of each hour/solar zenith angle.

Photolysis Conditions (Time / Solar Zenith Angle)	**[ClO]**	
	Number Density (molec cm^{-3})	Mixing Ratio (ppt)
6:00 AM / 105°	0	0
7:00 AM / 94°	8.46E+04	0.0031
7:18 AM / 91°	1.35E+06	0.050
8:00 AM / 83°	1.25E+07	0.46
9:00 AM / 73°	3.83E+07	1.4
10:00 AM / 63°	**6.33E+07**	**2.4**
11:00 AM / 54°	7.93E+07	2.9
NOON / 47°	9.27E+07	3.4

In order to observe the extent of the impact of the major chlorine source, $ClNO_2$, and the source of ClO depletion, NO_2, we performed continuous model runs, varying the initial concentrations of these two species from 100 ppt to 10 ppb. The results of the analysis are presented in **Table 3.2** and **Table 3.3**, respectively. We see that the ClO concentration maximizes under conditions of high $ClNO_2$ and low NO_2, and that it scales approximately linearly with $ClNO_2$. By assessing their impact in the model, we were able to confirm the importance of these species and their reactions in dictating the amount of ClO that may be present. If the experimentally measured ClO concentration is in line with model predictions, it may provide us with an idea of the accompanying amount of $ClNO_2$ present prior to sunrise.

Table 3.2: The effect of varying initial $ClNO_2$. Values given are those from the continuous 10 AM model. ClO concentration is observed to increase with increasing $ClNO_2$.

[$ClNO_2$] (ppt)	**[ClO]**	
	Number Density (molec cm^{-3})	Mixing Ratio (ppt)
100 ppt	6.32E+06	0.23
300 ppt	1.88E+07	0.70
1 ppb	**6.33E+07**	**2.4**
3 ppb	1.88E+08	7.0
10 ppb	6.39E+8	24

Table 3.3: The effect of varying initial NO_2. Values given are those from the continuous 10 AM model. ClO concentration is observed to increase with decreasing NO_2.

[NO_2] (ppt)	**[ClO]**	
	Number Density (molec cm^{-3})	Mixing Ratio (ppt)
100 ppt	3.94E+08	15
300 ppt	1.70E+08	6.3
1 ppb	**6.33E+07**	**2.4**
3 ppb	2.35E+07	0.87
10 ppb	6.82E+06	0.25

In considering the chlorine budget, we observe that Cl is conserved, partitioning into some ClO under favourable conditions, and into some HOCl, but nearly all of it ending up as the stable, non-radical terminal reservoir species HCl and $ClONO_2$, as per the reactions presented in the Introduction. We

observe $[Cl]_{initial} = [Cl]_{final}$ to be true in our model, with Cl originating as $ClNO_2$ and Cl_2, such that $[Cl]_{initial} = [ClNO_2] + 2[Cl_2] = 2.7E10 + 2(8.1E9) = 4.3E10$ molec cm^{-3} and $[Cl]_{final}$ finishing as HCl and $ClONO_2$, giving $[Cl]_{final} = [HCl] + [ClONO_2] = 3.8E10 + 4.9E9 = 4.3E10$ molec cm^{-3}.

The model results are in general agreement with literature values, underestimating the ClO concentration slightly, as direct observations of a few ppt were first made in the arctic boundary layer (Tuckermann et al., 1997), followed by 5–15 ± 2 ppt close to a salt lake (Stutz et al., 2002) and 8.4 ± 4.3 ppt in a mid-latitude coastal area (Lee et al., 2008). In terms of number densities, only two studies have reported direct or indirect estimates, accounting for an average daytime concentration of 10^6–10^8 molec cm^{-3} (Chang et al., 2004; Platt et al., 1995). The literature likewise describes a correlation to pollution levels (Stutz et al.,2002; Chang et al., 2004) and we see this strong ClO dependence on NO_2 in the model. Because Toronto is not located by a consistent natural salt source, a lower experimental value may be expected, unless particulate chloride is higher due to the presence of road salt or other anthropogenic sources. Further, although a $ClNO_2$ concentration of 1 ppb is possible, this may be an overestimate, particularly in a mid-continental location. In Calgary and Boulder, Colorado studies (Mielke et al., 2016; Thornton et al., 2010), only 100 to 450 ppt was observed, which may result in ClO levels too low to detect. However, measurements in the residual layer could be much higher and have infrequently been made (Osthoff et al., 2008; Young et al., 2012; Edwards et al., 2013).

3.1.2: AtChem Online + Master Chemical Mechanism (MCM)

Modeling was performed for a second time using the AtChem online platform running the Master Chemical Mechanism (MCM), allowing for continuous model runs to produce smooth and continuous curves. Once again, a constant temperature of 0 °C or 273 K was assumed and the model was initialized using 1 ppb of $ClNO_2$ and NO_2 to start. Results are displayed in **Figure 3.2**, in which we observe a similar diurnal pattern and peak mixing ratio of ClO, albeit slightly higher in magnitude at $5.16x10^7$ molec cm^{-3} (2.0 ppt) and occurring about an hour earlier in the morning, just before 8 AM, with this model. The results from varying initial $[ClNO_2]$ and $[NO_2]$ are presented in **Figure 3.3** and in **Figure 3.4**, respectively. Lastly, **Figure 3.5** illustrates the resultant concentrations of the remaining major chlorine-containing species in the model. As would be expected, $ClNO_2$ and Cl_2 are gradually depleted, HCl and $ClONO_2$ are gradually increasing, and ClO, Cl and HOCl reach a maximum sometime in the morning hours. Results of the modeling suggest that measurable levels of ClO are possible under favourable atmospheric conditions, i.e. high $ClNO_2$ and low NO_2, given the assumptions made in the modeling process are valid.

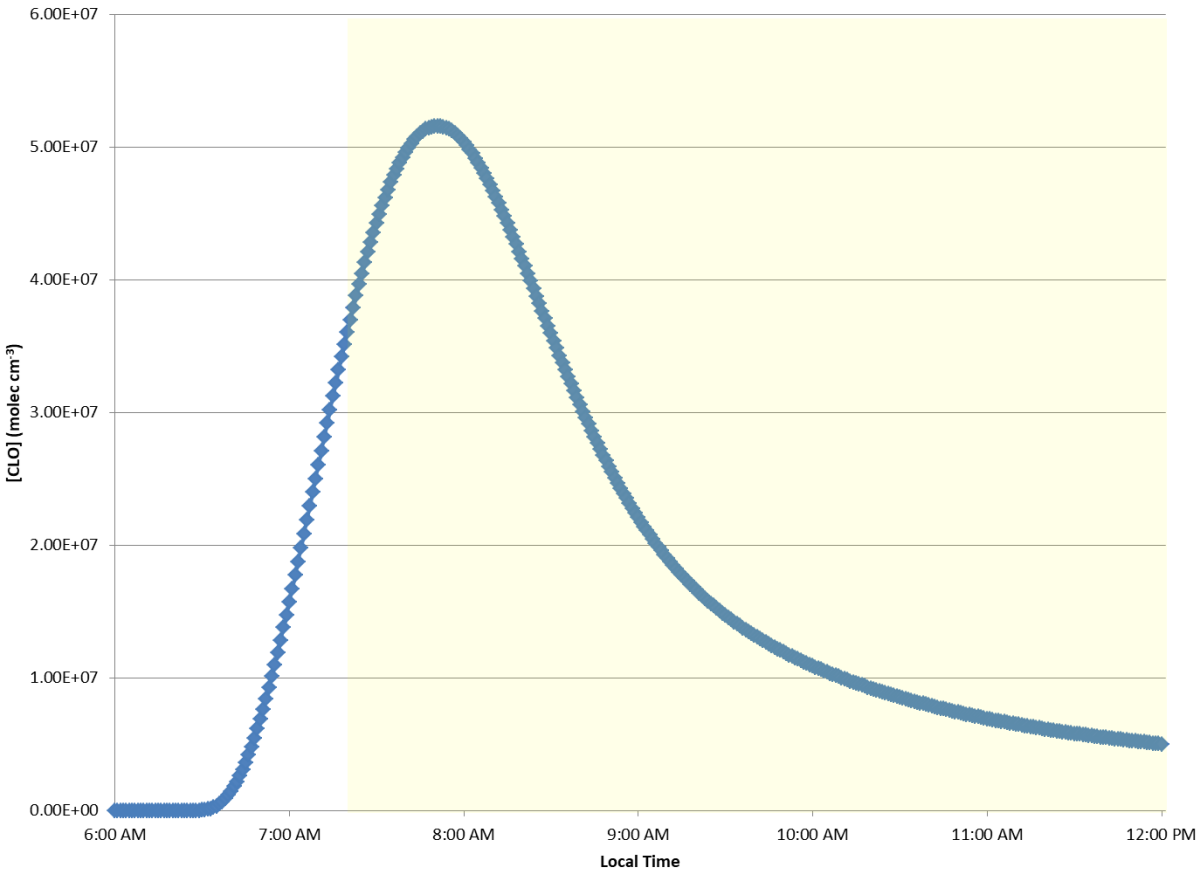

Figure 3.2: The modeled ClO concentration at York University on March 21 2016. Daylight hours indicated by yellow overlay (sunrise: 7:18 AM EDT).

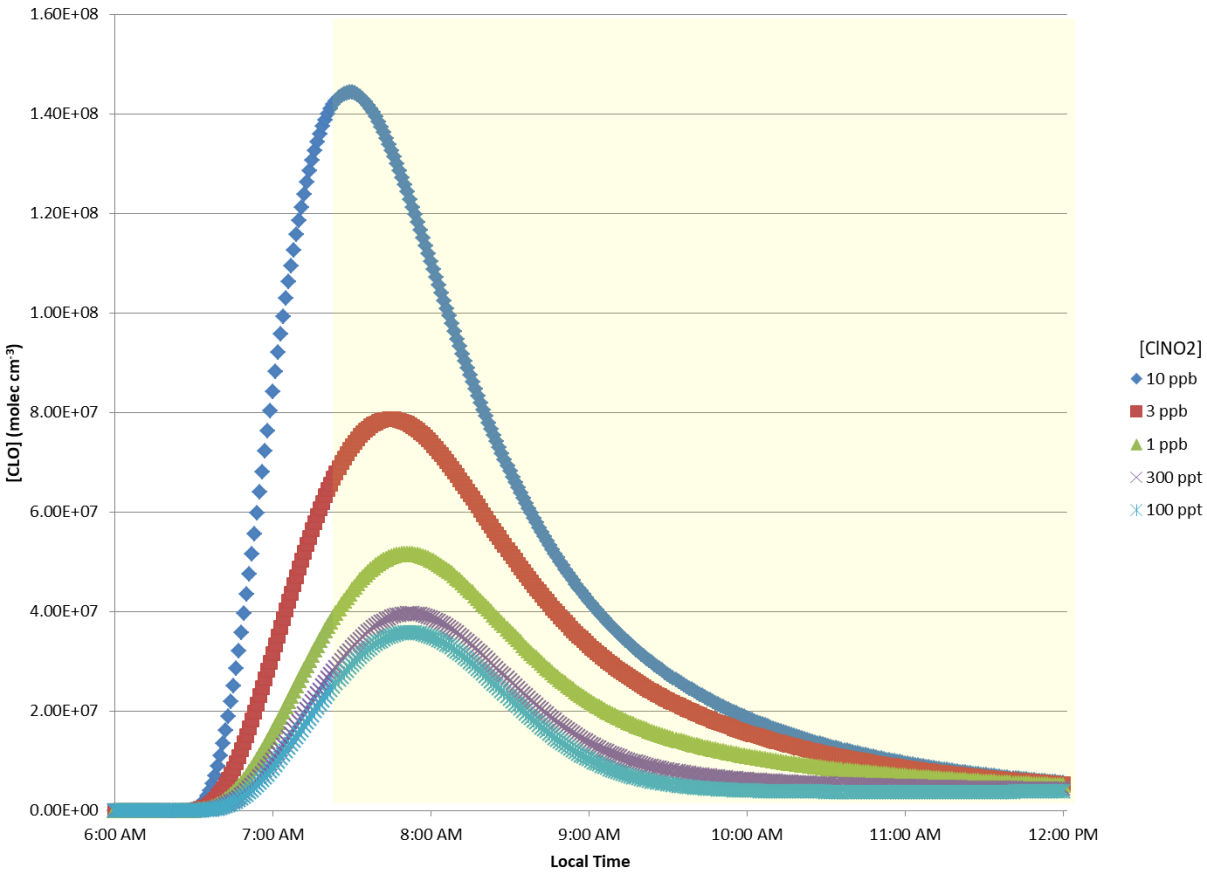

Figure 3.3: The effect of varying initial $ClNO_2$ on the modeled ClO concentration at York University on March 21 2016. $[NO_2]$ = 1 ppb. Daylight hours indicated by yellow overlay (sunrise: 7:18 AM EDT).

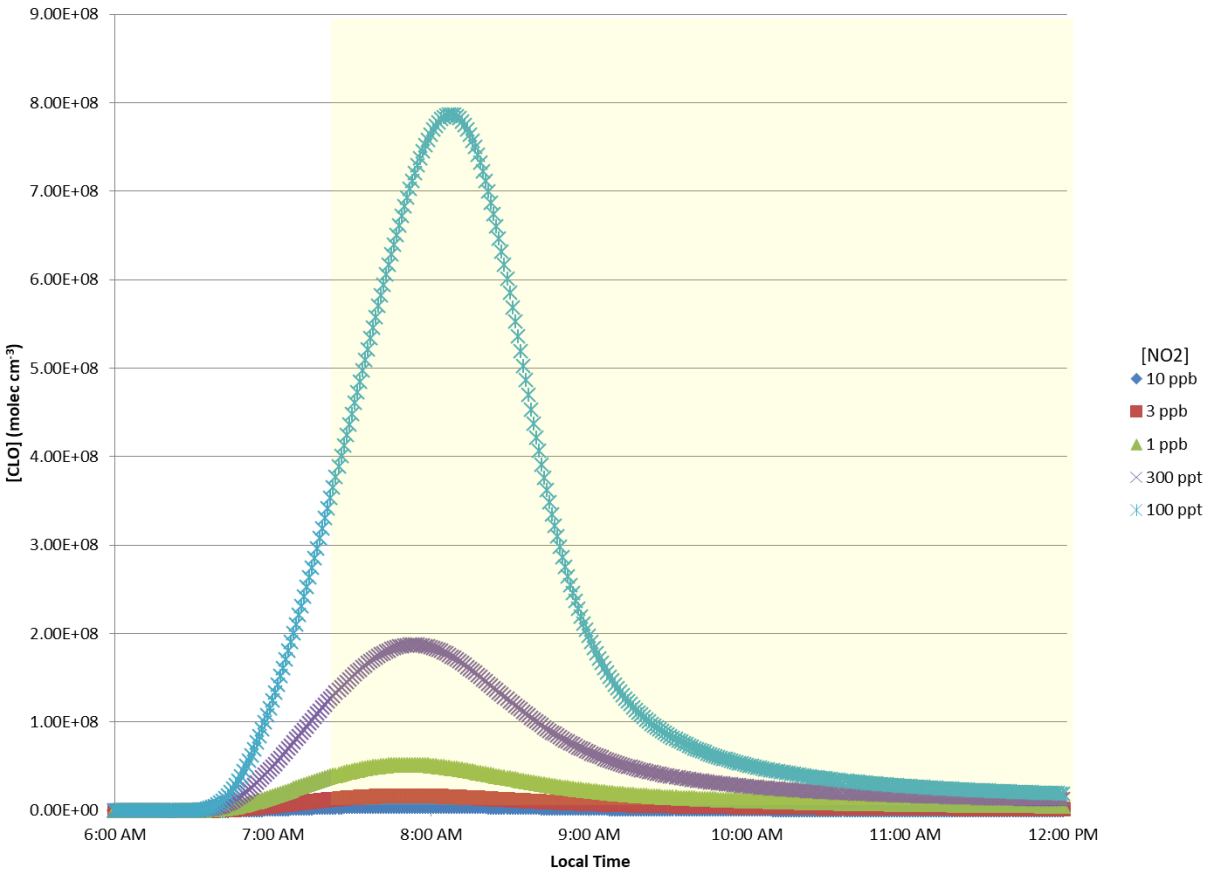

Figure 3.4: The effect of varying initial NO_2 on the modeled ClO concentration at York University on March 21 2016. [$ClNO_2$] = 1 ppb. Daylight hours indicated by yellow overlay (sunrise: 7:18 AM EDT).

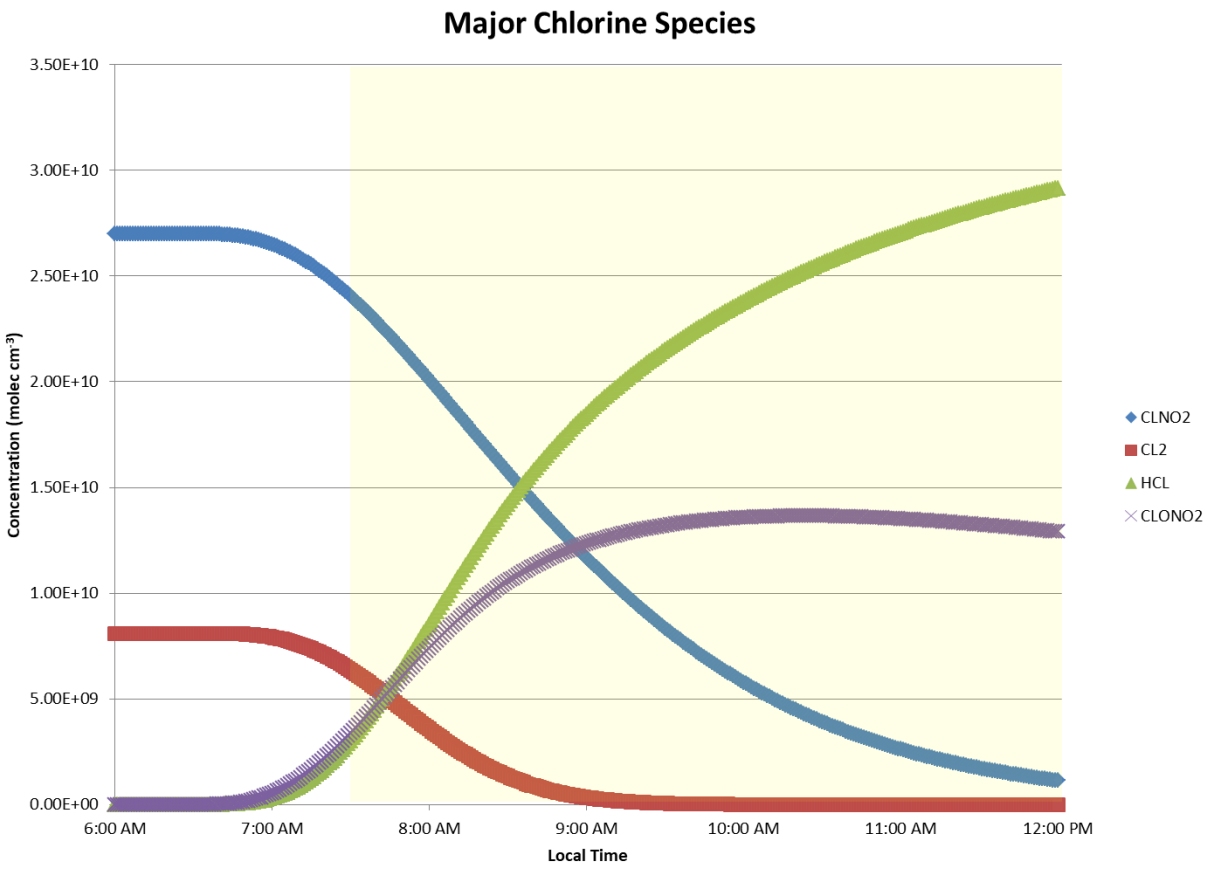

(Figure continued on next page)

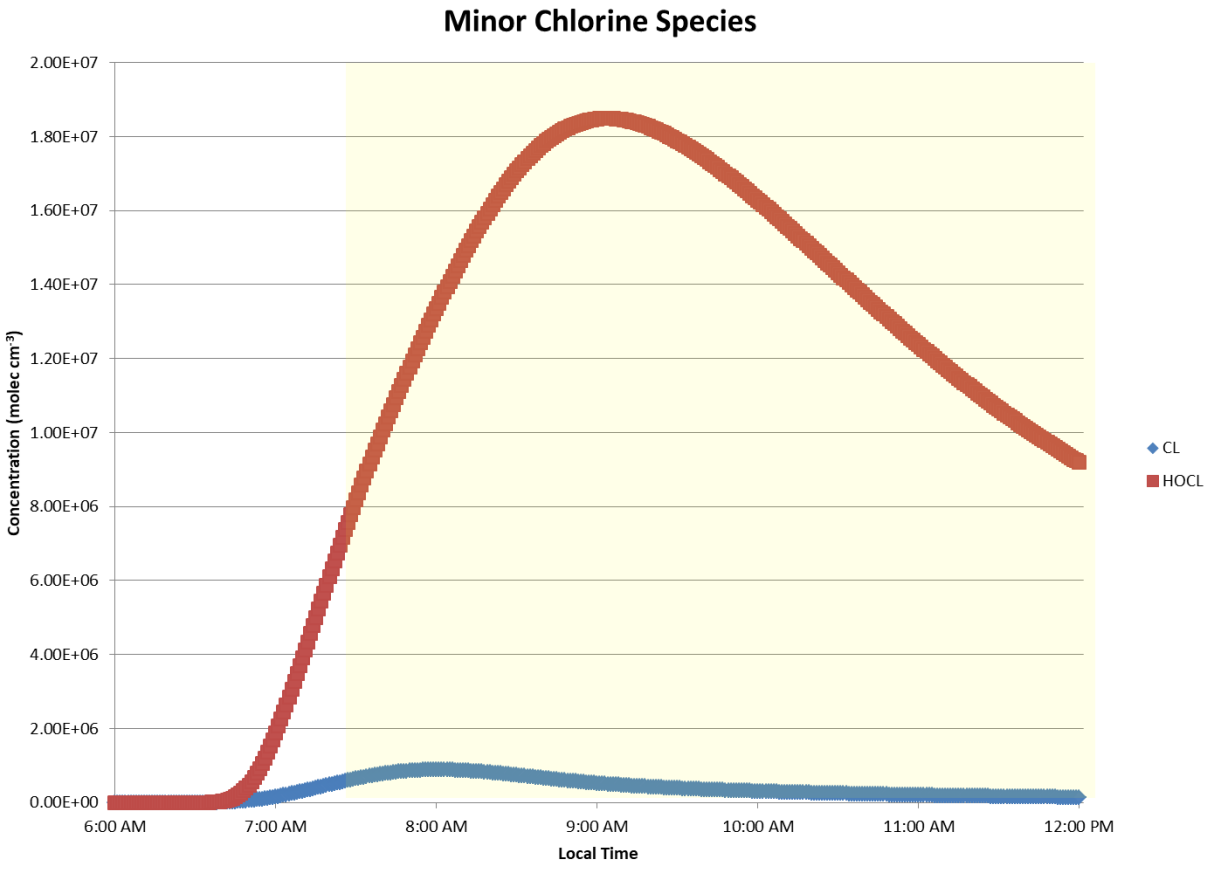

Figure 3.5: The modeled concentrations of $ClNO_2$, Cl_2, HCl, $ClONO_2$, Cl and HOCl at York University on March 21 2016. Daylight hours indicated by yellow overlay (sunrise: 7:18 AM EDT).

3.2: Experimental: Measurements at York University

3.2.1: Overview

Cumulatively, the complete usable dataset of ClO measurements consists of spectra acquired and analyzed intermittently over the course of a year, weather permitting, from March 2017 to March 2018, under both winter and summertime conditions, on both clear sky and partly cloudy days, resulting in a number of partial or full 24-hour diurnal ClO profiles. A shared focus on SO_2 was introduced during this time, with ambient SO_2 fits and sample cell experiments conducted in the second half of the study, concluding in May 2018. In making measurements, a final averaged spectrum was generated every 8.3 minutes (250 ms integration time; 2000 averages), leading to an ample amount of time-resolved spectra over the course of 24 hours, and hundreds over the course of the project. We note that in utilizing all measurement, lamp, correction and calibration spectra, the first recorded spectrum in a set (#00000) was discarded, as it is acquired with double the set collection time. **Table 3.4** displays an overview of all measurement days, organized sequentially into three major measurement periods which we denote as 'Winter/Spring 2017', 'Summer 2017' and 'Spring/Summer 2018',on the basis of the presence or absence of snow. For Winter/Spring 2017 entries, the confirmation of snow on a specific date

necessitates at a minimum, a light snowfall episode a few days prior to those measurements. A weather log detailing snow and cloud cover, temperature, wind speed, and other relevant atmospheric conditions was maintained throughout and is available upon request.

Table 3.4: The complete series of ClO measurement days, arranged chronologically into three sets: Winter/Spring 2017, Summer 2017, and Spring/Summer 2018. Background spectra were retrieved and used in fitting the measurement spectra in the corresponding data set.

Date	Type of DOAS	Type of Spectra Collection	Snow?	Date of Correction/Calibration/Lamp Spectra Used in Fitting
Winter/Spring 2017				
Monday February 20 2017	MAX	---	No	Monday February 20 2017
Saturday March 11 2017	Active	Measurement	No	Monday March 13 2017
Sunday March 12 2017	Active	Measurement	No	Monday March 13 2017
Monday March 13 2017	Active	Measurement	No	Monday March 13 2017
Thursday March 16 2017	Active	Measurement	Yes - Heavy	Thursday March 16 2017
Friday March 17 2017	MAX + Active	Measurement	Yes - Heavy	Friday March 17 2017
Tuesday March 21 2017	Active	Measurement	Yes - Light	Tuesday March 21 2017
Wednesday March 22 2017	Active	Measurement	Yes - Light	Wednesday March 22 2017
Thursday March 23 2017	Active	Background	Yes - Light	---
Wednesday March 29 2017	Active	Measurement	No	Wednesday March 29 2017
Saturday April 8 2017	Active	Measurement	Yes - Heavy	Saturday April 8 2017
Summer 2017				
Thursday August 31 2017	Active	Measurement	No	Thursday August 31 2017
Friday September 1 2017	Active	Measurement	No	Thursday August 31 2017
Saturday September 2 2017	MAX + Active	Background	No	---
Monday September 11 2017	Active	Measurement	No	Saturday September 23 2017
Friday September 22 2017	Active	Measurement	No	Saturday September 23 2017
Spring/Summer 2018				
Saturday March 3 2018	Active	Measurement	No	Sunday March 4 2018
Saturday March 17 2018	Active	Background	No	---
Monday March 19 2018	Active	Measurement	No	Wednesday March 21 2018
Tuesday March 20 2018	Active	Measurement	No	Wednesday March 21 2018
Saturday March 24 2018	Active	Measurement	No	Tuesday March 27 2018
Sunday March 25 2018	Active	Measurement	No	Tuesday March 27 2018
Monday March 26 2018	Active	Measurement	No	Tuesday March 27 2018

The fitting ranges selected for ClO and SO_2 in this study were based upon the operating range of the spectrometers, the nature of their absorption cross sections and what has conventionally been used in the literature. The SO_2 fit range we use for both active and MAX-DOAS is 303.5 – 312 nm; a range encompassing four well-defined vibronic peaks. The selection of a fit range for ClO was not as clear-cut and it is one that has varied by several nanometers in pre-existing studies, as was seen in Table 1.2. In the case of active DOAS, we initially opted for the widest possible fit range, 291-310 nm, in which there are 5 peaks. The lowest reliably detected wavelength by the spectrometer is around 291 nm, and the

absorption cross section of ClO trails off at 310 nm, as can be seen in Figure 2.2. Following data analysis however, we obtained improved fit results using a fit range of 295 – 305 nm; one that includes the middle three vibronic absorptions in the previous range. It may be that the peak at the lower end is too close to the spectrometer's lower wavelength limit and the trailing peak at the opposite end is weak in intensity. We note that the 295 – 305 nm fit range is that used in the Pohler et al. study in 2010. With respect to MAX-DOAS, this fit range was constrained further still, owing to the ~300 nm lower limit of sunlight intensity, rendering the measurement of ClO challenging using this passive technique. For this reason, we place greater emphasis on active DOAS measurements moving forward.

Prior to beginning experimental work, we were limited to speculation of what we may observe based on the few literature studies available, our preliminary modeling results and perhaps, as dictated by meteorological conditions. It was thought that on measurement days following snowfall and high winds, we may see higher values of ClO due to higher levels of Cl^- in ambient aerosols arising from salt use that would act as a source of "salt spray" in the urban atmosphere (Haskins et al., 2018; Kolesar et al., 2018). On clear sunny days, a large swift pulse of ClO is possible, whereas cloudy days may give rise to lower ClO in a wider temporal pulse due to slower photolysis rates. Overall, the detection of ClO was likely to be challenging in the case of insufficient atmospheric chloride from reduced salting over a mild late winter/early spring season. In regard to the active DOAS system, the retroreflector was positioned near ground level, rendering ClO undetectable if it is indeed primarily in the residual layer. We were unfortunately unable to obtain permission for placing the retroreflector on a tall building to allow residual layer measurements with increased $ClNO_2$ and lower NO_2. However, early morning mixing of residual layer air to the surface may homogenize the vertical gradients of N_2O5, NO_2, $ClNO_2$, Cl, ClO, and O_3. We therefore continue to be optimistic as we present experimental results in the following sections.

3.2.2: Active DOAS ClO Measurements

Measurements of our original target molecule, ClO, using the active DOAS instrument, comprise the bulk of our results and discussion. Here we compile and present the total of our results, offer some potential insight into our observations and critically evaluate any unforeseen issues we've encountered, primarily based on quality markers of the DOASIS fits. We shape our discussion according to the divisions in Table 3.4 in order to present our results chronologically and discuss the flow of our understanding as it led to further experimental tests and modifications. This is achieved using a case-study approach, as we present DOASIS fits of individual and groups of measured spectra that are representative of overall trends and consider possible root causes. Following a shift in focus to SO_2, another UV absorber in the same spectral region, we finish with a look at the limitations of MAX-DOAS for ClO measurement, as well as a modeling vs. experimental comparison, before speaking to study-wide observations and conclusions at the end of the section.

Winter/Spring 2017

We begin with the first round of measurements in the winter of 2017. These measurements were made from February 20 2017 to April 8 2017 inclusive, cumulating in 9 days of active DOAS data, along with 2 days of MAX-DOAS data, with one day of overlap (March 17 2017). The idea was to take

measurements on mornings after snowfall, when salt application on the roads could have given rise to increased levels of Cl^- aerosols and thus potentially, overnight accumulation of N_2O_5, $ClNO_2$ and/or Cl_2. A series of atmospheric raw spectra were collected from pre-dawn, continuing through sunrise, into the early afternoon. This was followed by the collection of daily electronic offset, dark current and calibration (Hg lamp) spectra. This led to morning profiles extending from 6 AM to ~ noon or 1 PM, on several dates in the Winter/Spring 2017 phase. We originally elected to forego the measurement of lamp spectra, and rather, we were to use a ~ 5 AM measured spectrum, under the assumption that a spectrum taken prior to sunrise, and prior to ClO formation, may serve the same purpose, however, this was replaced with standard lamp spectra in later measurements. We present original fitting results on days with the highest snowfall amounts, March 16 2017, March 17 2017 and April 8 2017, in **Figure 3.6**, with the remaining days displayed in **Figure 3.7**. We repeatedly observe unusually high mixing ratios, well above the maximum 5-15 ppt of tropospheric ClO reported in the literature (Stutz et al., 2002). On first glance, there seems to be no correlation to snowfall amounts, with high and low mixing ratios in both plots. In looking at the diurnal pattern on certain dates, we observe a sharp increase in ClO in the mid-morning hours, sometime after sunrise, which seems to persist into the afternoon, with no sharp decline in ClO as anticipated by earlier modeling.

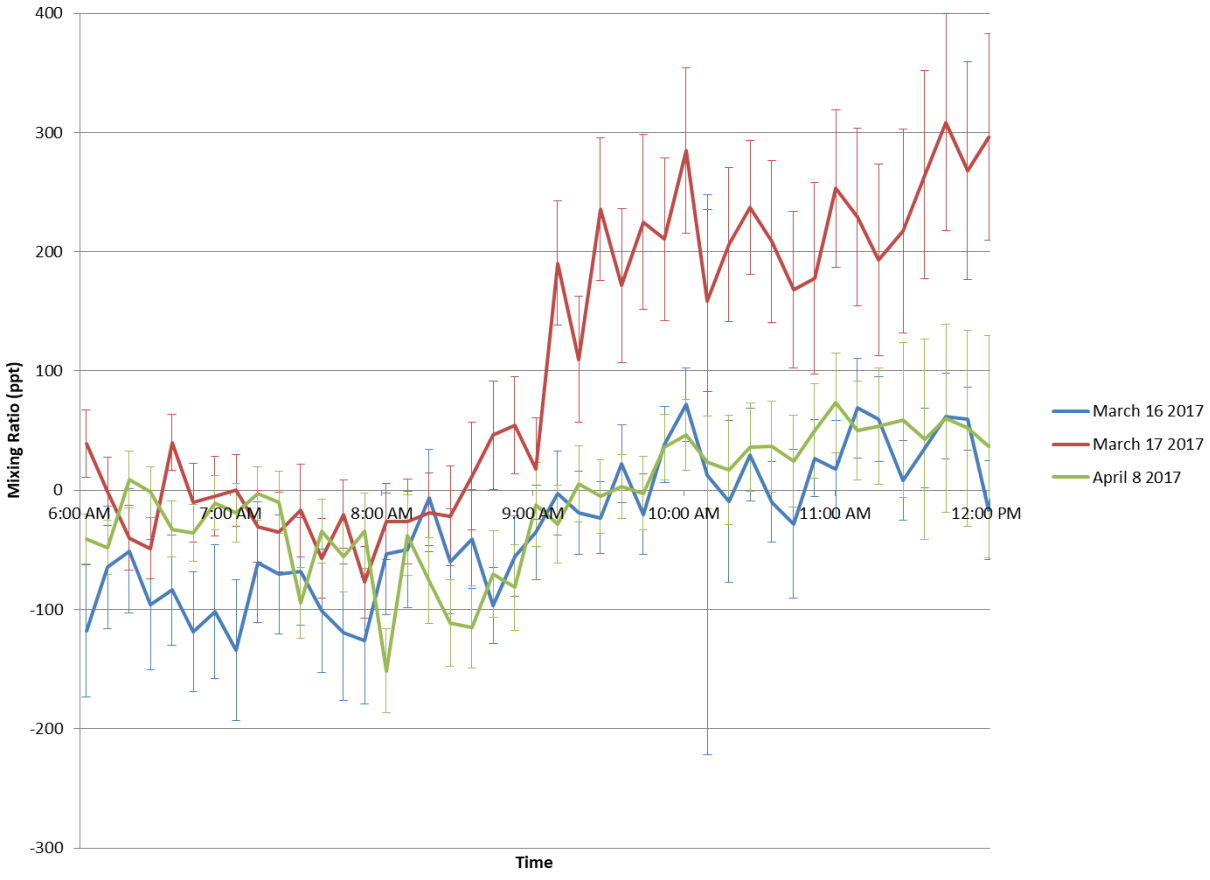

Figure 3.6: ClO mixing ratios on days following high snowfall in the Winter/Spring 2017 measurement period. Sunrise times range from 6:47 to 7:28 AM EDT.

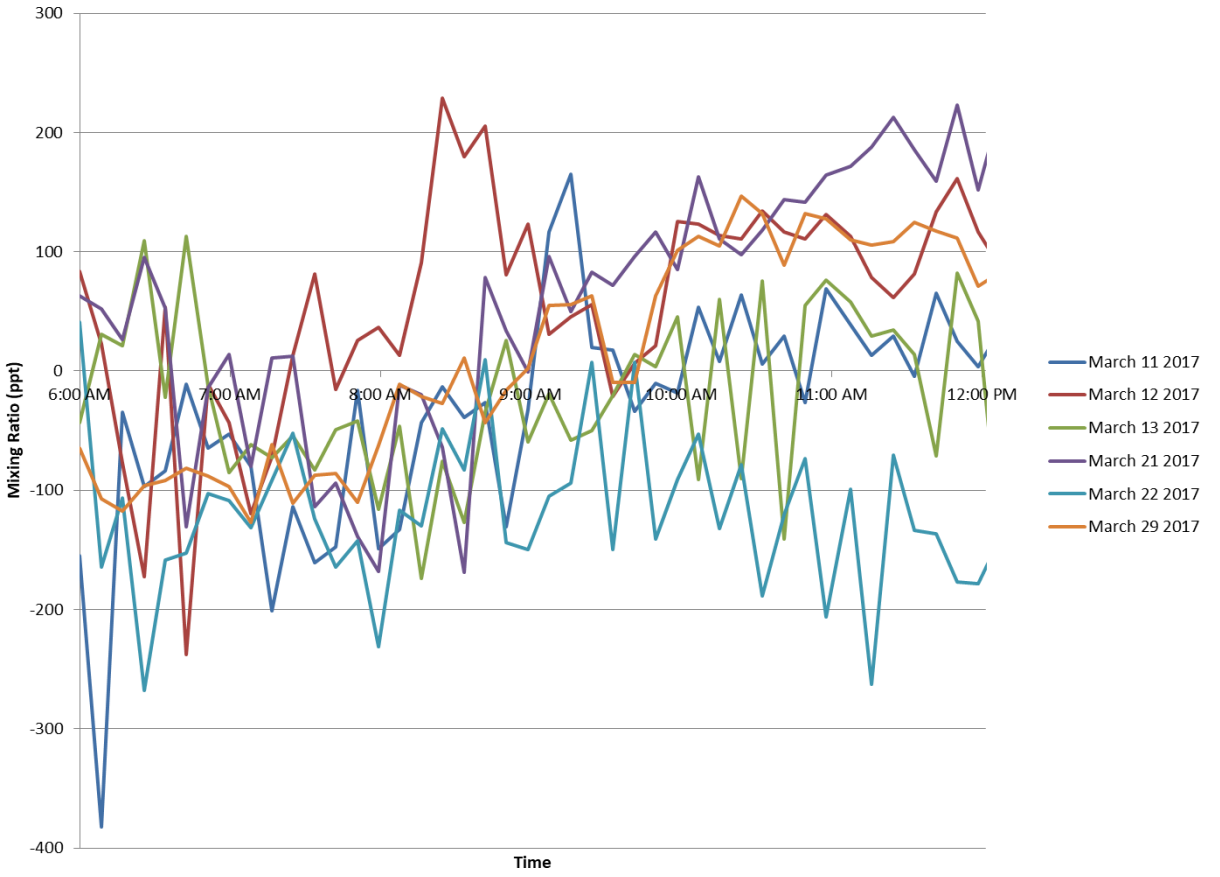

Figure 3.7: ClO mixing ratios on all remaining days in the Winter/Spring 2017 measurement period. Sunrise times range from 6:37 to 7:04 AM EDT. Error bars omitted to minimize visual clutter.

We next choose to narrow in on the March 17 2017 time series; the day which saw the highest ClO mixing ratios during the span of this measurement period and the only day with clear skies. A series of background spectra were recorded, initially as a precautionary measure, on March 23 2017, a similarly clear and sunny day, close in time proximity to our measurement set. Upon observing the unusually high mixing ratios, we attempted to include these background spectra in the fit, to remove any possible interfering sunlight that may be entering the telescope from the field of view. **Figure 3.8** presents the final ClO fit results for March 17 2017, one that includes background subtraction and a few key amendments to be described shortly. We see the mixing ratios decrease significantly but nevertheless remain high, and the diurnal pattern seems to persist. At this point, we note that our data is clearly noisy and we must consider the possibility that our detection limits are not low enough; a topic which we discuss at length in subsequent sections. However, given that detection limits may be improved with changes to the instrumental system or with post-processing averaging, we choose to continue with measurements to investigate these large signals and diurnal patterns.

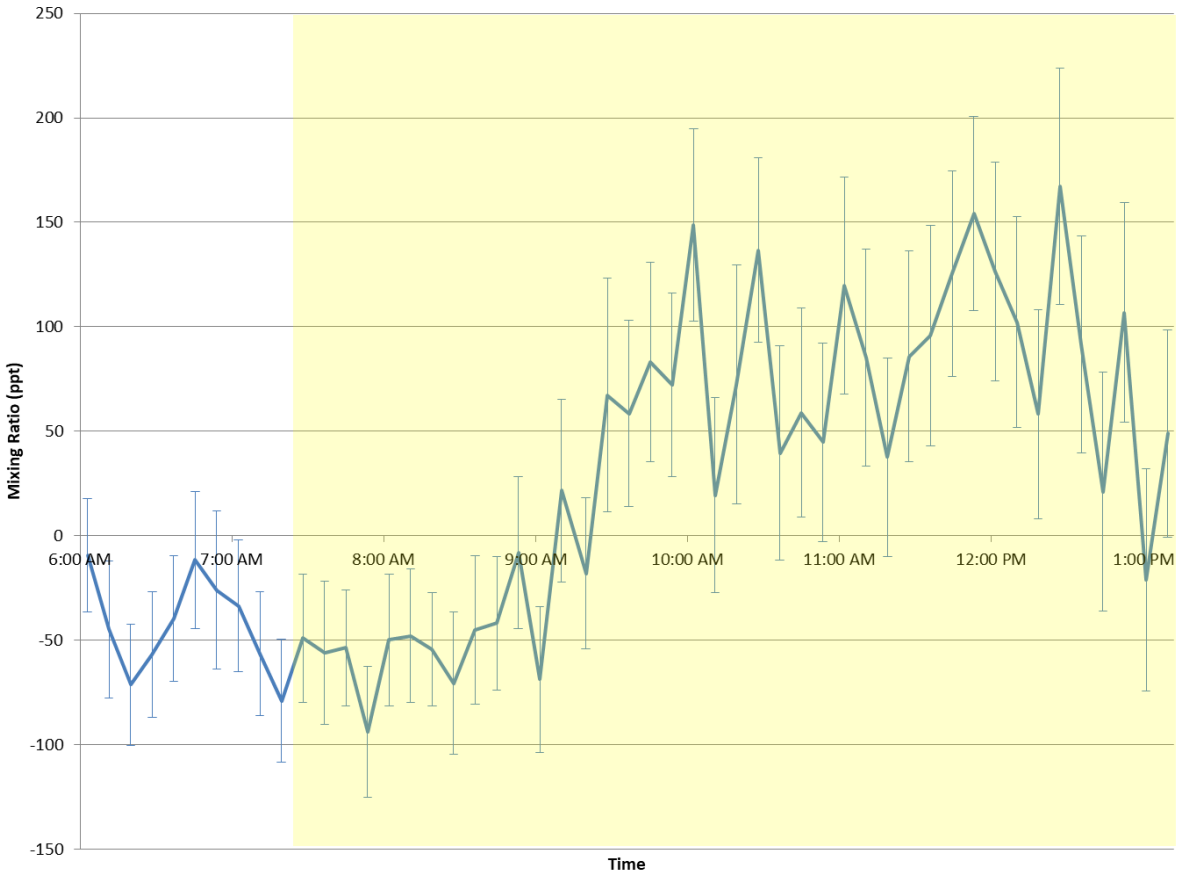

Figure 3.8: ClO mixing ratios on the morning of March 17 2017. Background spectra used in the fit were collected on March 23 2017. Daylight hours indicated by yellow overlay (sunrise: 7:26 AM EDT).

Summer 2017

Our initial observations led us to obtain a second set of measurements in the summer for comparison with wintertime results. In **Figure 3.9**, we present a continuous 24-hour time series of ClO mixing ratios on August 31st 2017 through to September 1st 2017. The instrument was run for a full day without interruption, with correction spectra taken the day prior, rather than the day of. This provides us with a better look at the diurnal pattern, as we now see that we must shift our focus beyond the morning hours. In addition, we restricted measurements to clear days only, to support the application of background spectra. As in the winter, we observe a sharp crossover sometime after sunrise, and we now see that ClO seems to remain prominent until just after sunset, at which time it experiences a sharp decline. There is a small grouping of positive mixing ratios during the early-morning pre-sunrise hours, although these values are largely zero within error. Most notably, we again observe unusually high mixing ratios, albeit to a lesser degree, and larger negative mixing ratios at night. At first glance, these results may lead us to propose two findings; that a seasonal dependency is uncertain at this point and that there exists a link between the presence of ClO and sunlight levels. The full set of Summer 2017 measurements, on a 24-hour scale, is shown in **Figure 3.10**.

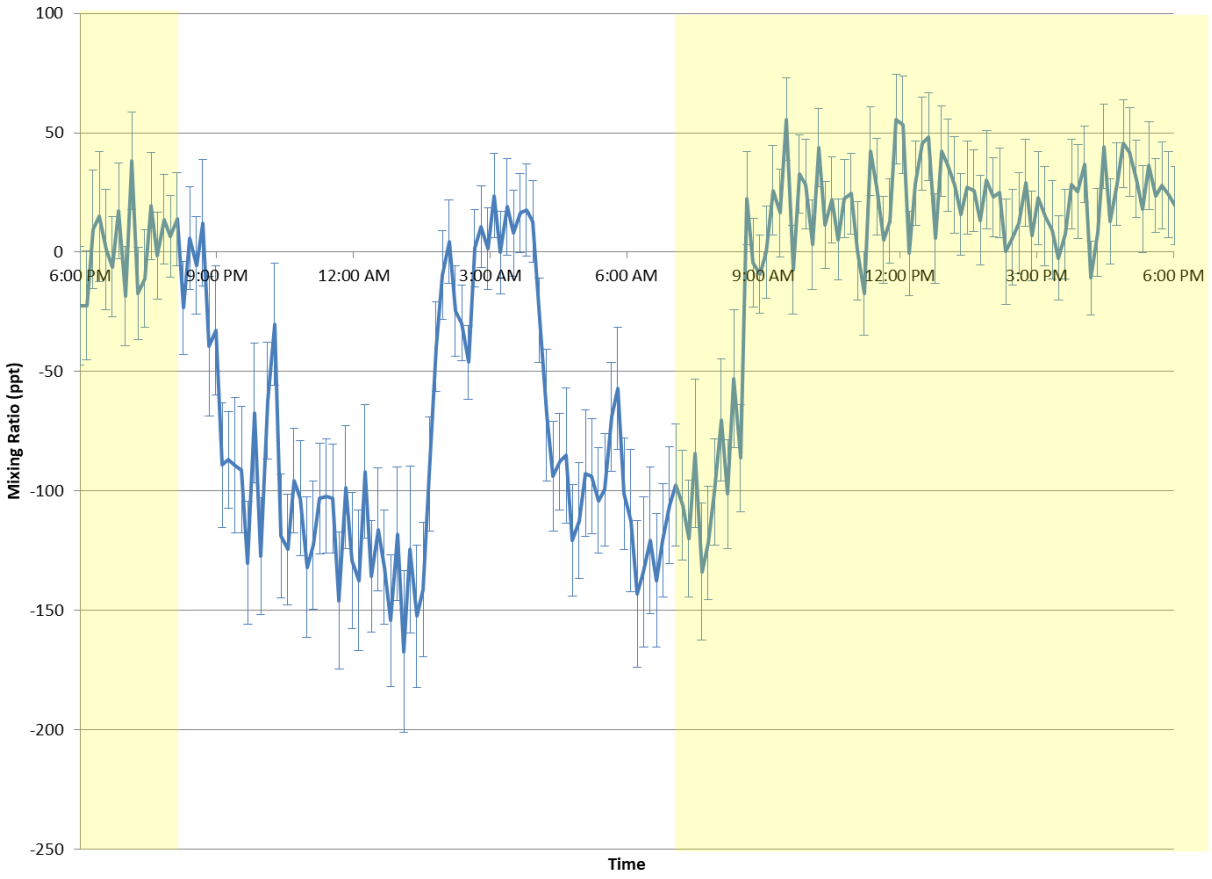

Figure 3.9: ClO mixing ratios over a 24-hour period from 6 PM on August 31 to 6 PM on September 1 2017. Background spectra used in the fit were collected from 6 PM on September 1 to 6 PM on September 2 2017. Daylight hours indicated by yellow overlay (sunset: 7:53 PM; sunrise: 6:42 AM).

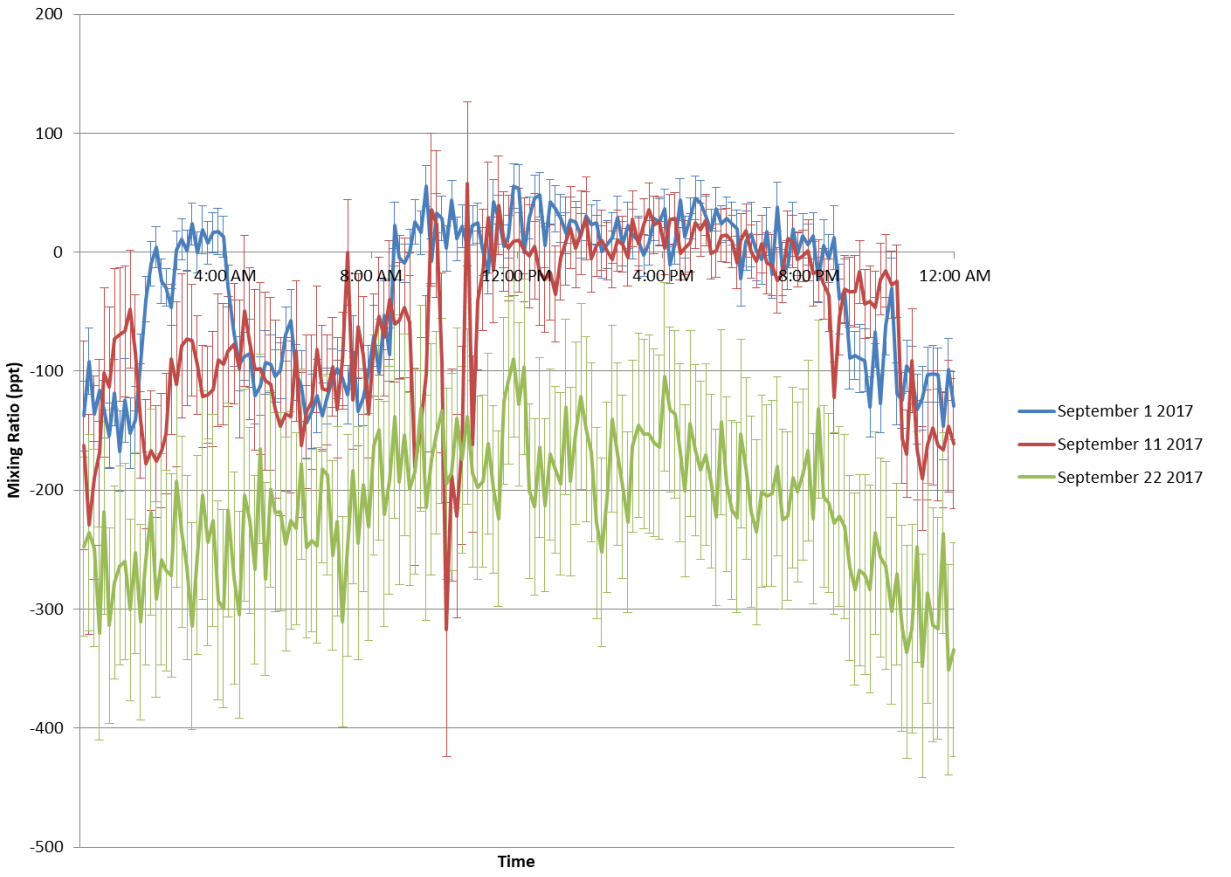

Figure 3.10: ClO mixing ratios during the Summer 2017 measurement period. Sunrise times range from 6:42 to 7:06 AM EDT.

To investigate the highly negative mixing ratios, high noise and correlation to sunlight intensity, we took a systematic approach in examining and ensuring the consistency of variables in both the pre-processing steps (i.e. by retaking correction and calibration spectra) and in regards to the DOAS fitting procedure. **Figure 3.11** illustrates the visual appearance of the original ClO fit for the highest mixing ratio on March 17 2017. It appears to be fairly convincing with respect to the presence of spectral features. In contrast, a depiction of a fit for a large negative mixing ratio is seen in **Figure 3.12**. Nevertheless, we must consider the possibility that the mixing ratios we have obtained may not be real (the negative mixing ratios are surely not real), by reason of their magnitude and as evidenced by certain red flags during fitting. We introduce and attempt to correct these issues, deviating from the standard fitting procedure in three key ways, outlined and explained below. The March 17 2017 fit generated using these amendments is shown in **Figure 3.13** and although it still results in a high mixing ratio, the fit is visually not as convincing and not conclusive.

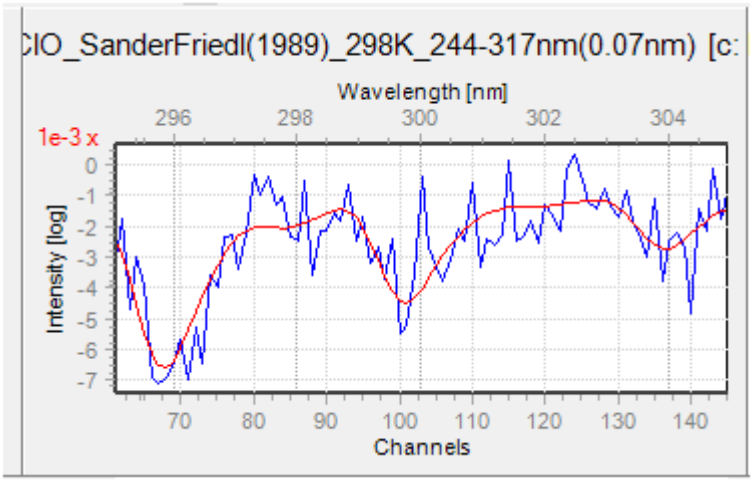

Figure 3.11: An example ClO fit on March 17 at 10:02 AM corresponding to a fit coefficient of 2.92E+15 +/- 3.25E+14 molec cm^{-2} or a mixing ratio of 274 +/- 30 ppt.

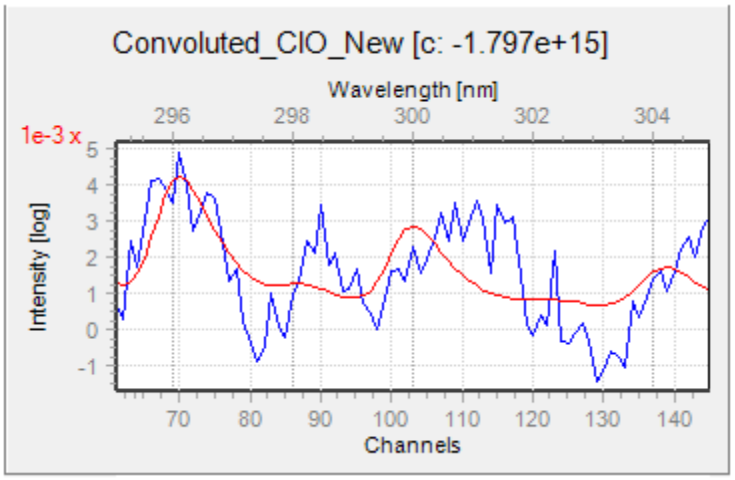

Figure 3.12: An example ClO fit on September 1 at 7:53 AM corresponding to a fit coefficient of -1.80E+15 +/- 3.63E+14 molec cm^{-2} or a mixing ratio of -94 +/- 31 ppt.

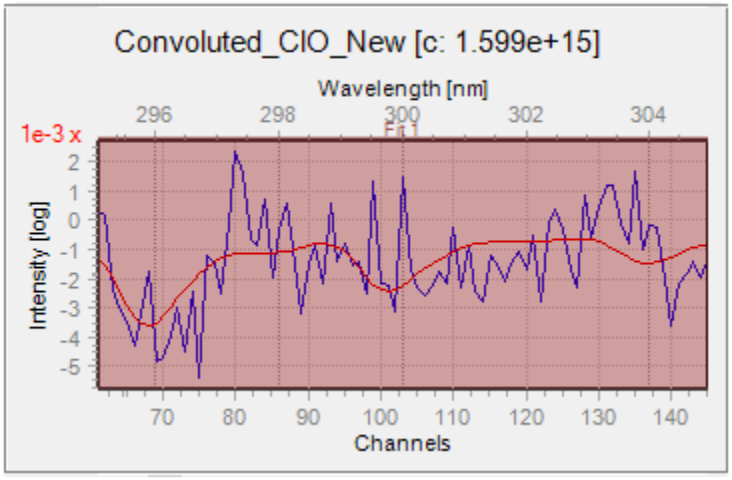

Figure 3.13: An example ClO fit on March 17 at 10:02 AM corresponding to a fit coefficient of 1.60E+15 +/- 4.95E+14 molec cm^{-2} or a mixing ratio of 149 +/- 46 ppt.

- **i.** Use of an average of multiple measured spectra at ~ 5 AM to serve as lamp spectra (for Winter/Spring 2017 only)
- **ii.** Modified correction of dark current integration time
- **iii.** Subtraction of background spectra collected with the lamp off

i. As mentioned previously, no lamp spectra were collected during winter measurements. In fitting this data, rather than using a single measured spectrum at 5 AM as the lamp spectrum, as originally intended, we used instead an average of multiple spectra to reduce the noise. Although we simply require a reference spectrum in which ClO is not present, variable fit coefficients were obtained when using lamp spectra at slightly different times. Therefore, an average spectrum was generated by subtracting offset and dark current from four spectra before and after 5 AM and subsequently adding them. In taking summer measurements, we chose to log conventional lamp spectra to eliminate the need for this step.

ii. During fitting we noticed that when zoomed in on an offset and dark current-subtracted spectrum, too much dark current signal was removed, as evidenced by the formation of negative dips in intensity, illustrated in **Figure 3.14**. This issue was all the more apparent when looking at the fit residuals, in which a hot pixel preceding the 296 nm mark was visible in many instances, as exemplified in **Figure 3.15** and **Figure 3.16**. To correct for this over-subtraction, the spectrum was divided by an arbitrary constant, equivalent to correcting for differences in integration time between spectra, until these troughs across the spectrum were removed. This will undoubtedly introduce error into the results, if we are in fact removing too much or too little dark current, particularly from low-intensity spectra such as the background spectra. Ideally, we would want to collect a representative dark current spectrum from the beginning to eliminate this step as well. Considering the root causes of too much dark current seems to suggest that either excess light was entering into the spectrometer or the temperature was fluctuating during collection. With our temperature controller, we regularly logged fluctuations up to 1 degree and

occasional drifts up to 2 degrees from the set temperature. If possible, placing the spectrometer in a dark temperature controlled chamber steady to a few tenths of a degree may resolve the issue.

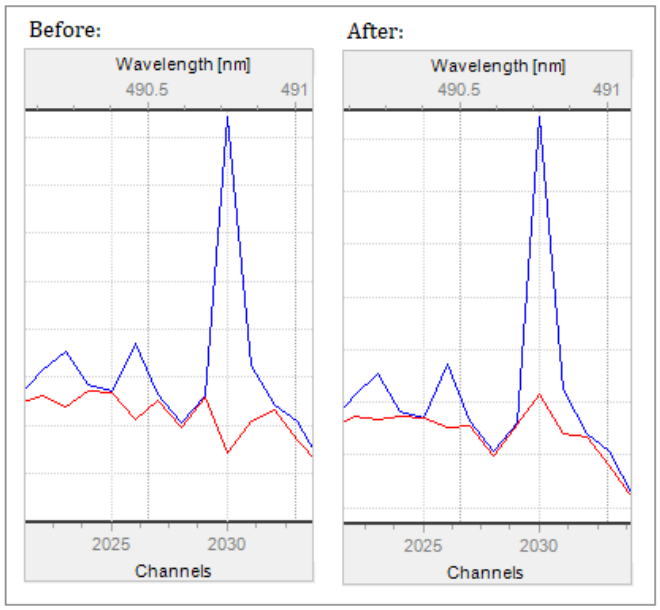

Figure 3.14: An example measured spectrum with dark current removed (red) vs. without dark current removed (blue), before and after modification of the dark current intensity.

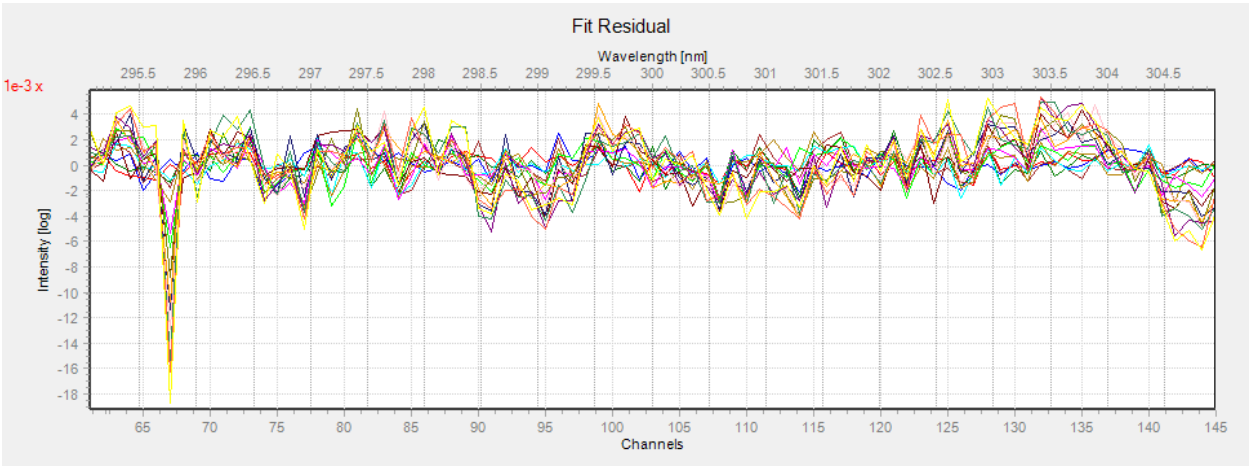

Figure 3.15: Fit residuals on March 17, prior to correcting for over-subtraction of dark current signal. Each trace corresponds to a single spectral fit.

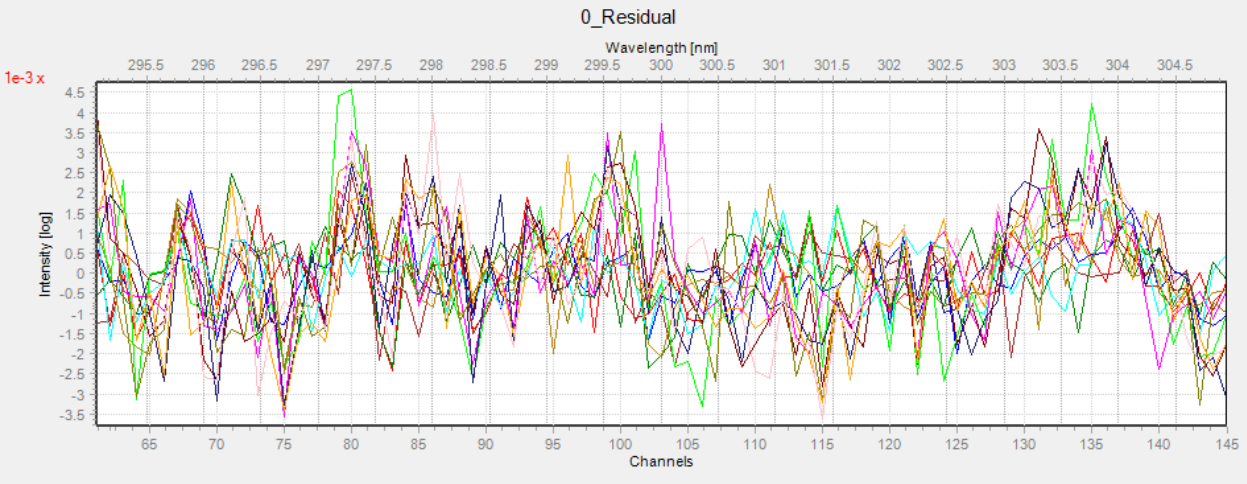

Figure 3.16: Fit residuals on March 17, after correcting for over-subtraction of dark current signal. Each trace corresponds to a single spectral fit. Traces of the hot pixel just ahead of 296 nm have been removed.

iii. Background spectra (lamp turned off) collected over 24 hours on a clear day show the development of a weak scattered sunlight spectrum, evidenced primarily by the growth of the most prominent Fraunhofer features just ahead of the filter cut-off point at 400 nm, namely the Ca^{+} lines at ~393 nm and ~397 nm. During daylight hours, these background spectra resemble a scattered sunlight MAX-DOAS spectrum, as shown in **Figure 3.17**, with the highest intensities occurring around noon. This suggests that stray sunlight is entering the telescope and the possibility arises that we may inadvertently be measuring absorption signals due to the presence of ClO in the stratosphere. To lend support to this hypothesis, the background spectra themselves were fit for ClO. However, the results were inconclusive, with poor fits yielding no clear trend, rather a smattering of both positive and negative values with virtually all error bars crossing the x-axis, such that zero, small non-zero and large non-zero values are all possible at any time.

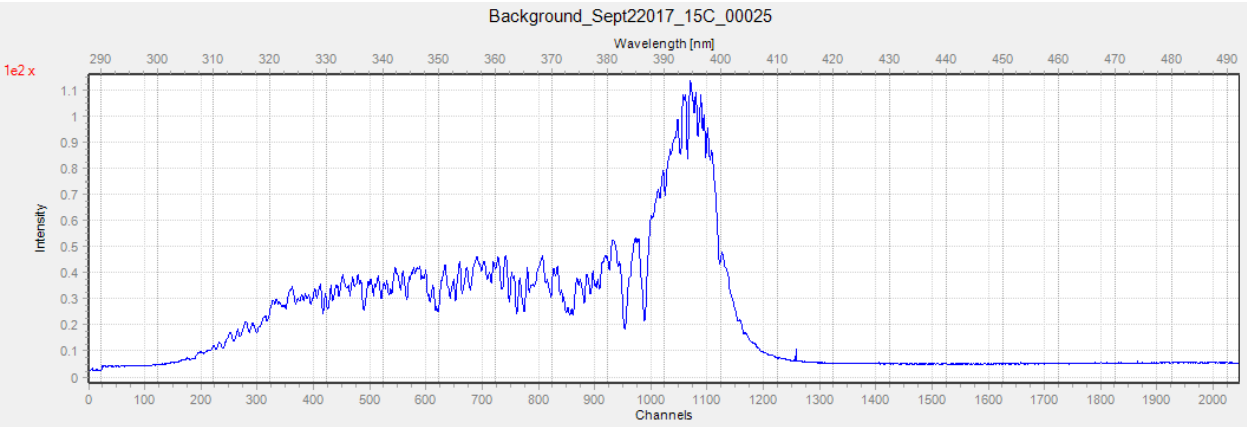

Figure 3.17: An example background spectrum collected on September 2 2017 from 12:10-12:35 PM.

To attempt to remove this background component, the spectra were incorporated into the fit in one of two ways; by subtracting the respective background spectra from the lamp and measured

spectrum prior to fitting, or by adding them as reference spectra. Both methods produce the same fit coefficients within error, decreasing the values of ClO slightly, however they remain unusually high, suggesting it may not be stratospheric ClO, or may only partially be. As well, the noise remains excessively high following this background subtraction. In the literature, the diurnal and seasonal variation of stratospheric ClO at mid-latitudes has historically been difficult to discern (Kuwahara et al., 2012), however the approximate diurnal patterns seen generally agree well with that of ClO in the mid-stratosphere at 30-40 km; seen in **Figure 3.18**. This may imply that there is an error in incorporating the background component, although our approach is reasonable, if at any given time of the day, we assume a negligible change in stratospheric ClO between the days the measurement and background spectra were collected. Temporal trends of stratospheric ClO (Ricaud et al., 2000) have shown only a slight seasonal variation, decreasing with altitude, and thus we presume little variation over the course of a few days. However, enhanced ClO is typically observed in the stratosphere during spring ozone depletion events that are observed in the southern hemisphere in September-November (Solomon at al., 2016) and occasionally, but to a lesser extent in the northern hemisphere during our measurement periods in March (Manney and Lawrence, 2016).

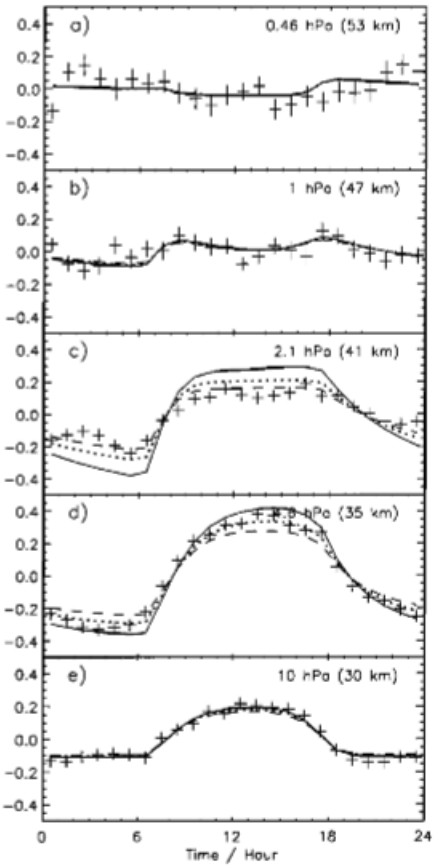

Figure 1. The ClO diurnal variation at (a) 0.46 (~53 km), (b) 1 (~47 km), (c) 2.1 (~41 km), (d) 4.6 (~35 km), and (e) 10 hPa (~30 km) as measured by UARS/Microwave Limb Sounder (MLS) from 1991 to 1997 within the band 40°-50°N and averaged irrespective of the year within 24 1 hour wide (crosses) bins and as calculated by a 0-D purely photochemical model with $\eta = 0$ (solid line), 0.05 (dotted line), and 0.1 (dashed line) at 45°N in February. Vertical bars represent a 1σ error.

Figure 3.18: The diurnal variation of ClO in the middle stratosphere. Adapted from "Temporal evolution of chlorine monoxide in the middle stratosphere," by P. Ricaud et al., 2000, J. Geophys. Res., 105, p. 4459–4469.

It is important to take into consideration that cloud cover on measurement days may have varied widely. The ideal long term solution would be to automatically take consecutive spectra with the lamp turned on and off, to obtain accurate background spectra for that date and time. This is not possible with our instrument without significant modification, nor is repeating this process manually, as after the lamp is turned on, a ~2-hour warming period is required and we would lose a substantial amount of measuring time (25 minute background spectrum + 2 hour warm-up). As a compromise, a single background spectrum taken at noon on the day of measurements may represent a maximum on a sunny day, but is not applicable if cloud cover is changing throughout the day. For this reason, subtraction of background spectra cannot reliably be applied on a partly cloudy day, and thus the above winter and summer measurement and background days were chosen to be showcased for the reason that they were primarily clear days. Alternatively, we can prospectively apply this technique on a uniformly overcast day.

We originally hypothesized a higher likelihood of ClO detection on March 16, March 17, and April 8 2017 on the basis of snowfall amounts and high wind speeds. However, of these three measurement days, March 17 was the only clear day (with accompanying MAX-DOAS data). With the above recent developments in the fitting procedure, of the remaining 6 days that saw no immediately preceding snowfall, March 21 and March 22 were mostly clear and so were re-fit. Once again, if we assume stratospheric ClO is largely unchanging from one day to the next, and if we had a similar amount of cloud cover (minimal to none), this would suggest that deviations in mixing ratios or the diurnal pattern arise from a difference in tropospheric conditions between measurement days, such as more or less atmospheric chlorine or NO_2, which will affect ClO sources and sinks. This may be the case in **Figure 3.19**, the time series on March 21, in which we observe a comparable diurnal pattern to March 17 but lower mixing ratios. On the other hand, March 22 seems to be an outlier as it exhibits similar peak mixing ratios but no diurnal pattern, as seen in **Figure 3.20**. Every data point on this plot is zero within error, however once again, noise is unusually high. Quantitatively, we calculate an apparent $6\sigma \approx 180$ ppt, $3\sigma \approx 90$ ppt and $\sigma \approx 30$ ppt. Cumulatively, we hold evidence both in support of, and in contradiction to, the presence of tropospheric and stratospheric ClO, and we must continue to review our results with a critical eye.

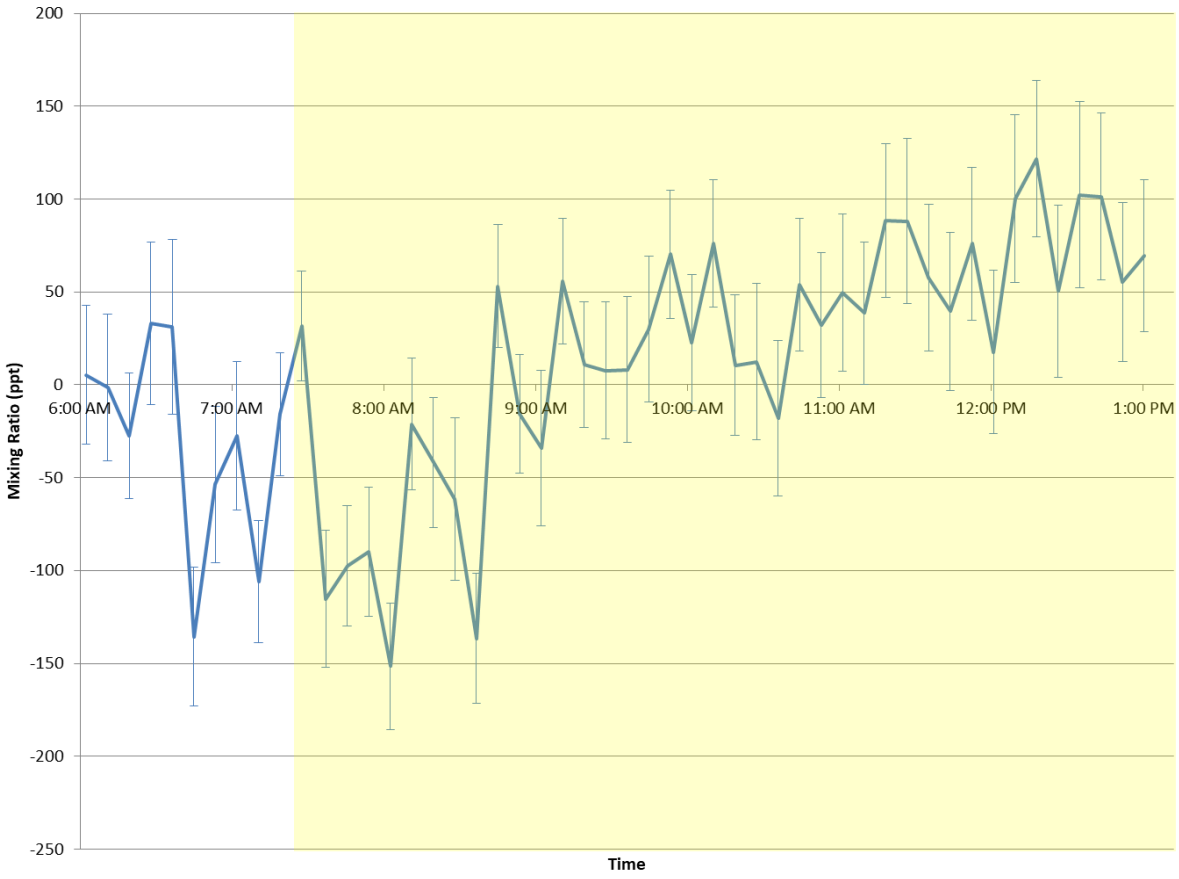

Figure 3.19: ClO mixing ratios on the morning of March 21 2017. Background spectra used in the fit were collected on March 23 2017. Daylight hours indicated by yellow overlay (sunrise: 7:18 AM EDT).

Figure 3.20: ClO mixing ratios on the morning of March 22 2017. Background spectra used in the fit were collected on March 23 2017. Daylight hours indicated by yellow overlay (sunrise: 7:17 AM EDT).

Spring/Summer 2018

Ideally, the intention was to take a final set of measurements the following winter. We were unsuccessful in this endeavour due to unfavourable weather conditions further restricted by recent developments – a need for snowy yet completely clear days with a second clear day for background measurements. We sporadically would obtain a day (or partial day) of measurements or a day of background spectra but not in close enough time proximity to one another. Prolonged clear days became more frequent as the end of winter neared and we began taking more measurements in March 2018, comprising our final wave of data, but due to the lack of snow by this time, we classify these as summertime measurements.

Figure 3.21 displays this closing set of ClO mixing ratios, spanning 24 hours on six measurement days. These results are not unlike what we have seen before; a diurnal pattern consisting of a midday peak, increasing near sunrise and decreasing near sunset. Unfortunately we again produce both unusually high ClO mixing ratios, negative mixing ratios and very high noise levels. This suggests that over-subtraction of a dark current signal and interference of sunlight remains an issue. At this point, we consider the possibility that the detection limit of our current system is not low enough to measure

ambient ClO, and we investigate this likelihood through turning our attention to our secondary molecule, SO_2.

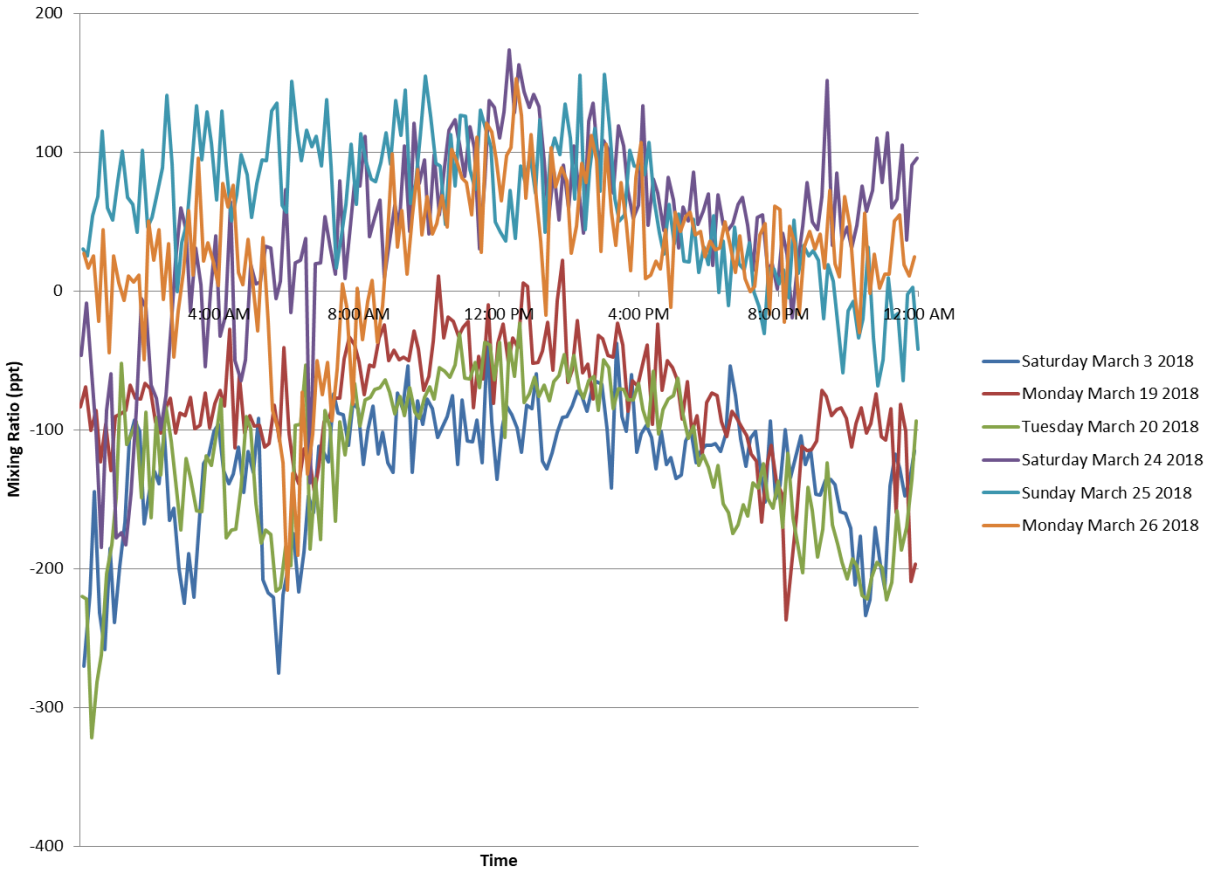

Figure 3.21: ClO mixing ratios on dates in the Spring/Summer 2018 grouping. Error bars omitted to minimize visual clutter. Note: Results were obtained using a standard fitting procedure, prior to background subtraction and any DC integration-time correction that may be required.

3.2.3: Active DOAS SO_2 Measurements

To expand the utility of our ClO dataset, we fit some of the data for ambient SO_2, in order to compare it to hourly SO_2 measurements from a nearby air quality monitoring station; the OMECC Toronto North station located at 4905 Dufferin St. in Toronto. This external data provided us with a basis for comparison not possible with ClO. According to these OMECC measurements, the area typically sees very little SO_2, up to a maximum of a few ppb on occasion. Looking at our final dataset, 0 +/- 1 ppb of SO_2 was reported over the full 24-hour periods, with the exception of Monday March 26 2018, when it went up to 1 +/- 1 ppb from 10 AM to noon EDT. We chose to fit that day for SO_2 and obtained the result in **Figure 3.22**. We see a baseline of non-zero SO_2, under 1 ppb, and a peak that may correspond to this increase or may be the sunrise/sunset phenomenon seen with ClO. To confirm, we fit two reportedly zero SO_2 days, Saturday March 3 2018 and Sunday March 25 2018 and observe that although the March 3rd data falls in line with what we would expect, March 25th follows the same pattern as the 26th. Either

these SO_2 mixing ratios are accurate and there is a location-based discrepancy, or more likely, the SO_2 fits are also compromised by fitting issues. It may stem from the interference of background sunlight, but then the question arises as to why the effect is more pronounced on certain days, when each day saw clear skies, assuming similar sunlight levels. There must be more to it, and we indeed saw dark current error in the form of a dip at the pixel preceding 296 nm in the ClO fits on March 25th and March 26th. Consequently, we know that DC over-subtraction affects SO_2 fitting as well, even though this feature is not in the SO_2 fit range and so the problem is not as visible. But again, because we were consistent with the collection and processing of the correction spectra, why is DC an issue on some days and not others? It is likely some combination of both DC, sunlight, and possibly other factors. Since ClO is anticipated in even smaller mixing ratios than ambient SO_2, these problems are only all the more amplified and the real diurnal patterns and mixing ratios of ambient ClO and SO_2 may be masked due to these issues.

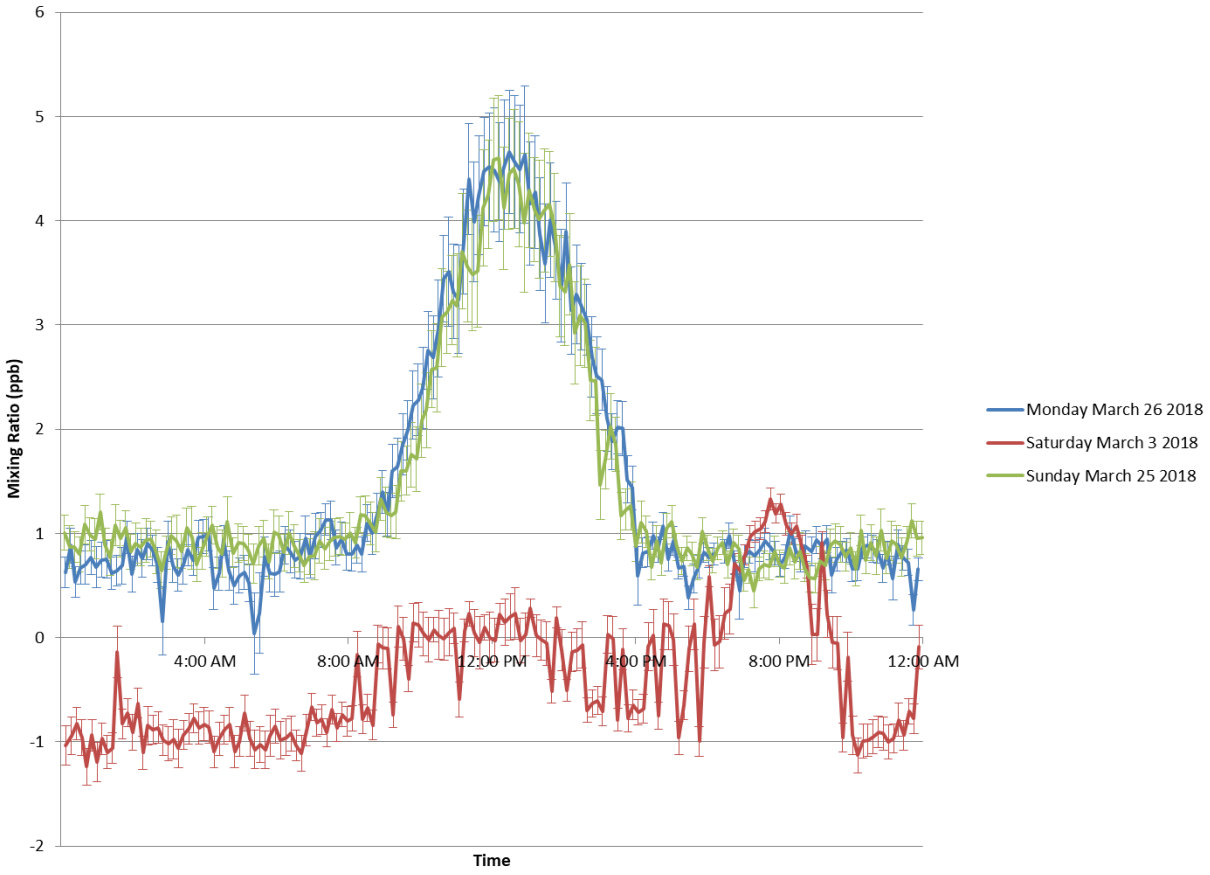

Figure 3.22: SO_2 mixing ratios on select dates in the Spring/Summer 2018 grouping. Note: Results were obtained using a standard fitting procedure, prior to background subtraction and any DC integration-time correction that may be required.

Detection Limits

As mentioned, it is also possible that ClO levels are too low for our detection limits. In order to estimate the detection limits for our active DOAS system, we first present a standard limit of detection calculation within a 99.7% confidence interval using the following equation:

$$DL = 3\sigma_{blank}$$

We select a spectrum in which ClO is assumed to be equal to zero and we make the assumption that the noise is solely instrumental noise rather than ambient atmospheric noise. In this way, our calculations represent a maximum detection limit, which in actuality may be lower if some of the noise is of the latter origin. Using the relatively flat series of early morning data points in Figure 3.6, we calculate 3σ ≈ 90 ppt. This seems to suggest our data on March 17 2017 is statistically significant, exceeding 2σ (maximum mixing ratio of 310 ppt > 180 ppt). Using Figure 3.20, in which all data points are zero within error, we calculate 3σ ≈ 150 ppt. Together, we estimate the detection limits for ClO to span around 90–150 ppt; a range undoubtedly too high to measure a few ppt of ClO as previously reported in the literature and as suggested by our modeling results. To measure 7 ppt of ClO, we would require a detection limit of 1–2 ppt. This would necessitate a large amount of averaging with a significant loss in time resolution, as the detection limit improves by the square root of the number of spectra averaged. Assuming a detection limit of 100 ppt and averaging 100 spectra, our detection limits may lower by a factor of 10 but will nevertheless remain unsatisfactory for our application.

To further substantiate that detection limits are indeed an issue, we performed a series of experiments using SO_2 sample cells with the same instrumentation and under the same conditions. Repeat sets of measurements using 100 ppm-m and 10 ppm-m SO_2 sample cells as pictured in **Figure 3.23** were collected in triplicate, on Wednesday January 8 2018, Wednesday May 16 2018 and Wednesday May 17 2018. These dates were chosen somewhat arbitrarily but with the intention of having days both close and far apart in time. As pictured in **Figure 3.24**, as we would anticipate, we see a very good SO_2 fit using the 100 ppm-m sample cell and a fairly good fit for 10 ppm-m. For reference, these days were partly sunny/partly cloudy and no background subtraction was applied. The full set of fit results is presented in **Table 3.5**. There is more variation in the fit coefficients for the 10 ppm-m cell and these discrepancies are likely to be even greater for ClO. Calculating the detection limit from the reproducibility of consecutive observations, defined as three times the standard deviation, we obtain fairly large values, indicating that detection limit is an issue, even for ambient SO_2. However, because values are not consistent amongst the three days, this suggests that the fitting issues explained above are a factor nevertheless.

To calculate a theoretical detection limit for ClO, we multiply the SO_2 detection limit by a ratio that compares the size of absorption features from peak to peak in the fit range; approximately 0.4:1, as shown:

$$DL_{ClO} = DL_{SO2} \cdot \frac{\sigma'_{SO2}}{\sigma'_{ClO}}$$

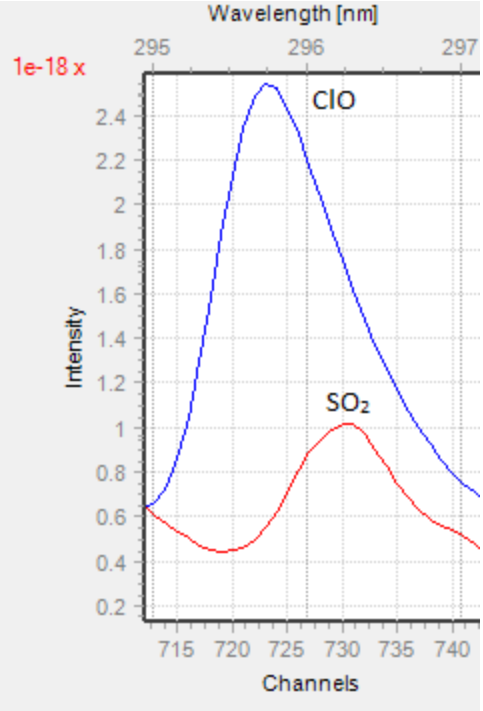

$$DL_{ClO} = DL_{SO2} \cdot \frac{0.4}{1}$$

Taking the 175 ppt detection limit minimum for SO_2, we obtain a ~70 ppt detection limit for ClO and extend our previous range to an approximate 70–150 ppt detection limit for ClO. An improvement in the detection limit is therefore certainly required, perhaps achieved by making amendments to the instrumental setup. One option could perhaps be to use a stronger lamp in order to increase the intensity of return light given that we are working with a long path length and in a lower intensity wavelength range. A discussion of all possible improvements to be made will be provided in our final section on future work.

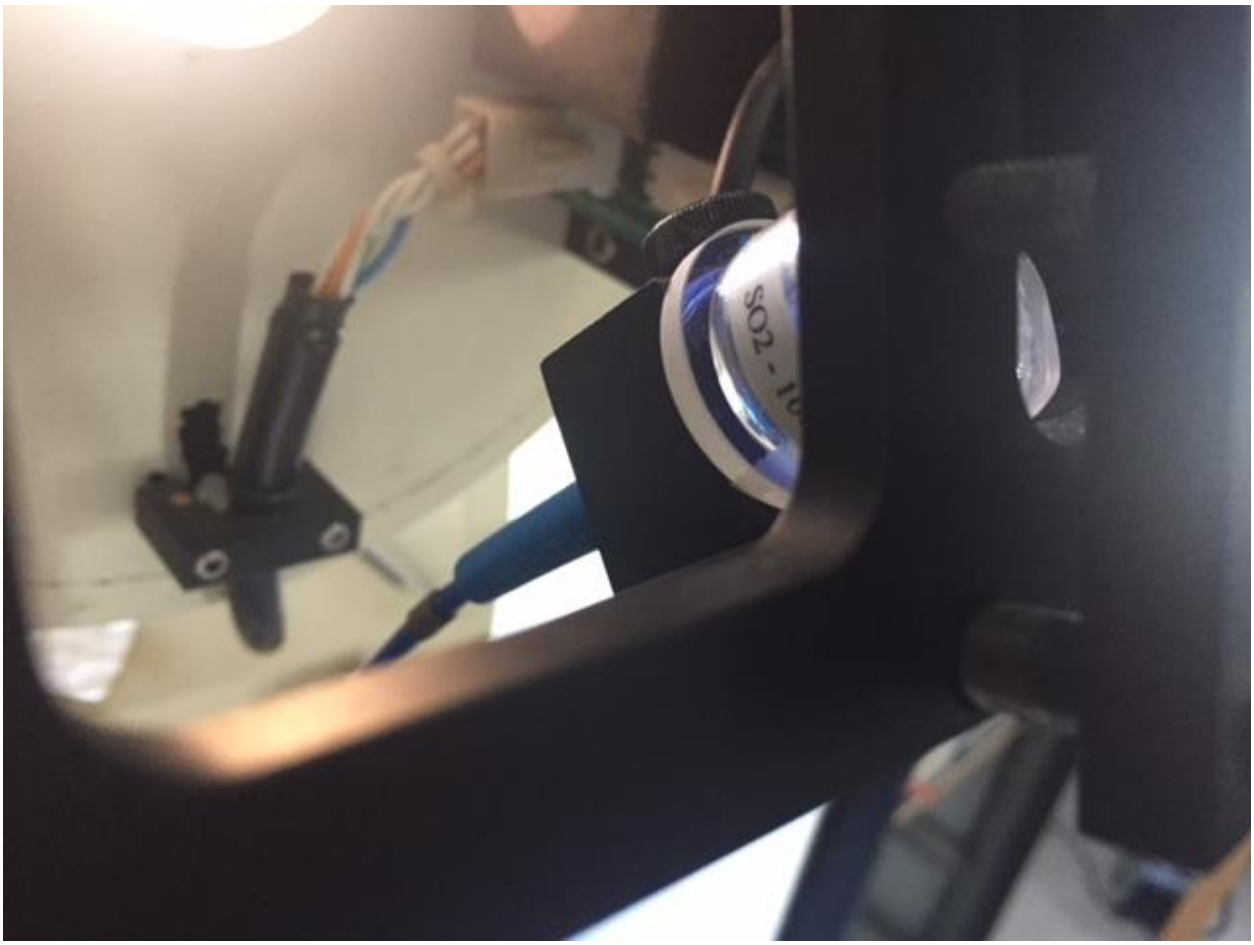

Figure 3.23: Photo of the SO_2 sample cell placed on top of the filter during spectra collection.

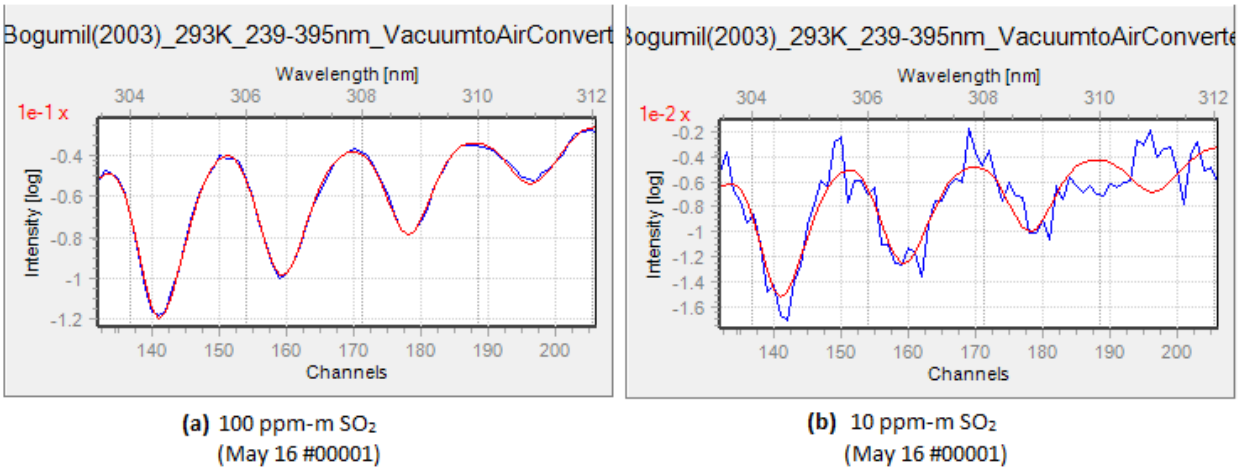

(a) 100 ppm-m SO_2 (May 16 #00001)

(b) 10 ppm-m SO_2 (May 16 #00001)

Figure 3.24: SO_2 sample cell fit results in the 303.5-312 nm fit range. **(a)** 100 ppm-m SO_2 sample cell **(b)** 10 ppm-m SO_2 sample cell.

Table 3.5: SO_2 sample cell results (fit range: 303.5 – 312 nm) and detection limit calculations for **(a)** January 3 2018 **(b)** May 16 2018 and **(c)** May 17 2018. Correction/calibration spectra used in fitting were collected on each given day, immediately following that day's measurements. Note: Subsequent spectra are 8 minutes apart (250 ms integration time, 2000 averages).

(a) Wednesday January 3 2018

Spectrum #	Fit Coefficient (molec cm^{-2}) 100 ppm-m SO_2 sample cell	Fit Coefficient (molec cm^{-2}) 10 ppm-m SO_2 sample cell
00001	2.00e+17 +/- 1.37e+15	2.97e+16 +/- 1.23e+15
00002	2.00e+17 +/- 1.59e+15	3.02e+16 +/- 1.42e+15
00003	2.00e+17 +/- 1.55e+15	3.04e+16 +/- 1.35e+15
00004	2.00e+17 +/- 1.46e+15	3.11e+16 +/- 1.45e+15
Standard Deviation, s	---	0.058e+16 or 0.58e+15
Detection Limit, 3s	---	0.174e+16 or 1.74e+15
Detection Limit, 3s (ppt)	---	175
Avg Experimental SO_2 (ppm-m)	80.3 +/- 0.60	12.2 +/- 0.55

(b) Wednesday May 16 2018

Spectrum #	Fit Coefficient (molec cm^{-2}) 100 ppm-m SO_2 sample cell	Fit Coefficient (molec cm^{-2}) 10 ppm-m SO_2 sample cell
00001	1.92e+17 +/- 1.54e+15	2.43e+16 +/- 2.17e+15
00002	1.93e+17 +/- 1.44e+15	2.28e+16 +/- 1.91e+15
00003	1.92e+17 +/- 1.71e+15	2.41e+16 +/- 1.87e+15
00004	1.93e+17 +/- 1.68e+15	2.45e+16 +/- 1.93e+15
Standard Deviation, s	<< for 10 ppm-m	0.077e+16 or 0.77e+15
Detection Limit, 3s	<< for 10 ppm-m	0.230e+16 or 2.30e+15
Detection Limit, 3s (ppt)	<< for 10 ppm-m	231
Avg Experimental SO_2 (ppm-m)	77.5 +/- 0.64	9.6 +/- 0.79

(c) Thursday May 17 2018

Spectrum #	Fit Coefficient (molec cm^{-2}) 100 ppm-m SO_2 sample cell	Fit Coefficient (molec cm^{-2}) 10 ppm-m SO_2 sample cell
00001	1.97e+17 +/- 1.55e+15	3.02e+16 +/- 1.59e+15
00002	1.96e+17 +/- 1.48e+15	2.58e+16 +/- 1.58e+15
00003	1.95e+17 +/- 1.48e+15	2.77e+16 +/- 1.47e+15
00004	1.96e+17 +/- 1.59e+15	2.50e+16 +/- 1.70e+15
Standard Deviation, s	<< for 10 ppm-m	0.231e+16 or 2.31e+15
Detection Limit, 3s	<< for 10 ppm-m	0.694e+16 or 6.94e+15
Detection Limit, 3s (ppt)	<< for 10 ppm-m	697
Avg Experimental SO_2 (ppm-m)	78.7 +/- 0.61	10.9 +/- 0.79

Revisiting the issue concerning dark current over-subtraction, this sample cell data was re-fit using a revised wavelength range, namely the 295-305 nm fit range previously used for ClO, to more clearly observe whether or not it influences these much larger mixing ratios. The results of this test are illustrated in **Figure 3.25**. On May 16th, the pixel at ~296 nm is absent for the 100 ppm-m sample cell but does appear for 10 ppm-m. Therefore, we would certainly see it for ambient SO_2 and ClO. However, it appears to be a non-issue on May 17th even though once again, the methods of data acquisition and fitting had remained the same and clear sky conditions persisted throughout. We are left with the question of why these DC and sunlight effects play a part on some days and not others, and what could be causing them.

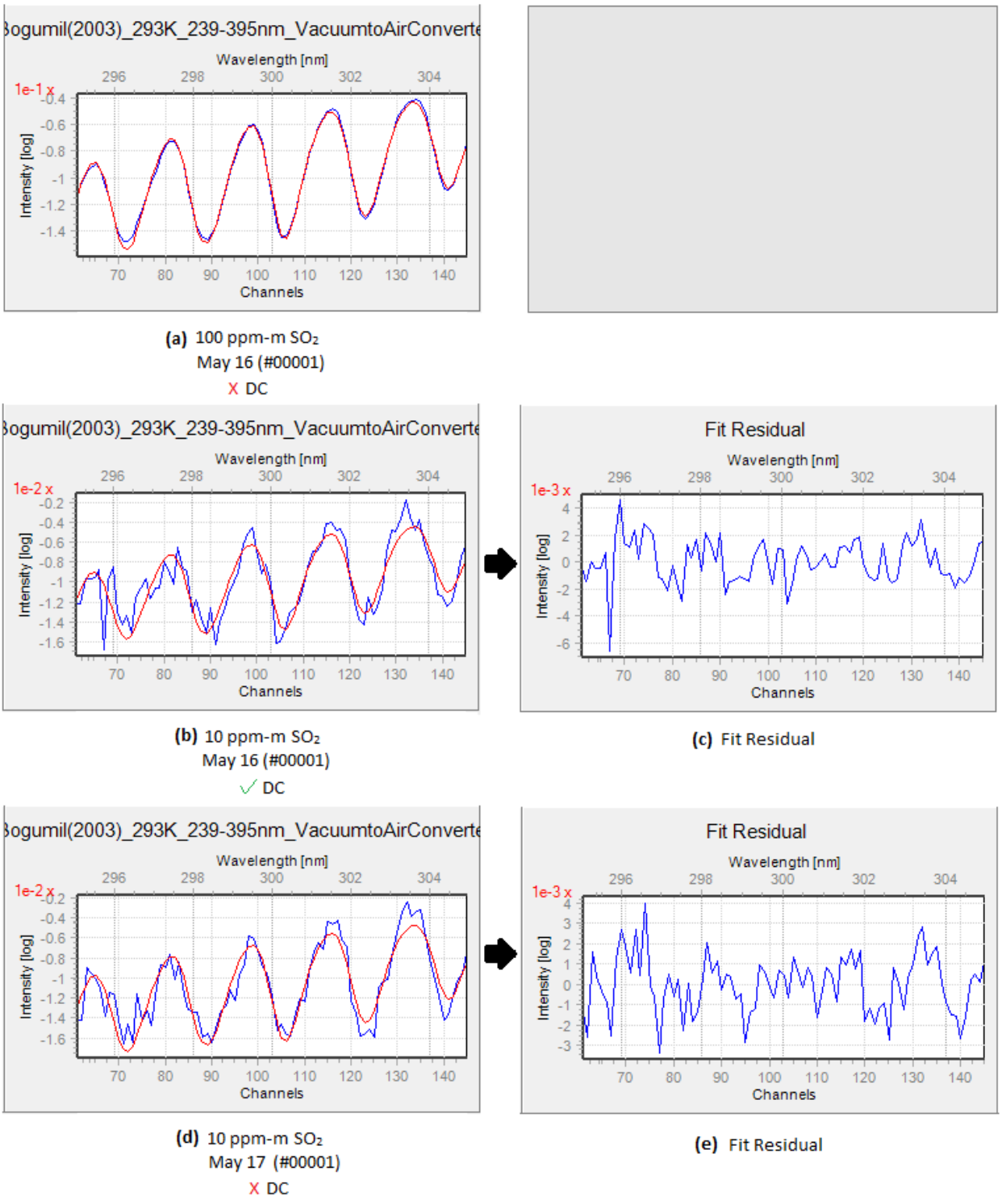

Figure 3.25: SO_2 sample cell fit results in the 295-305 nm fit range. **(a)** 100 ppm-m SO_2 sample cell **(b)** 10 ppm-m SO_2 sample cell on May 16th **(c)** Associated fit residual to (b) **(d)** 10 ppm-m SO_2 sample cell on May 17th **(e)** Associated fit residual to (d).

3.2.4: MAX-DOAS ClO Measurements

Analysis of the MAX-DOAS dataset has come with its own challenges and limitations. The practical limits of operating the instrument in the wintertime under below freezing temperatures was a factor, as was the formation of clouds as the day progressed in many cases. In contrast to our active DOAS results, the quality of the ClO fit on both the winter and summer measurement days were poor, with residuals on the order of $x10^{-1}$ and $x10^{-2}$ in most instances, rather than the preferred $x10^{-3}$ or $x10^{-4}$. This is likely due to the unreliability of the MAX-DOAS spectrometer at the low end of its range, around 300 nm. We observe an improvement in the residual when the fit range is shortened to exclude the shorter wavelengths above this cut-off, however, we are then reduced to only two or a single ClO feature, as is best seen in **Figure 3.26**. Our original intention was to employ both active and MAX-DOAS instruments and run them simultaneously, as on March 17 2017. In the very least, we had hoped MAX-DOAS measurements may assist us in interpreting our active DOAS results. Unfortunately, our MAX-DOAS fit results on this day were largely nonsensical and did not align with active DOAS results. We do however present a partial day of Summer 2017 MAX-DOAS ClO fit coefficients in **Figure 3.27**. Here, the crossover at the x-axis resembles what we have seen with active DOAS, however we do not have complete confidence in the tropospheric ClO dSCD's that are generated. The absorption spectrum of SO_2, seen once again in **Figure 3.28** is better suited to wavelengths greater than 300 nm and is more successfully measured using the MAX-DOAS technique, which we employ in the Welland Canal field study in the final section of our Experimental.

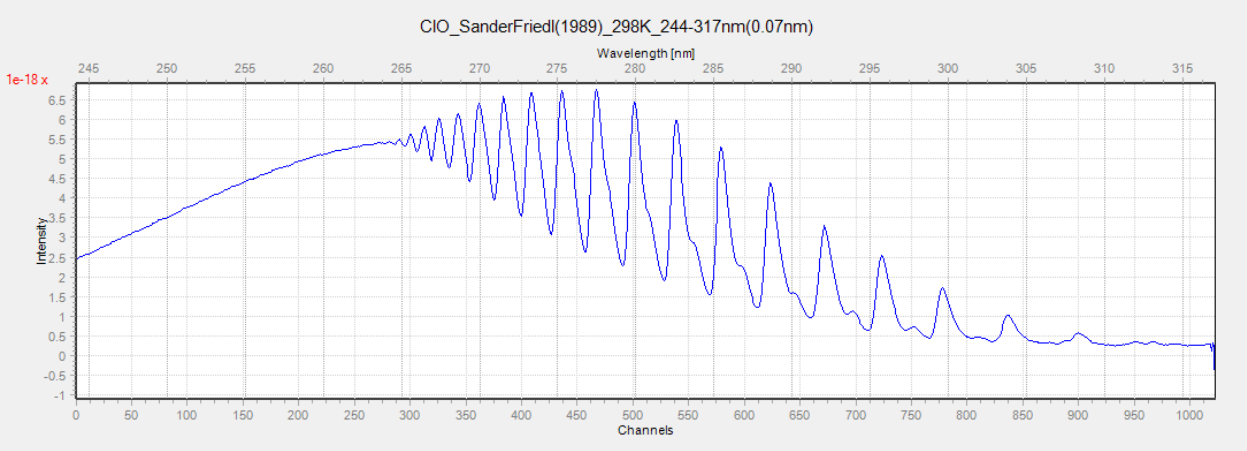

Figure 3.26: The ClO reference spectrum in DOASIS prior to convolution with our instrument function.

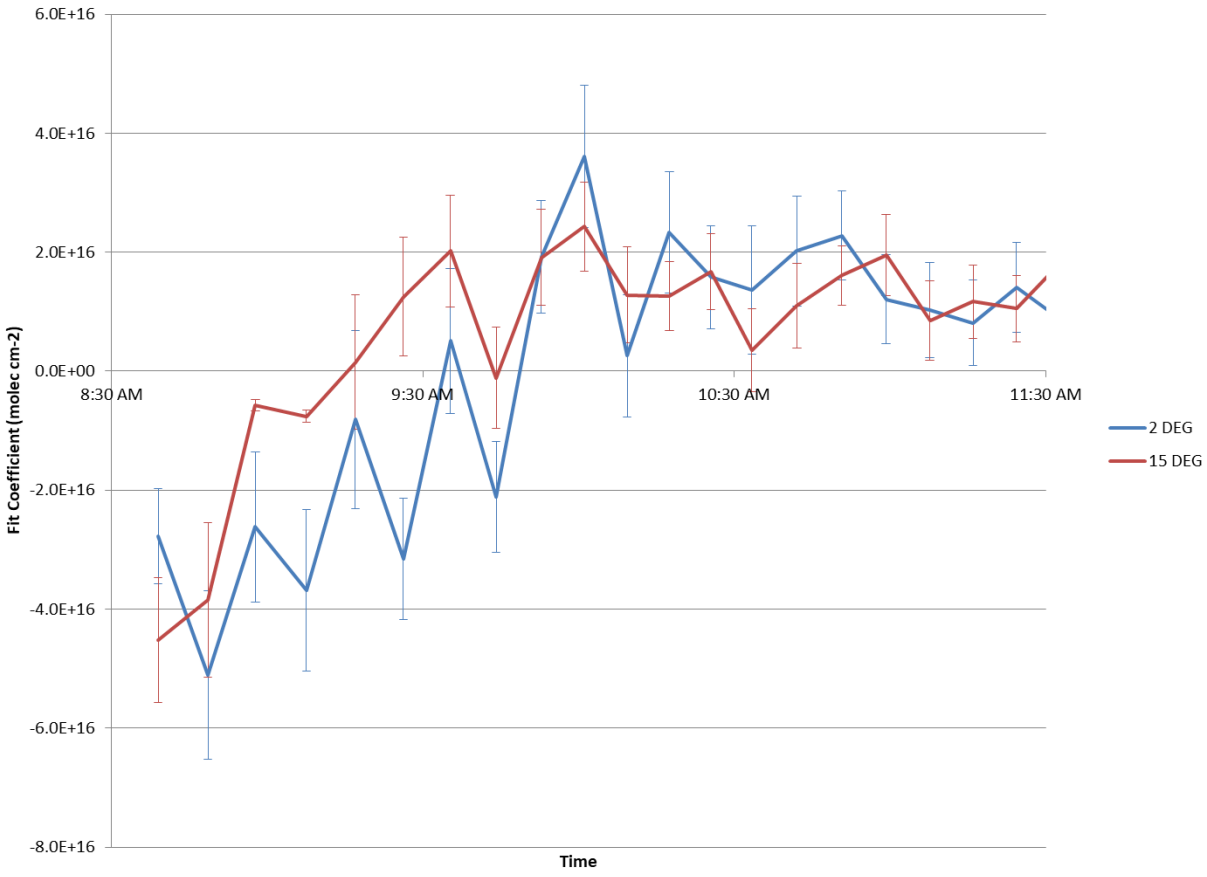

Figure 3.27: ClO fit coefficients on the morning of September 2 2017. Results obtained with the MAX-DOAS instrument operating at a temperature of 10.26 °C.

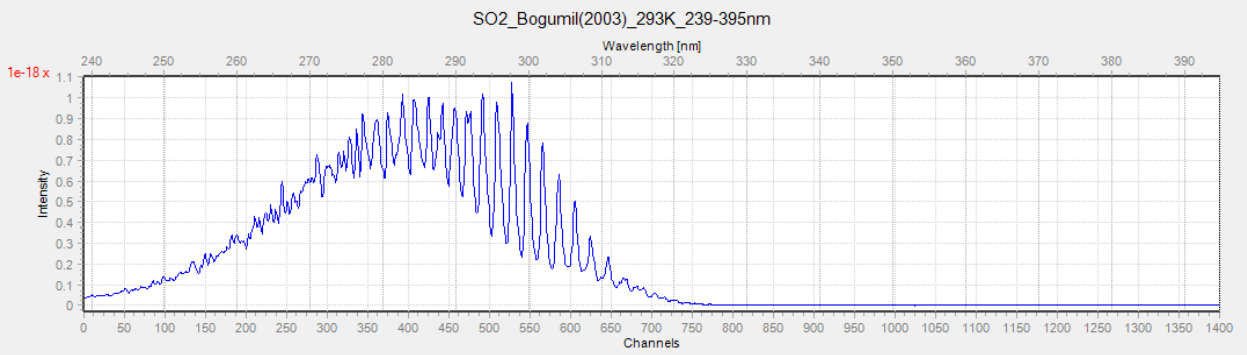

Figure 3.28: The SO_2 reference spectrum in DOASIS prior to convolution with our instrument function.

3.2.5: Modeling vs. Experimental Comparison

Modeling using AcuChem and the modified MCM + chlorine mechanism in Atchem predicted a maximum ClO mixing ratio on the order of a few ppt, within a few hours after sunrise, in line with what we would expect based on literature values. However, this modeling is somewhat rudimentary and represents a simplified version of a much more complex system. Zero dimensional box models assume

uniform mixing and homogenous composition throughout and may not be as accurate as a 1D or 2D model which would tell us more about variation with latitude and altitude. Although the MCM itself is robust, our model does not contain all chemical species or dynamics in the real atmosphere and relies on assumptions of starting concentrations that may or may not be accurate in our location, on our measurement days. In comparison to the models, our experimental results differ significantly, consisting of much larger peak ClO mixing ratios that seem to linger well into the afternoon; however these are likely affected by the fitting issues which we summarize in the following final section.

3.2.6: Study Wide Observations & Discussion

Overview

The scope of this research has evolved over the course of the project with feedback from an array of tests and experiments, resulting in a continually improved understanding of what we may be seeing and why. Adjustments were made in our approach, experimental design and data analysis procedures, to systematically refine or revise existing methods, with only those having a significant impact discussed in this report. In our proposed work, we had set out to measure ClO using the MAX-DOAS technique. The intention was to quantify the elusive ClO radical and obtain a vertical distribution, perhaps an ambitious endeavour from the start. Nevertheless, our motivations were fueled by the wonder of its presence in local ambient air and an ambition to fill an existing gap in the literature. Once the results started coming in, we were met with the development of unforeseen issues that set off a series of roadblocks. These results were not compatible to what had been seen in the literature and the possibility of not detecting any ClO was thought to be of greater likelihood than the unusually high values we were obtaining. There were a number of limiting conditions we had no control over, such as intermittent instrumental failure and unfavourable weather, resulting in unusable or unreliable data. Nevertheless, making amendments to the best of our ability, we did not deviate from our key research goal to identify and quantify ClO. Through the ebb and flow of the experimental process, we may yet derive significant information and provide evidence of its existence in an urban environment, with arguments for and against its feasibility discussed as follows.

Discussion of Possibilities:

Based solely on literature values, we anticipated low levels of ClO, likely on the order of a few ppt, given that we are removed from a large salt source such as an ocean or salt lake. Although this was corroborated by our modeling, our experimental results seem to suggest much higher mixing ratios, from the tens of ppt, up to over 150 ppt of ClO. We approach the discussion of these unanticipated results rigorously and from several opposing angles. In this section we present and summarize three possibilities: The ClO mixing ratios are real and tropospheric in nature; the ClO mixing ratios are real and stratospheric in nature; the ClO mixing ratios are not real and are likely biased due to experimental and/or fitting issues.

Real and Tropospheric

If we consider the possibility that the mixing ratios are real, we must also consider whether they are tropospheric or stratospheric in nature. Significant differences in mixing ratios on consecutive days and larger mixing ratios in the winter season would favour tropospheric ClO. Is it possible that the tons of road salt used on Toronto's many residential streets and highways over a long, snow-filled winter can accumulate to a larger source of chloride in aerosol than nearby sea spray? In looking at our results, we do observe significant day-to-day variations within the same measurement period, perhaps arising from differences in ClO-forming conditions in the troposphere between those days. However, there seems to be no direct correlation to snowfall amounts and the lasting presence of high mixing ratios into the summer months overshadows any wintertime enhancement. We note that both the 2017 and 2018 March measurements were made near the end of or after the winter season, respectively, and perhaps an accumulation of road salt could be the culprit in both cases, although this does not explain the August/September results. Alternatively, could there be another large unidentified source of chloride in close proximity to the study site and present year-round that we are unaware of? This is also possible though not very likely.

To supplement the active and MAX-DOAS measurements made, and to assist in our interpretation of the results, NO_2 and O_3 data was examined. NO_2 values were obtained from a co-located ThermoScientific Model 42i NO_x box, while O_3 records were acquired from the Toronto North Air Monitoring station at Environment and Climate Change Canada (4905 Dufferin St.). A graphical representation of NO_2 and O_3 mixing ratios between 6:00 AM LT and noon, on select measurement days, are shown in **Figure 3.29** and **Figure 3.30**, respectively. Both pollutants display typical diurnal profiles in these time series, exemplified by a morning NO_2 peak and a late afternoon O_3 peak, corresponding to high traffic "rush hour" emissions and a combination of photochemical formation of ozone and/or nocturnal boundary layer break-up. As such, NO_2 is at highest concentration on the weekdays, whereas O_3 is inversely correlated and higher on the weekend. Taking this into account, we speculate a greater likelihood of ClO detection on the Saturday, for instance. However, corresponding particulate chloride or $ClNO_2$ measurements are not available and we must ultimately rely on the DOAS evaluation of ClO itself.

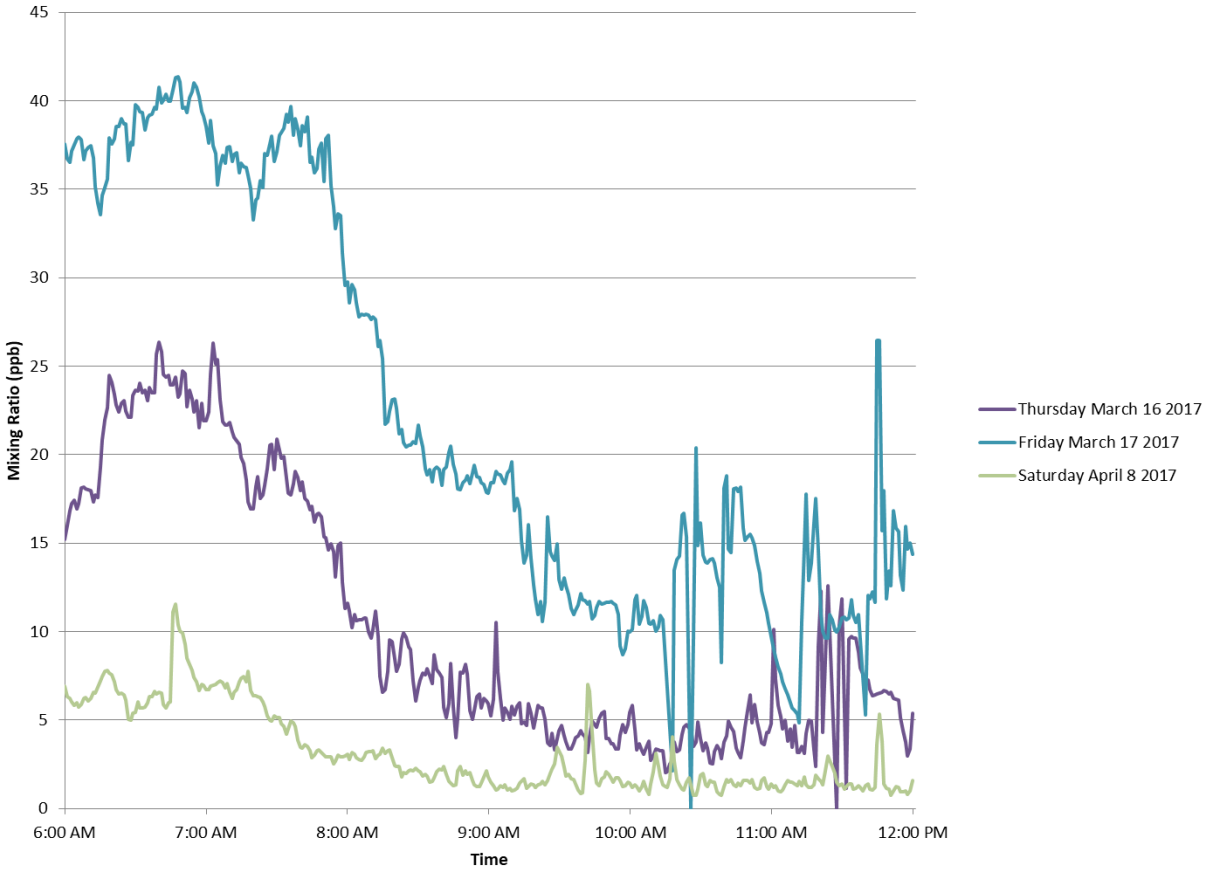

Figure 3.29: NO_2 mixing ratios on select measurement days for which elevated chloride levels are predicted. Data collected via a ThermoScientific Model 42i NOx box, with an output of one data point per minute. NO_2 calculated as the difference between measured NOx and NO.

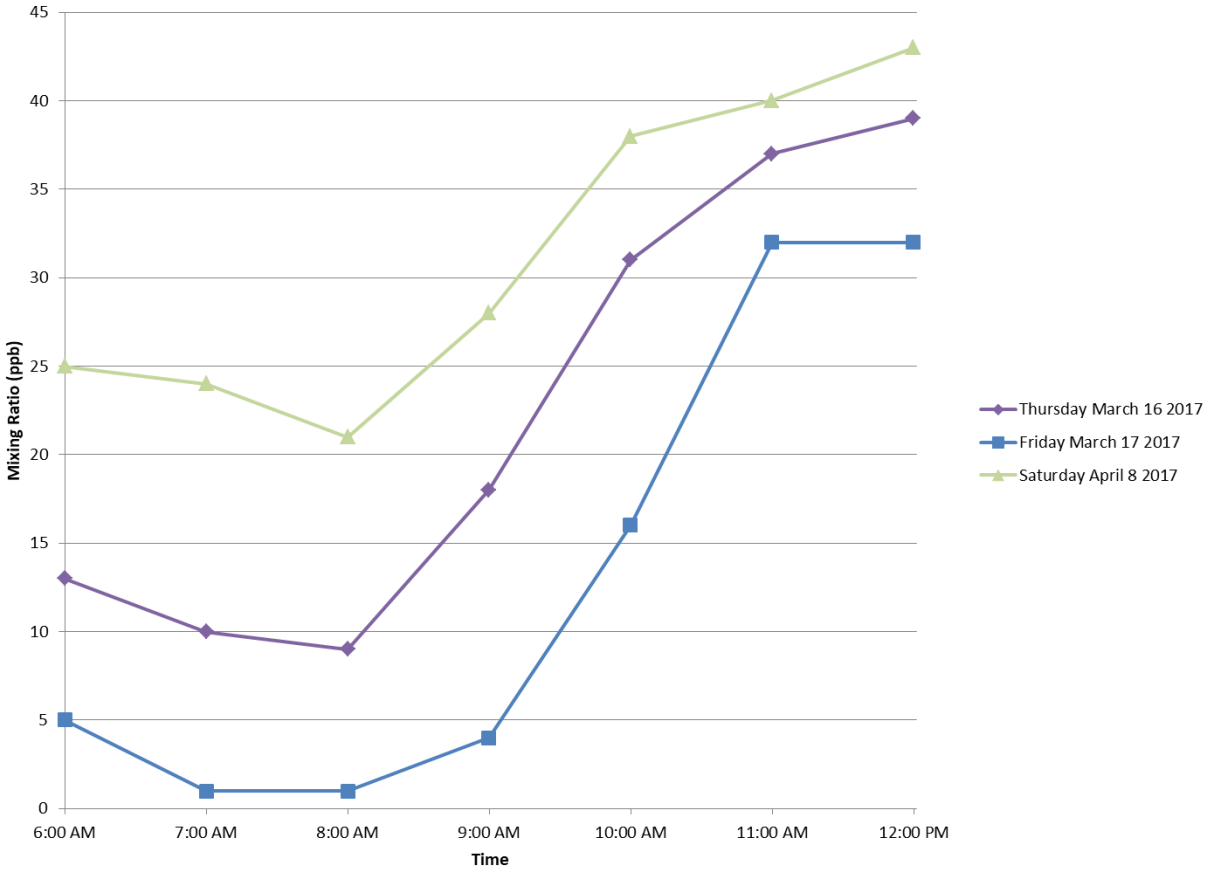

Figure 3.30: Hourly averaged O_3 mixing ratios on select measurement days for which elevated chloride levels are predicted. Data obtained from the Toronto North OMECC Air Monitoring Station.

Real and Stratospheric

Because we are seeing ClO in the fit independent of season, along with unusually high mixing ratios that tend to follow a sunrise to sunset pattern, this leans us in favour of a stratospheric component. Based on the chemistry, we originally predicted ClO to be present for a few hours in the morning only, as the $ClNO_2$ is depleted upon photolysis at sunrise and the ClO radical formed is quickly converted into other more stable species. Since it instead seems to prolong well into the afternoon hours, this would suggest we may be looking at stratospheric ClO. As seen with $ClNO_2$ measurements in the literature (Edwards et al., 2013) and supported by our modeling results (Figure 3.5), $ClNO_2$ is depleted by noontime and so a tropospheric afternoon peak of ClO is very unlikely. Our results are likewise in line with the diurnal pattern of ClO at higher altitudes as was seen in Figure 3.18. The enhanced ClO we observe and variation between days in our March data may be explained by ozone depletion events in the stratosphere, while August/September results would correspond to background ClO. Because the chemistry dictates that chlorine will be converted primarily to HCl rather than ClO, in order for these high mixing ratios to be real and tropospheric, it would mean an enormously large amount of HCl is also produced, which can be seen in our earlier modeling. HCl is arguably easier to measure, and so we would once again benefit from measurements of a second chlorine-containing

species to corroborate our results and provide us with an appreciation of chloride levels. If in fitting background spectra for ClO we obtain large mixing ratios that are comparable to, or slightly less than, those from measured spectra, this would moreover direct us toward a stratospheric answer. Subtracting background spectra prior to fitting yields high mixing ratios still, and although this was originally thought to support tropospheric ClO, it may be due to flaws in our methods of background subtraction; one of the concerns we touch upon next.

Using literature values of ClO mixing ratios in the lower stratosphere (Nedoluha et al., 2016), representing Antarctic springtime maxima, we may calculate a possible maximum stratospheric ClO signal for our experiment. This is accomplished through the use of a simple geometric approximation, defined as L = VCD/cos(SZA), in which L is a slant column density over a path length through the stratosphere prior to an arbitrary point of scatter in the troposphere. Integrating over 10–40 km while accounting for temperature and pressure changes, we obtain a total ClO column of approximately 2.1E+15 molec cm^{-2} as shown:

$$VCD = \int_{10\ km}^{40\ km} \chi_{ClO} \cdot n_{air} \cdot dx$$

At a given solar zenith angle, i.e. 49° at noon on March 17 2017, we obtain L = 3.2E+15 molec cm^{-2}. Then, taking into account the relative light intensities of the measured and corresponding background spectra on this date and time in the middle of our fit range at 300 nm, we obtain a value of 7.5E+13 molec cm^{-2}, in comparison to our original fit coefficient of 3.2E+15 molec cm^{-2}. This seems to suggest that a stratospheric signal could not account for the largest of the mixing ratios we've seen, leading us to our final and most likely conclusion.

Not Real

Lastly, we consider the likelihood that the mixing ratios obtained are not real and something has gone awry during data collection and/or data processing. On an experimental front, the issues we have encountered may be rooted in the use of our DOAS instruments or in flaws within our methodologies, but more likely stem from complications in fitting with the DOASIS software. In particular, we propose that a combination of one or more of the following issues may be altering our results; stray sunlight in the retroreflector resulting in a background effect that has not been adequately removed or accounted for, dark current signal over-subtraction, temperature shifts in the spectrometer, and insufficient detection limits.

In the daytime, interfering solar features are likely to be a large contributor to the inflated mixing ratios and consistent sunup to sundown patterns we have seen. As previously stated, we attempted to remove this background component by incorporating solar spectra into the fit in one of two ways. Fit results were identical, within error, whether the background was subtracted from measurement spectra or included in the fit scenario. Seeing as mixing ratios remained high, it is possible it was not adequately removed using our methods. Moreover, this manual subtraction of a background signal on a spectrum-by-spectrum basis is impractical and calls for the automation of this step or more

effectively, the minimization of background light to a negligible amount. This was attempted by way of a field of view test in which the size of the spot was adjusted (by positioning the fiber optic cable further away) to be slightly larger than the size of the fiber optic opening, as pictured in **Figure 3.31**. We then noted the change in intensity of the perceived scattered sunlight spectrum produced with the lamp turned off. Ideally, we would like to find a balance between minimizing sunlight (larger spot) and maximizing light intensity (smaller spot). However, even with the spot as diffuse as it can become, the solar features were reduced in intensity but did not disappear altogether. Because we are not able to record simultaneous background spectra using a shutter system, we were forced to use those collected at the same time on a different day. In testing however, results were comparable when a small number of spectra collected near noon were fit using background spectra taken immediately following with the lamp shut down. We therefore propose that a lack of simultaneously measured background spectra is not the issue; rather that we are inadvertently collecting background light at all, and if it is removable, we are not aware of the correct methods to remove it completely.

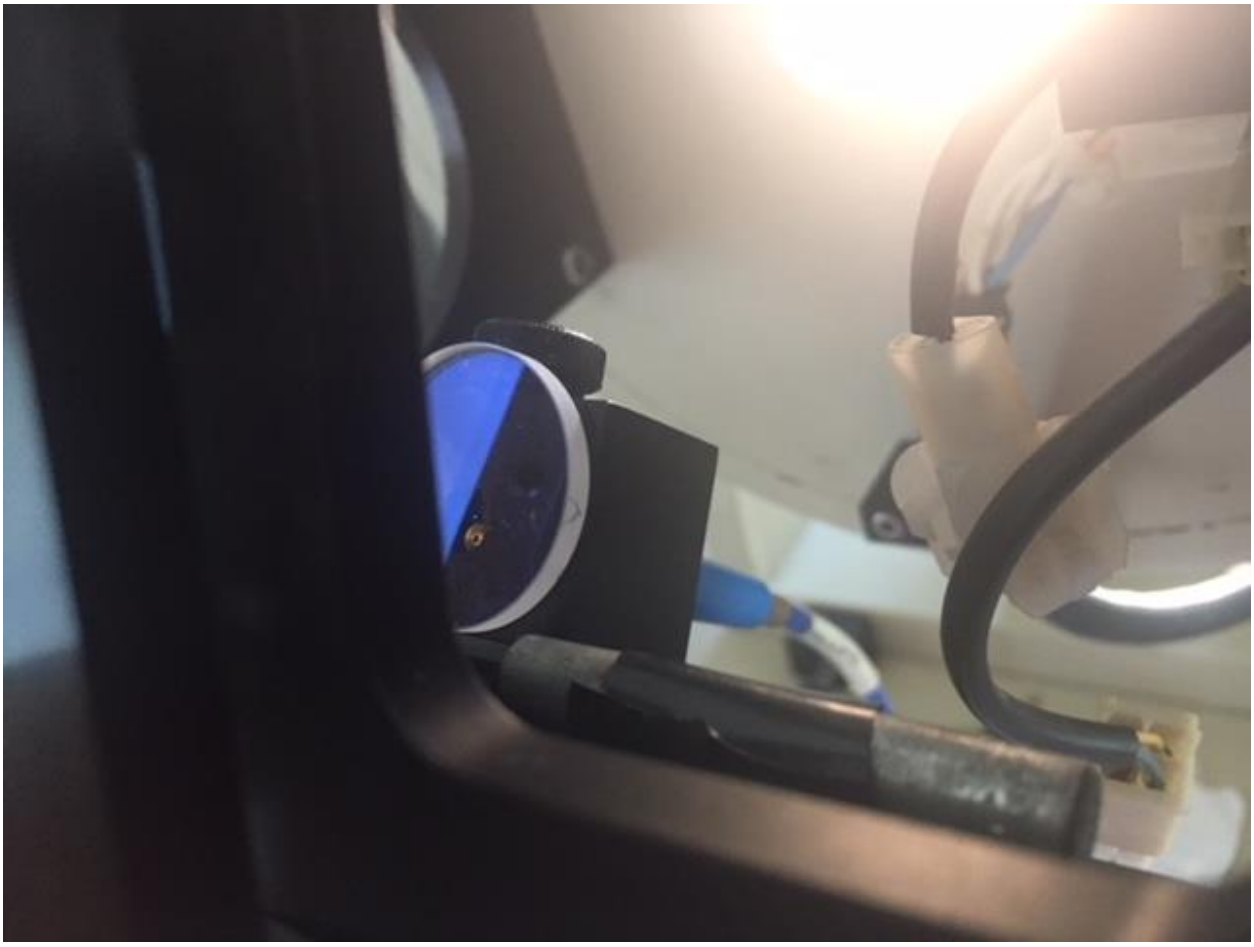

Figure 3.31: An image of the focused return light surrounding the fibre optic opening following adjustment of spot size.

A second visually discernable error is that concerning dark current over-subtraction. These inaccuracies emerge within the first steps of fitting, following the subtraction of offset and dark current, in which small dips in intensity are visible along the length of the measured spectra. Although these were superficially amended by estimating a correction factor, we are not aware of the root cause. It is known that there may be a nonlinear component to the dark current signal as it is dependent on the amount of charge already collected. We were able to rule this out by collecting several consecutive dark current spectra using varying integration times of 10000, 20000, and 30000 ms, and then normalizing it to same integration time to confirm its linearity. Akin to the background effect, the optimal solution may be to minimize or remove dark current altogether. Generally speaking, cooling the detector to lower temperatures will reduce the signal, as well as minimize the shot or Poisson noise of the dark current, which may be a contributing factor in the overall noise of the measurement (Burrows et al., 2018). Although dark current accounts for a comparatively small fraction of the total intensity, its effects are large when dealing with trace absorption. Another factor to consider are wavelength drifts due to thermal changes in the spectrometer, resulting in discrepancies between actual and measured wavelengths imprecisely accounted for by Hg calibration. Therefore, the use of a good temperature controller may help with both dark current and temperature stability.

Lastly, it is very possible that the detection limit of our instrumental setup is simply not low enough for this undertaking. Determination of detection limits for ClO were partially based upon those for SO_2, as deriving it from repeat measurements of a low-concentration sample of ClO was not an option. Using SO_2 detection limits scaled by the relative differential cross sections of ClO and SO_2, a value of 70 ppt was calculated for active DOAS, and if this is an accurate representation of our detection limits, ClO detection is not possible. An improvement in detection limits may provide some promise (i.e. via use of a stronger lamp, etc.), however if our original hypothesis is incorrect and ClO is present in exceptionally trace amounts, a detection limit issue may be unavoidable and out of our control. In investigating our unusually high mixing ratios, we fit for additional absorbers in the fit range, including NO_2, SO_2, BrO and HCHO in instances of highest and lowest apparent ClO. Although no single absorber appeared to be present consistently, it is possible that the issues we have experienced may have had an effect on the fits of these species as well. We note that removing O_3 from the fit generally did not make a large impact on mixing ratios. We end with a final note on the alignment of the active DOAS-retroreflector system, performed manually and subject to human error. On every occasion the light from the retroreflector was unaligned in order to take a lamp spectrum, the following realignment may have had a differing section of the arc focused onto the fibre optic opening, resulting in inconsistences in the lamp spectra. With the aforementioned experimental and fitting issues taken into consideration, we are nevertheless left with the question of why mixing ratios are so large in magnitude, why it is we obtain contrasting DOASIS outputs of highly negative mixing ratios and why there is so much noise between these high and low data points.

3.3: Experimental: MAX-DOAS SO_2 Measurements during the Welland Canal Field Study

We now briefly present and discuss the results of the MAX-DOAS portion of the Welland Canal Field Study. As this endeavour is secondary to our main project, more information on this particular study is available in Aida Khanbabakhani's Master's thesis. In the aforementioned report, active DOAS measurements of SO_2 confirmed that the monitored marine vessels were not significant sources of SO_2 due to low sulfur content in the ship fuel. The scarcity of SO_2, together with gaps in the MAX-DOAS data due to unfavourable cloud cover, renders our data difficult to interpret. We choose to present these results, which serve as our first foray into fitting for SO_2, as we did achieve some success in measuring SO_2 using the MAX-DOAS instrument. The resultant SO_2 fit coefficients on Day 1 and Day 2 of the study are displayed in **Figure 3.32** and **Figure 3.33** respectively. For reference, ships passed by on Day 1 at 12:25 PM, 13:28 PM and 15:20 PM and on Day 2 at 11:11 AM, 12:58 PM, 14:43 PM and 14:50 PM. Applying a rough geometric approximation, i.e. VCD = dSCDsinθ, assuming a boundary layer height of 1 km and a background SO_2 level of 1 ppb for calculation of the VCD, in good agreement with nearby Hamilton OME station data, we calculate background dSCD's of 3.6E+16 molec cm^{-2} for 4°, 1.8E+16 molec cm^{-2} for 8°, 1.0E+16 molec cm^{-2} for 15° and 5.0E+15 molec cm^{-2} for 30°. Based on these values, levels we measured are largely at or below background, with the exception of a possible peak occurring around the time the final ship passed on Day 1 at 15:20 PM and around the time that the final two ships crossed paths on Day 2 at 2:43-2:50 PM, since the higher dSCD's (excluding at 4°) are above background. Although Aida was measuring CO_2, and SO_2 with the active DOAS instrument, and did not detect spikes at these times, it is possible that plumes were emitted several tens of metres above the surface and were only captured by the MAX-DOAS at higher elevation angles. However, our results must be interpreted with caution, as owing to cloud-obstructed 90°'s, there is a temporal difference between the FRS and the measured spectra. They may also be attributable to a changing background rather than a ship plume peak. To validate these results, repeating this study on a more suitable day with clear skies and an alternate set of ships is in order. This endeavour is easily feasible due to the accessibility of the site and portability of the MAX-DOAS instrument.

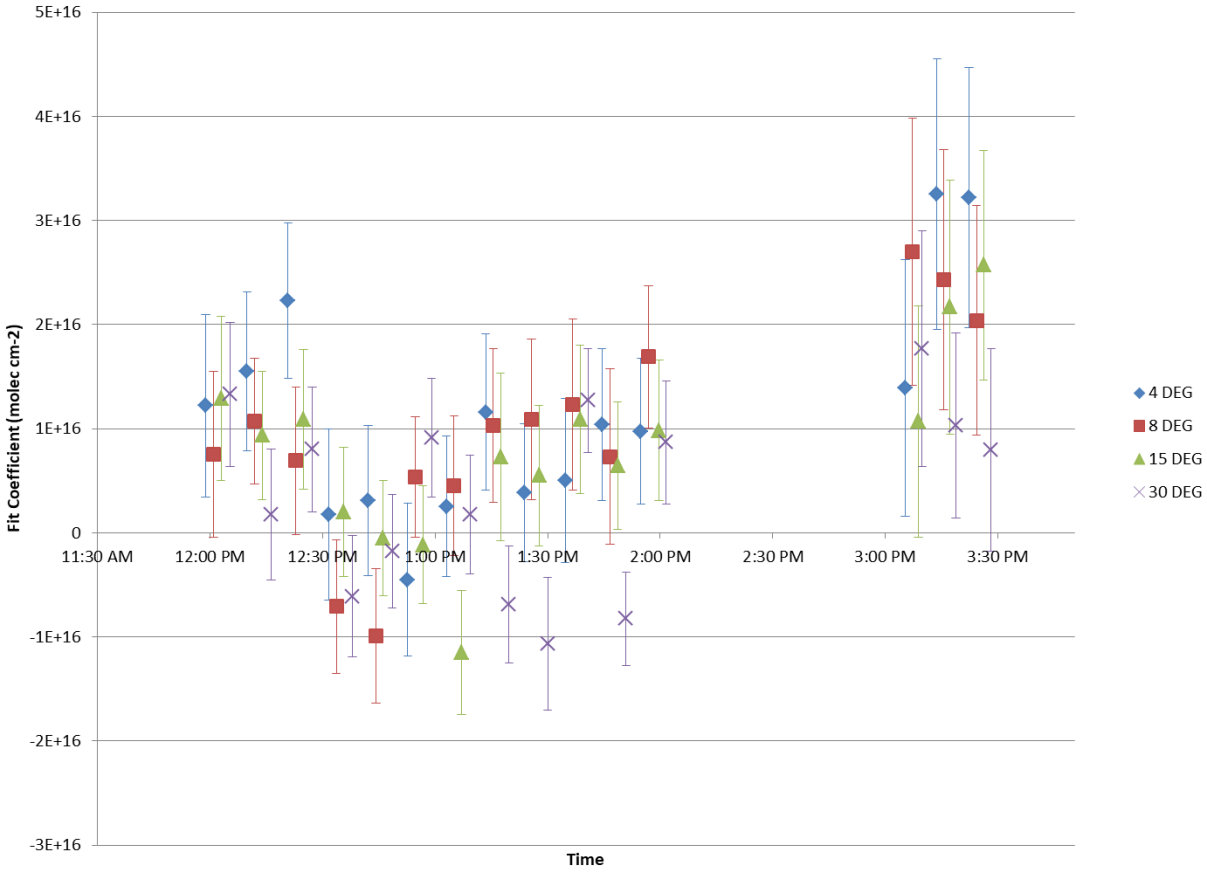

Figure 3.32: Time series of measured SO_2 dSCD's on Day 1, July 31 2017 at the Welland Canal. Ships crossed the MAX-DOAS at 12:25 PM, 13:28 PM and 15:20 PM.

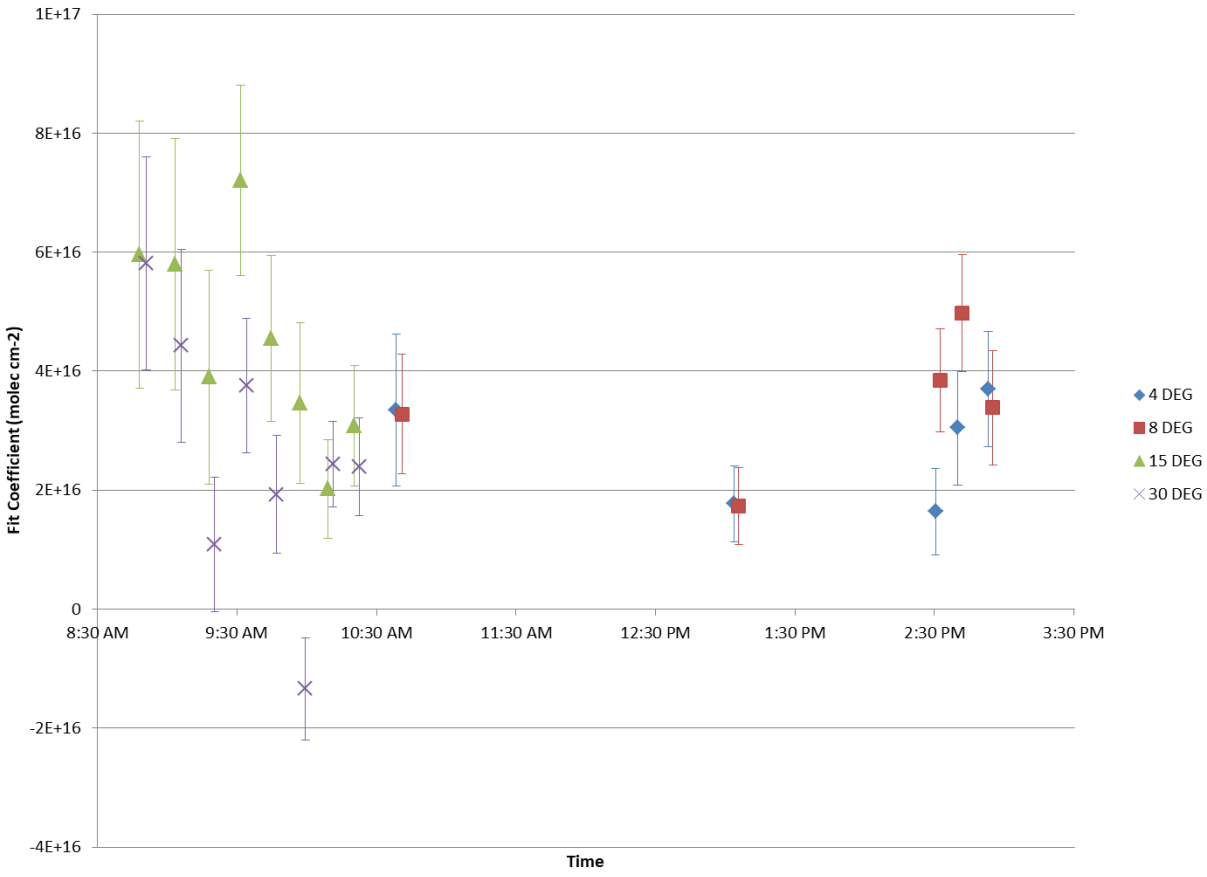

Figure 3.33: Time series of measured SO_2 dSCD's on Day 2, August 1 2017 at the Welland Canal. Ships crossed the MAX-DOAS at 11:11 AM, 12:58 PM, 14:43 PM and 14:50 PM.

CHAPTER 4: CONCLUSIONS & FUTURE WORK

To conclude, we first highlight our successes in modeling chlorine chemistry using the AcuChem and AtChem Online models. In future studies of ClO, we would look for a sharp transient peak, likely occurring within a couple hours after sunrise, before the nitryl chloride source is depleted around noontime. Although $ClNO_2$ levels have not been measured in Toronto as of yet, maximums reported in the literature have been upwards of 3 ppb and with these levels, we could see up to 7 ppt of ClO according to modeling results. However, to measure these levels experimentally, we would require a detection limit of 1–2 ppt and therefore, the answer to our research question of whether we have oxidative chlorine chemistry occurring during the wintertime due to the presence of road salt is uncertain at this point. The viability of ClO detection and the research project as a whole was put to the test in light of the limited and arguably questionable fit results derived from our active and MAX-DOAS measurements. We obtained unusually high mixing ratios, with a maximum of over 150 ppt; values substantially higher than what we may expect to observe based on literature values and preliminary modeling results. In view of this, we put forward two possibilities; that the ClO mixing ratios we've observed are real, possibly tropospheric but more likely stratospheric, but also that it may not be wise to accept these mixing ratios at face value due to several unresolved issues in processing the measured spectra. If the mixing ratios are real and indicative of tropospheric ClO levels, is it possible that road salt is a large source of atmospheric chlorine, perhaps more significant than sea salt aerosol? Or are we detecting stratospheric ClO? Because we are seeing ClO in the fit independent of season, along with unusually high mixing ratios that tend to follow a sunrise-to-sunset pattern, this leans us in favour of a stratospheric component. Although significant differences in mixing ratios on consecutive days and a larger mixing ratio in the winter season would seem to favour tropospheric ClO, this may be accounted for by ozone depletion events in the stratosphere. We therefore present a stratospheric conclusion as the more likely explanation of our findings if what we have seen is not simply an artifact of the experiment due to interfering sunlight. As well, the feasibility and practicality of measuring SO_2 in ship plumes using the portable MAX-DOAS instrument was demonstrated in this work, and our methods may be applicable to future field studies.

While clear-cut results and a definitive final conclusion are not on offer, we emphasize that this work in the very least contributes to a piece of the puzzle and serves to guide us in the right direction. We once again note that only a single successful attempt at measuring ClO using MAX-DOAS has been made (Lee et al., 2008) and although more instances of active-DOAS measurements have been reported, the investigators likely used better instruments tailored and fine-tuned for their specific applications. Nevertheless, there currently exists a large uncertainty in both the mechanistic details of heterogeneous chlorine chemistry and the emissions inventories of chlorine radical precursors (Faxon and Allen, 2013). The reported uptake coefficients of N_2O_5 and yields of $ClNO_2$ vary widely in the literature (Faxon and Allen, 2013). Further, although both natural and anthropogenic (i.e. cooling towers, water treatment facilities, swimming pool chlorination) sources have been identified, inventories are not comprehensive or definitive, due in part to an incomplete understanding of the biogeochemical cycle of chlorine (Faxon and Allen, 2013). Referring back to Table 1.2 and Table 1.3, we note that ClO measurements were made prior to the first measurements of $ClNO_2$ and therefore it was not considered as a major source of

chlorine. Ultimately, this research must be ongoing within the scientific community if we wish to close this gap in knowledge on tropospheric ClO.

We stress that further insight is required to address the limitations of this particular study and we suggest ways in which the objective of quantifying ClO using the DOAS technique, or a related chlorine-containing species through other means, might be achieved. Our experimental and data analysis procedures were re-optimized to the best of our ability and to the best of our knowledge, however further development and validation of our methods may be necessary. Insufficient detection limits for ClO using the active DOAS instrument were likely a defining hurdle in our measurements, calculated to be upwards of 70–150 ppt. Detection limits may be improved by making various changes to the experimental system. This may include, in order of importance; the use of a more powerful light source, a larger retroreflector (signal directly proportional to size), larger uncoated mirrors (light capture proportional to the square of the diameter; ours coated to improve longevity with a decrease in reflectivity), a filter with a cut-off closer to our fit range (to further reduce stray light) and the use of a better spectrometer and temperature controller. In retrospect, although we did require a long path length to increase ClO sensitivity, which increases linearly with distance, we are losing light at a faster rate due to Rayleigh scattering and so it may be a delicate balance to operate at the optimum path length. As mentioned previously, the use of a very large number of averages may improve detection limits but with the trade-off of very low time resolution. However, taking all of the above into consideration, we may be able to improve detection limits considerably. For example, averaging to obtain a factor of 2 improvement in detection limits, together with the upgrade from a 150 W bulb to 500 W bulb (factor of 3.3 improvement in detection limit), and the upgrade from a 8” mirror to a 12” mirror (factor of 2.25 improvement in detection limit) totals in a factor of ~15 improvement in detection limits. We could therefore go from a 70–150 ppt detection limit to ~5–10 ppt, although this is still not the 1–2 ppt we require. The high noise in our signal is likely a combination of instrumental noise in the CCD detector, thermal noise and perhaps shot noise. We presume the noise in the offset, dark current and background spectra are combining to contribute to the overall noise in our results and again we may reduce this noise by increasing the number of averages, and therefore the collection time, of these spectra to beyond the 8 minutes used. Most useful would be to eliminate or minimize the interference of background sunlight, perhaps achieved through shielding the retroreflector or changing the pointing direction. An equally beneficial solution would involve implementing a shutter system modification to our instrument to allow light switching in which we take near-simultaneous measurement and background spectra. Because there is only so much we can do experimentally, with our current system located outdoors, the solution to background light artifacts would likely have to come from advanced background corrections during processing of the spectra.

It is possible we may have seen some success were we able to fully utilize the MAX-DOAS instrument, given this technique’s unique ability to measure higher in the atmosphere and our inclination that ClO may be present primarily in the residual layer. The use of a newer MAX-DOAS instrument and spectrometer more suited to our wavelength range would be of value. Then, expanding the scope of our MAX-DOAS measurements to comprise several elevation angles would allow us to determine whether there exists an altitude dependency. If identification and quantification of ClO by

this method is deemed reliable, we may complete radiative transfer modeling for conversion of MAX-DOAS SCDS's into VCD's. We may also benefit from data sampling at one or more alternate locations. If possible, a small-scale field study conducted with the intent of securing an elevated site for placement of the retroreflector, as well as for performing the experiment in a rural area with less road salt, could be of comparative value. On a practical front, a DOASIS JScript to automate active DOAS fitting using a variable background spectrum would be of value, in order to process more data more efficiently. Perhaps the best chance to succeed in this endeavour will come from a shift in focus to an alternate target molecule by other methods. At present, Dr. Cora Young's research group at York University is pursuing the measurement of HCl using a Picarro CRDS Analyzer; this approach may likewise provide us with an indication of ambient chlorine levels in Toronto.

We highlight the possible implications of our findings, that is to say, if chlorine chemistry is indeed occurring, it can significantly affect the oxidative capacity of an urban atmosphere such as that in Toronto. An effect on ambient air quality near the surface comes with associated environmental and health concerns for a densely populated city and mitigation strategies for sources and precursors, if possible, may be worth consideration. On a grander scale, we must recognize the impact on tropospheric ozone, a greenhouse gas with a positive radiative forcing and a direct contributor to climate change (Finlayson-Pitts and Pitts, 2000). Through continuation of this research, the discovery of significant levels of ClO and other chlorinated species may call for the incorporation of this chemistry into regional air quality models and down the line, in air quality policy development.

CHAPTER 5: REFERENCES

Baker, A. K., Slemr, F., and Brenninkmeijer, C. A. M.: Analysis of non-methane hydrocarbons in air samples collected aboard the CARIBIC passenger aircraft, Atmos. Meas. Tech., 3, 311–321, 2010.

Behnke, W., and Zetzsch, C.: Heterogeneous photochemical formation of Cl atoms from NaCl aerosol, NOx and ozone, J. Aerosol Sci., 21, S229–S232, 1990.

Bertram, T. H. and Thornton, J. A.: Toward a general parameterization of N2O5 reactivity on aqueous particles: the competing effects of particle liquid water, nitrate and chloride, Atmos. Chem. Phys., 9, 8351–8363, 2009.

Bobrowski, N. and Filsinger, F.: Mini MAX-DOAS Manual, Institute of Environmental Physics, University of Heidelberg, 2005.

Braun, W., Herron, J. T., and Kahaner, D. K.: Acuchem: A computer program for modeling complex chemical reaction systems, Int. J. Chem. Kinet., 20, 51–62, 1988.

Brown, S. S., Dubé, W. P., Osthoff, H. D., Wolfe, D. E., Angevine, W. M., and Ravishankara, A. R.: High resolution vertical distributions of NO3 and N2O5 through the nocturnal boundary layer, Atmos. Chem. Phys., 7, 139–149, 2007.

Brown, S. S. and Stutz, J.: Nighttime radical observations and chemistry, Chem. Soc. Rev., 41, 6405–6447, 2012.

Burrows, J. P., Richter, A., and Wittrock, F.: Institute of Environmental Physics, University of Bremen: DOAS Glossary, http://www.iup.uni-bremen.de/doas/doas_glossary.htm, 2018.

Chang, C. T., Liu, T. H., and Jeng, F. T.: Atmospheric concentrations of the Cl atom, ClO radical, and HO radical in the coastal marine boundary layer, Environ. Res., 94, 67–74, 2004.

Edwards, P. M., Young, C. J., Aiken, K., deGouw, J., Dubé, W. P., Geiger, F., Gilman, J., Helmig, D., Holloway, J. S., Kercher, J., Lerner, B., Martin, R., McLaren, R., Parrish, D. D., Peischl, J., Roberts, J. M., Ryerson, T. B., Thornton, J., Warneke, C., Williams, E. J., and Brown, S. S.: Ozone photochemistry in an oil and natural gas extraction region during winter: simulations of a snow-free season in the Uintah Basin, Utah, Atmos. Chem. Phys., 13, 8955–8971, 2013.

Farman, J. C., Gardiner, B. G., and Shanklin, J. D.: Large losses of total ozone in Antarctica reveal seasonal ClOx/NOx interaction, Nature, 315, 207–210, 1985.

Faxon, C. B. and Allen, D. T.: Chlorine chemistry in urban atmospheres: a review, Environ. Chem., 10, 221–233, 2013.

Finlayson-Pitts, B. J., Ezell, M. J., and Pitts Jr, J. N.: Formation of chemically active chlorine compounds by reactions of atmospheric NaCl particles with gaseous N2O5 and ClNO2, Nature, 337, 241–244, 1989.

Finlayson-Pitts, B. J. and Pitts Jr, J. N.: Chemistry of the Upper and Lower Atmosphere: Theory,

Experiments, and Applications, Academic Press, San Diego, CA, 2000.

Haskins, J. D., Jaeglé, L., Shah, V., Lee, B. H., Lopez-Hilfiker, F. D., Campuzano-Jost, P., Schroder, J. C., Day, D. A., Guo, H., Sullivan, A. P., Weber, R., Dibb, J., Campos, T., Jimenez, J. L., Brown, S. S., and Thornton, J. A.: Wintertime Gas-Particle Partitioning and Speciation of Inorganic Chlorine in the Lower Troposphere Over the Northeast United States and Coastal Ocean, JGR Atmos., 123, 12897–12916, 2018.

Holloway, A. M. and Wayne, R. P.: Atmospheric Chemistry, RSC Publishing, Cambridge, 2010.

Hönninger, G., von Friedeburg, C., and Platt, U.: Multi axis differential optical absorption spectroscopy (MAX-DOAS), Atmos. Chem. Phys., 4, 231–254, 2004.

Jacob, D. J.: Introduction to Atmospheric Chemistry, Princeton University Press, Princeton, NJ, 1999.

Jenkin, M. E., Saunders, S. M., and Pilling, M. J.: The tropospheric degradation of volatile organic compounds: a protocol for mechanism development, Atmos. Environ., 31, 81–104, 1997.

Keller-Rudek, H., Moortgat, G. K., Sander, R., and Sörensen, R.: The MPI-Mainz UV/VIS spectral atlas of gaseous molecules of atmospheric interest, Earth Syst. Sci. Data, 5, 365–373, 2013.

Kolesar, K. R., Mattson, C. N., Peterson, P. K., May, N. W., Prendergast, R. K., and Pratt, K. A.: Increases in wintertime PM2.5 sodium and chloride linked to snowfall and road salt application, Atmos. Environ., 177, 195–202, 2018.

Kuwahara, T., Nagahama, T., Maezawa, H., Kojima, Y., Yamamoto, H., Okuda, T., Mizuno, N., Nakane, H., Fukui, Y., and Mizuno, A.: Ground-based millimeter-wave observation of stratospheric ClO over Atacama, Chile in the mid-latitude Southern Hemisphere, Atmos. Meas. Tech., 5, 2601–2611, 2012.

Lee, C., Kim, Y. J., Lee, H., and Choi, B. C.: MAX-DOAS Measurements of ClO, SO2 and NO2 in the Mid-Latitude Coastal Boundary Layer and a Power Plant Plume, Advanced Environmental Monitoring, Springer Netherlands, 37–49, 2008.

Liao, J., Huey, G. L., Liu, Z., Tanner, D. J., Cantrell, C. A., Orlando, J. J., Flocke, F. M., Shepson, P. B., Weinheimer, A. J., Hall, S. R., Ullman, K., Beine, H. J., Wang, Y., Ingall, E. D., Stephens, C. R., Hornbrook, R. S., Apel, E. C., Riemer, D., Fried, A., Mauldin, R. L., Smith, J. N., Staebler, R. M., Neuman, J. A., and Nowak, J. B.: High levels of molecular chlorine in the Arctic atmosphere, Nat. Geosci., 7, 91–94, 2014.

Manney, G. L. and Lawrence, Z. D.: The major stratospheric final warming in 2016: dispersal of vortex air and termination of Arctic chemical ozone loss, Atmos. Chem. Phys., 16, 15371–15396, 2016.

Mielke, L. H., Furgeson, A., and Osthoff, H. D.: Observation of ClNO2 in a Mid-Continental Urban Environment, Environ. Sci. Technol., 45, 8889–8896, 2011.

Molina, M. J. and Rowland, F. S.: Stratospheric sink for chlorofluoromethanes: chlorine atom-catalysed destruction of ozone, Nature, 249, 810–812, 1974.

Nedoluha, G. E., Connor, B. J., Mooney, T., Barrett, J. W., Parrish, A., Gomez, R. M., Boyd, I., Allen, D. R., Kotkamp, M., Kremser, S., Deshler, T., Newman, P., and Santee, M. L.: 20 years of ClO measurements in the Antarctic lower stratosphere, Atmos. Chem. Phys., 16, 10725–10734, 2016.

Osthoff, H. D., Roberts, J. M., Ravishankara, A. R., Williams, E. J., Lerner, B. M., Sommariva, R., Bates, T. S., Coffman, D., Quinn, P. K., Dibb, J. E., Stark, H., Burkholder, J. B., Talukdar, R. K., Meagher, J., Fehsenfeld, F. C., and Brown, S. S.: High levels of nitryl chloride in the polluted subtropical marine boundary layer, Nat. Geosci., 1, 324–328, 2008.

Platt, U. and Janssen, C.: Observation and role of the free radicals NO3, ClO, BrO and IO in the troposphere, Faraday Discuss., 100, 175–198, 1995.

Platt, U. and Stutz, J.: Differential Optical Absorption Spectroscopy: Principles and Applications, Springer-Verlag Berlin Heidelberg, 2008.

Pöhler, D., Vogel, L., Frieß, U., and Platt, U.: Observation of halogen species in the Amundsen Gulf, Arctic, by active long-path differential optical absorption spectroscopy, Proc. Natl. Acad. Sci. USA., 107, 6582–6587, 2010.

Ricaud, P., Chipperfield, M. P., Waters, J. W., Russell III, J. M., and Roche, A. E.: Temporal evolution of chlorine monoxide in the middle stratosphere, J. Geophys. Res., 105, 4459–4469, 2000.

Riedel, T. P., Bertram, T. H., Crisp, T. A., Williams, E. J., Lerner, B. M., Vlasenko, A., Li, S. -M., Gilman, J., de Gouw, J., Bon, D. M., Wagner, N. L., Brown, S. S., and Thornton, J. A.: Nitryl Chloride and Molecular Chlorine in the Coastal Marine Boundary Layer, Environ. Sci. Technol., 46, 10463–10470, 2012.

Riedel, T. P., Wolfe, G. M., Danas, K. T., Gilman, J. B., Kuster, W. C., Bon, D. M., Vlasenko, A., Li, S. -M., Williams, E. J., Lerner, B. M., Veres, P. R., Roberts, J. M., Holloway, J. S., Lefer, B., Brown, S. S., and Thornton, J. A.: An MCM modeling study of nitryl chloride (ClNO2) impacts on oxidation, ozone production and nitrogen oxide partitioning in polluted continental outflow, Atmos. Chem. Phys., 14, 3789–3800, 2014.

Sander, S. P., Golden, D. M., Kurylo, M. J., Moortgat, G. K., Wine, P. H., Ravishankara, A. R., Kolb, C. E., Molina, M. J., Finlayson-Pitts, B. J., Huie, R. E., and Orkin, V. L.: Chemical Kinetics and Photochemical Data for Use in Atmospheric Studies, Evaluation No. 15, JPL Publication 06-2, Jet Propulsion Laboratory, Pasadena, CA, 2006.

Saunders, S. M., Jenkin, M. E., Derwent, R. G., and Pilling, M. J.: Protocol for the development of the Master Chemical Mechanism, MCM v3 (Part A): tropospheric degradation of non-aromatic volatile organic compounds, Atmos. Chem. Phys., 3, 161–180, 2003.

Solomon, S., Ivy, D. J., Kinnison, D., Mills, M. J., Neely, R. R., and Schmidt, A.: Emergence of healing in the Antarctic ozone layer, Science, 353, 269–274, 2016.

Strahan, S. E. and Douglass, A. R.: Decline in Antarctic Ozone Depletion and Lower Stratospheric Chlorine Determined From Aura Microwave Limb Sounder Observations, Geophys. Res. Lett., 45, 382–390, 2018.

Stutz, J., Ackermann, R., Fast, J. D., and Barrie, L.: Atmospheric reactive chlorine and bromine at the Great Salt Lake, Utah, Geophys. Res. Lett., 29, 18-1–18-4, 2002.

Thornton, J. A., Kercher, J. P., Riedel, T. P., Wagner, N. L., Cozic, J., Holloway, J. S., Dubé, W. P., Wolfe, G. M., Quinn, P. K., Middlebrook, A. M., Alexander, B., and Brown, S. S.: A large atomic chlorine source inferred from mid-continental reactive nitrogen chemistry, Nature, 464, 271–274, 2010.

Tuckermann, M., Ackermann, R., Gōlz, C., Lorenzen-Schmidt, H., Senne, T., Stutz, J., Trost, B., Unold, W., and Platt, U.: DOAS-observation of halogen radical-catalysed arctic boundary layer ozone destruction during the ARCTOC-campaigns 1995 and 1996 in Ny-Ålesund, Spitsbergen, Tellus B, 49, 533–555, 1997.

Young, C. J., Washenfelder, R. A., Roberts, J. M., Mielke, L. H., Osthoff, H. D., Tsai, C., Pikelnaya, O., Stutz, J., Veres, P. R., Cochran, A. K., VandenBoer, T. C., Flynn, J., Grossberg, N., Haman, C. L., Lefer, B., Stark, H., Graus, M., de Gouw, J., Gilman, J. B., Kuster, W. C., and Brown, S. S.: Vertically Resolved Measurements of Nighttime Radical Reservoirs in Los Angeles and Their Contribution to the Urban Radical Budget, Environ. Sci. Technol., 46, 10965–10973, 2012.

APPENDIX

A1: AcuChem Model Input

Example: 9 AM Input

```
;Acuchem ClO Model
21.03.2016 09:00, T: 273 K (0 C), P: 1 atm, Altitude: 0 m (ground level), Relative Humidity: 50%
1111

;All ClO Production Reactions
;1, O + OClO = ClO + O2, 7.1E-14
;2, O + Cl2O = ClO + ClO, 3.9E-12
3, O + HOCl = OH + ClO, 1.7E-13
4, OH + HOCl = H2O + ClO, 4.8E-13
5, HO2 + Cl = OH + ClO, 7.9E-12
;6, NO + OClO = NO2 + ClO, 2.8E-13
7, Cl + O3 = ClO + O2, 1.1E-11
;8, Cl + NO3 = ClO + NO2, 2.4E-11 ; assumed to be negligible in the morning
;9, Cl + N2O = ClO + N2
;10, Cl + C2H5O2 = ClO + C2H5O
;11, Cl + OClO = ClO + ClO, 6.1E-11
;12, Cl + ClOO = ClO + ClO, 1.2E-11
;13, Cl + Cl2O = Cl2 + ClO, 1.0E-10
;14, Br + OClO = BrO + ClO, 2.2E-13
;15, Br + Cl2O = BrCl + ClO, 3.8E-12
;16, SO + OClO = SO2 + ClO

;All ClO Loss Reactions
17, O + ClO = Cl + O2, 3.8E-11
18, OH + ClO = Cl + HO2, 2.0E-11
19, OH + ClO = HCl + O2, 1.4E-12
20, HO2 + ClO = HOCl + O2, 6.0E-12
;21, ClO + O3 = ClOO + O2
;22, ClO + O3 = OClO + O2
;23, ClO + H2 = products
24, ClO + NO = NO2 + Cl, 1.9E-11
25, ClO + NO2 = ClONO2, 3.2E-12
;26, ClO + NO3 = ClOO + NO2, 4.7E-13 ; assumed to be negligible in the morning
;27, ClO + N2O = products
;28, ClO + CO = products
;29, ClO + CH4 = products
;30, ClO + H2CO = products
;31, ClO + CH3O2 = products, 2.2E-12
32, ClO + ClO = Cl2 + O2, 3.0E-15
;33, ClO + ClO = ClOO + Cl, 3.8E-15
;34, ClO + ClO = OClO + Cl, 2.3E-15
;35, ClO + ClO = ClOOCl, 3.6E-13
```

;36, ClO + OClO = Cl2O3, 1.8E-12
;37, Br + ClO = Br + OclO, 7.1E-12
;38, IO + ClO = products, 1.4E-11
;39, ClO + OCS = products
;40, ClO + CH3SCH3 = products, 7.3E-15
;41, ClO + CH3S(O)CH3 = products
;42, ClO + SO = Cl + SO2, 2.8E-11
;43, ClO + SO2 = Cl + SO3

;Photochemistry
44P, ClNO2 = Cl + NO2, 1.2E-4 ; main source of Cl in residual layer
;45P, ClOOCl = Cl + ClOO, 4.3E-4 ; photolysis path leading to ClO + ClO is not observed / low yield (& not in TUV)
46P, Cl2 = Cl + Cl, 6.1E-4 ; source of Cl
;47P, OClO = O + ClO, 2.3E-2
48P, ClONO2 = ClO + NO2, 1.4E-6
49P, ClO = Cl + O, 3.4E-6

;Major Cl Production Reactions (excluding repeats)
50, O + HCl = OH + Cl, 5.6E-17
51, OH + Cl2 = HOCl + Cl, 5.2E-14
52, OH + HCl = H2O + Cl, 7.2E-13
;53, NO3 + HCl = HNO3 + Cl ; assumed to be negligible in the morning

;Major Cl Loss Reactions (excluding repeats)
54, HO2 + Cl = HCl + O2, 3.4E-11
;55, Cl + O2 = ClOO, 7.6E-14
56, Cl + H2 = HCl + H, 7.5E-15
57, Cl + H2O2 = HCl + HO2, 3.0E-13
;58, Cl + NO = NOCl, 2.4E-12
59, Cl + NO2 = ClNO2, 2.0E-11
;60, Cl + HNO3 = products
;61, Cl + CO = ClCO, 5.0E-14
62, Cl + CH4 = HCl + CH3, 6.7E-14 ; Cl loss to methane
;63, Cl + C2H6 = HCl + C2H5, 5.6E-11; Cl loss to ethane
;64, Cl + C3H6O = C3H5O + HCl, 2.0E-12 ; Cl loss to acetone
65, Cl + HC = HCl + R, 5.6E-11; Cl loss to general hydrocarbon (using ethane rate constant)
;66, Cl + ClOO = Cl2 + O2, 2.3E-10
;67, Cl + ClO2 = products
;68, Cl + HOCl = products, 1.6E-12
;69, Cl + ClONO2 = products, 1.0E-11

;Tropospheric Chemistry
70P, O3 = O(1D) + O2, 2.1E-6
71, O(1D) + N2 = O + N2, 3.2E-11
72, O(1D) + O2 = O + O2, 4.0E-11
73, O + O2 = O3, 1.5E-14
74, O(1D) + H2O = OH + OH, 2.0E-10

```
75, OH + CO = H + CO2, 1.3E-13
76, H + O2 = HO2, 1.1E-12
77, HO2 + HO2 = H2O2 + O2, 1.7E-12
78P, H2O2 = OH + OH, 0.0E0
79, OH + O3 = HO2 + O2, 5.4E-14
80, HO2 + O3 = OH + 2O2, 1.7E-15
80b, 2O2 = O2 + O2, 1.E16
81, O3 + NO = NO2 + O2, 1.2E-14
82, HO2 + NO = NO2 + OH, 8.7E-12
83P, NO2 = O + NO, 3.0E-3 ; only significant source of O in troposphere
84, OH + CH4 = H2O + CH3, 3.7E-15 ; first step in methane oxidation
85, OH + HC = H2O + R, 1.7E-13 ; first step in VOC oxidation
;86, = HC, 5.0E5
87, O3 = , 1.0E-6 ; removal of O3 from the boundary layer

;Other Reactions (excluding repeats) to model Cl2, ClNO2, HCl, HOCl, ClONO2
88, OH + ClNO2 = HOCl + NO2, 2.5E-14 ; to model ClNO2
;89, O(1D) + Cl2 = products, 2.7E-10 ; to model Cl2
;90, Cl + ClNO = NO + Cl2, 8.4E-11 ; to model Cl2
;91, O(1D) + HCl = products, 1.5E-10 ; to model HCl
92P, HCl = H + Cl, 0.0E0 ; HCl photochemistry
;93, OH + OClO = HOCl + O2, 8.4E-12 ; to model HOCl
94P, HOCl = OH + Cl, 0.0E0 ; HOCl photochemistry
;95, O + ClONO2 = products, 1.5E-13 ; to model ClONO2
;96, OH + ClONO2 = products 3.6E-13 ; to model ClONO2
;97P, ClONO2 = Cl + NO3, 0.0E0 ; ClONO2 photochemistry

;98, = Cl, 5.E2

END
N2, 2.1E19 ; 78 % of [M]
O2, 5.6E18 ; 21 % of [M]
H2O, 8.1E16 ; 50 % relative humidity
CH4, 5.4E13 ; 2 ppm
H2, 1.3E13 ; 0.5 ppm
CO, 2.2E12 ; 80 ppb
O3, 8.1E11 ; 30 ppb
NO2, 2.7E10 ; assumed to be 1 ppb
HC, 2.7E11 ; assumed to be 10 ppb
ClNO2, 2.7E10 ; assumed to be 1 ppb
Cl2, 8.1E9 ; assumed to be 30% of ClNO2
END
0.001
0.0,
21600 ; 6 hours
```

A2: AtChem + MCM Model Input

```
************************************************************************ ;
* A citation to the MCM website and the relevant mechanism         * ;
* construction protocols should be given in any publication using   * ;
* information obtained from this source, using the following or     * ;
* comparable wording:                                              * ;
* The chemical mechanistic information was taken from the Master    * ;
* Chemical Mechanism, MCM v3.3.1 (ref), via website:               * ;
* http://mcm.leeds.ac.uk/MCM.                                      * ;
* The reference should be: (Jenkin et al., Atmos. Environ., 31, 81, * ;
* 1997; Saunders et al., Atmos. Chem. Phys., 3, 161, 2003), for     * ;
* non aromatic schemes; (Jenkin et al., Atmos. Chem. Phys., 3,  * ;
* 181, 2003; Bloss et al., Atmos. Chem. Phys., 5, 641, 2005), for   * ;
* aromatic schemes; (Jenkin et al., Atmos. Chem. Phys.,  12, * ;
* 5275, 2012), for the beta-caryophyllene scheme and (Jenkin et al., ;
* Atmos. Chem. Phys., 15, 11433, 2015), for the isoprene scheme.  * ;
************************************************************************ ;
* MCMv3.3.1 Subset generated for the following species:   ;
* CH4 ;
*;
* Variable definitions.  All species are listed here.;
*;
VARIABLE
 HCHO CH3NO3 CH3OH O1D O3 HO2NO2 NO3 N2O5 H2O2 NO NA HO2 NO2 CH4
HSO3 CO CL O HNO3 SO3 SO2 CH3O OH H2 HONO CH3O2NO2 CH3OOH SA CH3O2 CLNO2 CL2 CLO HCL
HOCL CLONO2;
************************************************** ;
*;
* Generic Rate Coefficients ;
*;
KRO2NO = 2.7D-12*EXP(360/TEMP) ;
KRO2HO2 = 2.91D-13*EXP(1300/TEMP) ;
KAPHO2 = 5.2D-13*EXP(980/TEMP) ;
KAPNO = 7.5D-12*EXP(290/TEMP) ;
KRO2NO3 = 2.3D-12 ;
KNO3AL = 1.4D-12*EXP(-1860/TEMP) ;
KDEC = 1.00D+06 ;
KROPRIM = 2.50D-14*EXP(-300/TEMP) ;
KROSEC = 2.50D-14*EXP(-300/TEMP) ;
KCH3O2 = 1.03D-13*EXP(365/TEMP) ;
K298CH3O2 = 3.5D-13 ;
K14ISOM1 = 3.00D7*EXP(-5300/TEMP) ;
*;
* Complex reactions ;
*;
KD0 = 1.10D-05*M*EXP(-10100/TEMP) ;
```

```
KDI = 1.90D17*EXP(-14100/TEMP) ;
KRD = KD0/KDI ;
FCD = 0.30 ;
NCD = 0.75-1.27*(LOG10(FCD)) ;
FD = 10@(LOG10(FCD)/(1+(LOG10(KRD)/NCD)**2)) ;
KBPAN = (KD0*KDI)*FD/(KD0+KDI) ;
KC0 = 3.28D-28*M*(TEMP/300)@-6.87 ;
KCI = 1.125D-11*(TEMP/300)@-1.105 ;
KRC = KC0/KCI ;
FCC = 0.30 ;
NC = 0.75-1.27*(LOG10(FCC)) ;
FC = 10@(LOG10(FCC)/(1+(LOG10(KRC)/NC)**2)) ;
KFPAN = (KC0*KCI)*FC/(KC0+KCI) ;
K10 = 1.0D-31*M*(TEMP/300)@-1.6 ;
K1I = 5.0D-11*(TEMP/300)@-0.3 ;
KR1 = K10/K1I ;
FC1 = 0.85 ;
NC1 = 0.75-1.27*(LOG10(FC1)) ;
F1 = 10@(LOG10(FC1)/(1+(LOG10(KR1)/NC1)**2)) ;
KMT01 = (K10*K1I)*F1/(K10+K1I) ;
K20 = 1.3D-31*M*(TEMP/300)@-1.5 ;
K2I = 2.3D-11*(TEMP/300)@0.24 ;
KR2 = K20/K2I ;
FC2 = 0.6 ;
NC2 = 0.75-1.27*(LOG10(FC2)) ;
F2 = 10@(LOG10(FC2)/(1+(LOG10(KR2)/NC2)**2)) ;
KMT02 = (K20*K2I)*F2/(K20+K2I) ;
K30 = 3.6D-30*M*(TEMP/300)@-4.1 ;
K3I = 1.9D-12*(TEMP/300)@0.2 ;
KR3 = K30/K3I ;
FC3 = 0.35 ;
NC3 = 0.75-1.27*(LOG10(FC3)) ;
F3 = 10@(LOG10(FC3)/(1+(LOG10(KR3)/NC3)**2)) ;
KMT03 = (K30*K3I)*F3/(K30+K3I) ;
K40 = 1.3D-3*M*(TEMP/300)@-3.5*EXP(-11000/TEMP) ;
K4I = 9.7D+14*(TEMP/300)@0.1*EXP(-11080/TEMP) ;
KR4 = K40/K4I ;
FC4 = 0.35 ;
NC4 = 0.75-1.27*(LOG10(FC4)) ;
F4 = 10@(LOG10(FC4)/(1+(LOG10(KR4)/NC4)**2)) ;
KMT04 = (K40*K4I)*F4/(K40+K4I) ;
KMT05 = 1.44D-13*(1+(M/4.2D+19)) ;
KMT06 = 1 + (1.40D-21*EXP(2200/TEMP)*H2O) ;
K70 = 7.4D-31*M*(TEMP/300)@-2.4 ;
K7I = 3.3D-11*(TEMP/300)@-0.3 ;
KR7 = K70/K7I ;
FC7 = 0.81 ;
NC7 = 0.75-1.27*(LOG10(FC7)) ;
```

```
F7 = 10@(LOG10(FC7)/(1+(LOG10(KR7)/NC7)**2)) ;
KMT07 = (K70*K7I)*F7/(K70+K7I) ;
K80 = 3.2D-30*M*(TEMP/300)@-4.5 ;
K8I = 3.0D-11 ;
KR8 = K80/K8I ;
FC8 = 0.41 ;
NC8 = 0.75-1.27*(LOG10(FC8)) ;
F8 = 10@(LOG10(FC8)/(1+(LOG10(KR8)/NC8)**2)) ;
KMT08 = (K80*K8I)*F8/(K80+K8I) ;
K90 = 1.4D-31*M*(TEMP/300)@-3.1 ;
K9I = 4.0D-12 ;
KR9 = K90/K9I ;
FC9 = 0.4 ;
NC9 = 0.75-1.27*(LOG10(FC9)) ;
F9 = 10@(LOG10(FC9)/(1+(LOG10(KR9)/NC9)**2)) ;
KMT09 = (K90*K9I)*F9/(K90+K9I) ;
K100 = 4.10D-05*M*EXP(-10650/TEMP) ;
K10I = 6.0D+15*EXP(-11170/TEMP) ;
KR10 = K100/K10I ;
FC10 = 0.4 ;
NC10 = 0.75-1.27*(LOG10(FC10)) ;
F10 = 10@(LOG10(FC10)/(1+(LOG10(KR10)/NC10)**2)) ;
KMT10 = (K100*K10I)*F10/(K100+K10I) ;
K1 = 2.40D-14*EXP(460/TEMP) ;
K3 = 6.50D-34*EXP(1335/TEMP) ;
K4 = 2.70D-17*EXP(2199/TEMP) ;
K2 = (K3*M)/(1+(K3*M/K4)) ;
KMT11 = K1 + K2 ;
K120 = 2.5D-31*M*(TEMP/300)@-2.6 ;
K12I = 2.0D-12 ;
KR12 = K120/K12I ;
FC12 = 0.53 ;
NC12 = 0.75-1.27*(LOG10(FC12)) ;
F12 = 10@(LOG10(FC12)/(1.0+(LOG10(KR12)/NC12)**2)) ;
KMT12 = (K120*K12I*F12)/(K120+K12I) ;
K130 = 2.5D-30*M*(TEMP/300)@-5.5 ;
K13I = 1.8D-11 ;
KR13 = K130/K13I ;
FC13 = 0.36 ;
NC13 = 0.75-1.27*(LOG10(FC13)) ;
F13 = 10@(LOG10(FC13)/(1+(LOG10(KR13)/NC13)**2)) ;
KMT13 = (K130*K13I)*F13/(K130+K13I) ;
K140 = 9.0D-5*EXP(-9690/TEMP)*M ;
K14I = 1.1D+16*EXP(-10560/TEMP) ;
KR14 = K140/K14I ;
FC14 = 0.36 ;
NC14 = 0.75-1.27*(LOG10(FC14)) ;
F14 = 10@(LOG10(FC14)/(1+(LOG10(KR14)/NC14)**2)) ;
```

```
KMT14 = (K140*K14I)*F14/(K140+K14I) ;
K150 = 8.6D-29*M*(TEMP/300)@-3.1 ;
K15I = 9.0D-12*(TEMP/300)@-0.85 ;
KR15 = K150/K15I ;
FC15 = 0.48 ;
NC15 = 0.75-1.27*(LOG10(FC15)) ;
F15 = 10@(LOG10(FC15)/(1+(LOG10(KR15)/NC15)**2)) ;
KMT15 = (K150*K15I)*F15/(K150+K15I) ;
K160 = 8D-27*M*(TEMP/300)@-3.5 ;
K16I = 3.0D-11*(TEMP/300)@-1 ;
KR16 = K160/K16I ;
FC16 = 0.5 ;
NC16 = 0.75-1.27*(LOG10(FC16)) ;
F16 = 10@(LOG10(FC16)/(1+(LOG10(KR16)/NC16)**2)) ;
KMT16 = (K160*K16I)*F16/(K160+K16I) ;
K170 = 5.0D-30*M*(TEMP/300)@-1.5 ;
K17I = 1.0D-12 ;
KR17 = K170/K17I ;
FC17 = 0.17*EXP(-51/TEMP)+EXP(-TEMP/204) ;
NC17 = 0.75-1.27*(LOG10(FC17)) ;
F17 = 10@(LOG10(FC17)/(1.0+(LOG10(KR17)/NC17)**2)) ;
KMT17 = (K170*K17I*F17)/(K170+K17I) ;
KMT18 = 9.5D-39*O2*EXP(5270/TEMP)/(1+7.5D-29*O2*EXP(5610/TEMP)) ;
KPPN0 = 1.7D-03*EXP(-11280/TEMP)*M ;
KPPNI = 8.3D+16*EXP(-13940/TEMP) ;
KRPPN = KPPN0/KPPNI ;
FCPPN = 0.36 ;
NCPPN = 0.75-1.27*(LOG10(FCPPN)) ;
FPPN = 10@(LOG10(FCPPN)/(1+(LOG10(KRPPN)/NCPPN)**2)) ;
KBPPN = (KPPN0*KPPNI)*FCPPN/(KPPN0+KPPNI) ;
************************************************** ;
*;
* Peroxy radicals. ;
*;
* WARNING: The following species do not have SMILES strings in the database. ;
*        If any of these are peroxy radicals the RO2 sum will be wrong!!! ;
************************************************** ;
*  ;
RO2 = CH3O2 ;
*;
* Reaction definitions. ;
*;
% 5.6D-34*N2*(TEMP/300)@-2.6*O2 : O = O3 ;
% 6.0D-34*O2*(TEMP/300)@-2.6*O2 : O = O3 ;
% 8.0D-12*EXP(-2060/TEMP) : O + O3 = ;
% KMT01 : O + NO = NO2 ;
% 5.5D-12*EXP(188/TEMP) : O + NO2 = NO ;
% KMT02 : O + NO2 = NO3 ;
```

```
% 3.2D-11*EXP(67/TEMP)*O2 : O1D = O ;
% 2.0D-11*EXP(130/TEMP)*N2 : O1D = O ;
% 1.4D-12*EXP(-1310/TEMP) : NO + O3 = NO2 ;
% 1.4D-13*EXP(-2470/TEMP) : NO2 + O3 = NO3 ;
% 3.3D-39*EXP(530/TEMP)*O2 : NO + NO = NO2 + NO2 ;
% 1.8D-11*EXP(110/TEMP) : NO + NO3 = NO2 + NO2 ;
% 4.50D-14*EXP(-1260/TEMP) : NO2 + NO3 = NO + NO2 ;
% KMT03 : NO2 + NO3 = N2O5 ;
% 2.14D-10*H2O : O1D = OH + OH ;
% 1.70D-12*EXP(-940/TEMP) : OH + O3 = HO2 ;
% 7.7D-12*EXP(-2100/TEMP) : OH + H2 = HO2 ;
% KMT05 : OH + CO = HO2 ;
% 2.9D-12*EXP(-160/TEMP) : OH + H2O2 = HO2 ;
% 2.03D-16*(TEMP/300)@4.57*EXP(693/TEMP) : HO2 + O3 = OH ;
% 4.8D-11*EXP(250/TEMP) : OH + HO2 = ;
% 2.20D-13*KMT06*EXP(600/TEMP) : HO2 + HO2 = H2O2 ;
% 1.90D-33*M*KMT06*EXP(980/TEMP) : HO2 + HO2 = H2O2 ;
% KMT07 : OH + NO = HONO ;
% KMT08 : OH + NO2 = HNO3 ;
% 2.0D-11 : OH + NO3 = HO2 + NO2 ;
% 3.45D-12*EXP(270/TEMP) : HO2 + NO = OH + NO2 ;
% KMT09 : HO2 + NO2 = HO2NO2 ;
% 3.2D-13*EXP(690/TEMP)*1.0 : OH + HO2NO2 = NO2 ;
% 4.0D-12 : HO2 + NO3 = OH + NO2 ;
% 2.5D-12*EXP(260/TEMP) : OH + HONO = NO2 ;
% KMT11 : OH + HNO3 = NO3 ;
% 4.0D-32*EXP(-1000/TEMP)*M : O + SO2 = SO3 ;
% KMT12 : OH + SO2 = HSO3 ;
% 1.3D-12*EXP(-330/TEMP)*O2 : HSO3 = HO2 + SO3 ;
% 6.00D-06 : HNO3 = NA ;
% 4.00D-04 : N2O5 = NA + NA ;
% 1.20D-15*H2O : SO3 = SA ;
% J<1> : O3 = O1D ;
% J<2> : O3 = O ;
% J<3> : H2O2 = OH + OH ;
% J<4> : NO2 = NO + O ;
% J<5> : NO3 = NO ;
% J<6> : NO3 = NO2 + O ;
% J<7> : HONO = OH + NO ;
% J<8> : HNO3 = OH + NO2 ;
% KMT04 : N2O5 = NO2 + NO3 ;
% KMT10 : HO2NO2 = HO2 + NO2 ;
% 6.6D-12*EXP(-1240/TEMP) : CL + CH4 = CH3O2 ;
% 1.85D-12*EXP(-1690/TEMP) : OH + CH4 = CH3O2 ;
% 3.8D-13*EXP(780/TEMP)*(1-1/(1+498*EXP(-1160/TEMP))) : CH3O2 + HO2 =
CH3OOH ;
% 3.8D-13*EXP(780/TEMP)*(1/(1+498*EXP(-1160/TEMP))) : CH3O2 + HO2 =
```

HCHO ;
% 2.3D-12*EXP(360/TEMP)*0.001 : CH3O2 + NO = CH3NO3 ;
% 2.3D-12*EXP(360/TEMP)*0.999 : CH3O2 + NO = CH3O + NO2 ;
% KMT13 : CH3O2 + NO2 = CH3O2NO2 ;
% 1.2D-12 : CH3O2 + NO3 = CH3O + NO2 ;
% 2*KCH3O2*RO2*7.18*EXP(-885/TEMP) : CH3O2 = CH3O ;
% 2*KCH3O2*RO2*0.5*(1-7.18*EXP(-885/TEMP)) : CH3O2 = CH3OH ;
% 2*KCH3O2*RO2*0.5*(1-7.18*EXP(-885/TEMP)) : CH3O2 = HCHO ;
% J<41> : CH3OOH = CH3O + OH ;
% 5.3D-12*EXP(190/TEMP)*0.6 : OH + CH3OOH = CH3O2 ;
% 5.3D-12*EXP(190/TEMP)*0.4 : OH + CH3OOH = HCHO + OH ;
% J<11> : HCHO = CO + HO2 + HO2 ;
% J<12> : HCHO = H2 + CO ;
% 5.5D-16 : NO3 + HCHO = HNO3 + CO + HO2 ;
% 5.4D-12*EXP(135/TEMP) : OH + HCHO = HO2 + CO ;
% J<51> : CH3NO3 = CH3O + NO2 ;
% 4.0D-13*EXP(-845/TEMP) : OH + CH3NO3 = HCHO + NO2 ;
% 7.2D-14*EXP(-1080/TEMP)*O2 : CH3O = HCHO + HO2 ;
% KMT14 : CH3O2NO2 = CH3O2 + NO2 ;
% 2.85D-12*EXP(-345/TEMP) : CH3OH + OH = HO2 + HCHO ;
% J<4>/30 : CLNO2 = CL + NO2 ;
% 2.6D-12*EXP(-350/TEMP) : HCL + OH = CL + H2O ;
% 2.8D-11*EXP(-250/TEMP) : CL + O3 = CLO + O2 ;
% 6.2D-12*EXP(295/TEMP) : CLO + NO = CL + NO2 ;
% 2.2D-12*EXP(340/TEMP) : CLO + HO2 = HOCL + O2 ;
% 2.3399D-12 : CLO + NO2 = CLONO2 ;
% J<3>*5.4 : CLONO2 = CL + NO3 ;
% J<3>*1.1 : CLONO2 = CLO + NO2 ;
% J<3>*37 : HOCL = CL + OH ;
% J<11>*75 : CL2 = CL + CL ;
*;
* End of Subset. No. of Species = 36, No. of Reactions = 81 ;